TÜRKİYE CUMHURİYETİ
ADANA ALPARSLAN TÜRKEŞ SCIENCE AND TECHNOLOGY UNIVERSITY

GRADUATE SCHOOL
MATERIALS ENGINEERING DEPARTMENT

SYNTHESIS AND CHARACTERIZATION OF SOME PHYSICAL PROPERTIES OF Fe_3O_4 DOPED MoS_2/PANI HYBRID COMPOSITES

CEMAL AKA

M.Sc.

ADANA 2024

TÜRKİYE CUMHURİYETİ
ADANA ALPARSLAN TÜRKEŞ SCIENCE AND TECHNOLOGY UNIVERSITY

GRADUATE SCHOOL
MATERIALS ENGINEERING DEPARTMENT

SYNTHESIS AND CHARACTERIZATION OF SOME PHYSICAL PROPERTIES OF Fe_3O_4 DOPED MoS_2/PANI HYBRID COMPOSITE

CEMAL AKA

M.Sc.

THESIS ADVISOR
ASSOC. PROF. DR. MUSTAFA AKYOL

ADANA, 2024

DECLARATION OF CONFORMITY

In this thesis study, which was prepared following the thesis writing rules of Adana Alparslan Türkeş Science and Technology University Institute of Graduate School, I declare that I provide all the information, documents, evaluations and results in accordance with scientific ethics and moral codes without resorting to any means or assistance that would be contrary to scientific ethics and traditions. I also declare that I refer to all of the articles I used in this study with appropriate references and accept all moral and legal consequences if a situation is found contrary to my statement regarding my work.

15/02/2024

Cemal AKA

ÖZET

Fe_3O_4 KATKILI MoS_2/PANI HİBRİT KOMPOZİTLERİN BAZI FİZİKSEL ÖZELLİKLERİNİN SENTEZİ VE KARAKTERİZASYONU

Cemal AKA
Yüksek Lisans, Malzeme Mühendisliği Anabilim Dalı
Danışman: Doç. Dr. Mustafa AKYOL
Şubat 2024, 80 sayfa

Malzemelerde elektromanyetik dalgaları absorbe eden sistemler, gizli uygulamalar ve hassas elektronik ekipmanlar için gereklidir. Bununla birlikte, EMW'yi geniş bir bant genişliği boyunca absorbe etme yeteneği, malzeme sistemleri ve mühendisliğindeki bazı sınırlamalarla hala sınırlıdır. Bant genişliğinin artırılması ve malzeme sistemi yansımalarının azaltılması, gelecekteki gizli teknolojilerin geliştirilmesi için çok önemli ilerlemelerdir. Bu çalışmada, yarı iletken MoS_2 nano tabakaları, Fe_3O_4 manyetik nanopartiküller ve iletken polianilin kullanılarak hibrit yapılar geliştirilmiştir. Bu hibrit yapıların yapısal, manyetik, morfolojik, termal, elektronik ve elektromanyetik özelliklerini incelemek için sistematik bir yaklaşım kullanılmıştır. Analiz sonucunda, elektromanyetik dalgaları etkili bir şekilde absorbe edebilen Fe_3O_4:MoS_2 ve PANI@Fe_3O_4:MoS_2 hibrit yapılarının üstün EMW absorpsiyon özelliklerine sahip olduğu görülmüştür. Özellikle, $F_{10}M_{90}$ numunesi 3 mm kalınlıkta ve 7,86 GHz frekansta -54,97 dB'lik minimum yansıma kaybına ulaşmış ve 4,0 GHz'lik etkili bir soğurma aralığına sahip olmuştur. $P_{50}F_{2.5}M_{47.5}$ numunesi 2 mm kalınlıkta ve 13,18 GHz frekansta -27,58 dB'lik minimum yansıma kaybına ulaşmış ve 8,03 GHz'lik etkili bir soğurma bant genişliğine sahip olmuştur. Deneysel bulgulara dayanarak, hafif yapıları ve yüksek sıcaklık kararlılıkları ile karakterize edilen PANI@Fe_3O_4:MoS_2 gibi hibrit nanokompozitlerin geniş bant aralığında EMW'nin neredeyse %99'unu etkili bir şekilde absorbe edebildiği sonucuna varılmıştır.

Anahtar Kelimeler: Polyaniline, MoS_2, hibrit yapı, electromanyetik dalga soğurma, Fe_3O_4 nanoparçacıkları

ABSTRACT

SYNTHESIS AND CHARACTERIZATION OF SOME PHYSICAL PROPERTIES OF Fe_3O_4 DOPED MoS_2/PANI HYBRID COMPOSITES

Cemal AKA

M.Sc., Department of Materials Engineering

Supervisor: Assoc. Prof. Dr. Mustafa AKYOL

February 2024, 80 pages

Systems for absorbing electromagnetic waves in materials are essential for stealth applications and vulnerable electronic equipment. However, the ability to absorb EMW over a large bandwidth is still limited by certain limitations in material systems and engineering. Increasing the bandwidth and reducing material system reflections are crucial advancements for the development of future stealth technologies. In this study, hybrid structures were developed using semiconducting MoS_2 nanosheets, Fe_3O_4 magnetic nanoparticles and conductive polyaniline. A systematic approach was employed to examine the structural, magnetic, morphological, thermal, electronic, and electromagnetic properties of these hybrid structures. As a result of the analysis, Fe_3O_4:MoS_2 and PANI@Fe_3O_4:MoS_2 hybrid sturucture, which can effectively absorb electromagnetic waves, were found to have superior EMW absorption properties. In particular, The $F_{10}M_{90}$ sample achieved a minimum reflection loss of -54.97 dB at a thickness of 3 mm and a frequency of 7.86 GHz, with an effective absorption range of 4.0 GHz. The $P_{50}F_{2.5}M_{47.5}$ sample achieved a minimum reflection loss of -27.58 dB at a thickness of 2 mm and a frequency of 13.18 GHz, with an effective absorption bandwidth of 8.03 GHz. Based on the experimental findings, it is concluded that hybrid nanocomposites such as PANI@Fe_3O_4:MoS_2, which are characterized by their lightweight structure and high temperature stability, can effectively absorb almost 99% of the EMW in the broadband range.

Keywords: Polyaniline, MoS_2, hybrid sturucture, electromagnetic wave absorbing, Fe_3O_4 nanoparticles

Dedication

Dedicate this thesis to my family and nation.

ACKNOWLEDGEMENTS

First of all, I would like to express my thanks and gratitude to everyone who supported me in my thesis studies throughout my graduate education and contributed to my scientific, social and life experience.

I would like to thank my esteemed advisor, Assoc. Prof. Dr. Mustafa AKYOL, whom I had the opportunity to get to know thanks to my master's degree education and who shed light on my path and motivated me with his vast knowledge and experience throughout my education.

I would like to thank Prof. Dr. Muharrem KARAASLAN, Assoc. Prof. Dr. Oğuzhan AKGÖL, Res. Assist. Fatih Özkan ALKURT, and the academicians of İskenderun Technical University who supported me with their laboratory facilities for the electromagnetic analyses of composite samples in my thesis.

I would like to thank my professors in the Department of Materials Science and Engineering who supported me with their knowledge and experience in my thesis studies.

I would like to thank Bekir ÇALIŞKAN, the secretary of the Faculty of Engineering, who helped me with all my needs at our university.

Finally, I would like to express my sincere love and gratitude to my beloved family, who has always been with me, supported me in every material and moral way, always stood by me and did everything for my happiness.

I would like to thank TÜBİTAK 2210-C Domestic Priority Areas Graduate Scholarship Program with project number 1649B022009657 for the scholarship during October 2022 - October 2023.

This work was supported by TÜBİTAK ARDEB-3501 program with project number 121F367. This thesis work was partially supported by ATU BAP Coordination Unit with project number of 22303006.

TABLE OF CONTENTS

LIST OF FIGURES

LIST OF TABLES

LIST OF ABBREVIATIONS

PPMS	: Physical Properties Measurement System
RAC	: Radar Absorbing Composites
RAM	: Radar Absorbing Materials
RCS	: Radar Cross Section
RL	: Reflection Loss
RF	: Radio Frequency
SEM	: Scanning Electron Microscopy
TB	: Blocking temperature
TC	: Curie temperature
TN	: Neel temperature
VSM	: Vibrating Sample Magnetometer
ZFC	: Zero Field Cooled
XRD	: X-Ray Diffraction
EDS	: Energy-Dispersive X-Ray Spectroscopy
FOPEN	: Foliage Penetration
AEW	: Airborne Early Warning
UAV	: Unmanned Air Vehicle
EMW	: Electromagnetic Wave
APS	: Ammonium Persulfate
PANI	: Polyaniline
DI	: Deionized

TG	: Thermogravimetric
TGA	: Thermogravimetric Analysis
VNA	: Vector Network Analyzer

LIST OF SYMBOLS

Å	: Angstrom
$\vec{a}$	: Acceleration
$\vec{B}$	: Magnetic field
C	: Curie constant
°C	: Celsius degree
D	: Crystallite size
$\vec{E}$	: Electric field
e-	: Electron charge
eV	: Electron Volts
FC	: Field Cooled
GHz	: Gigahertz
g	: Gram
hkl	: Miller indices
$\vec{H}$	: External magnetic field
Hc	: Coercive field
I	: Current
J	: Current density
$\vec{j}$	: Total angular momentum
j	: Total angular momentum quantum number
K	: Kelvin
kB	: Boltzmann Constant

$\vec{L}$: Orbital angular momentum

l : Orbital angular momentum quantum number

MHz : Megahertz

m : Mass

$\vec{M}$: Magnetization vector

Ms : Saturation Magnetization

Mr : Remanence Magnetization

Oe : Oersted

Q : Temperature constant

τ : Relaxation time

V : Speed

χ : Magnetic susceptibility

λ : Wavelength

θ : Bragg angle

μ : Magnetic moment

μB : Bohr magnetron

μ_0 : Free space magnetic permeability

γ : Gyromagnetic ratio

π : Pi number

$\vec{S}$: Spin angular momentum quantum number

α : Attenuation constant

C_0 : Eddy current loss

ε'	: The real side of the dielectric constant
ε''	: The imaginary side of the dielectric constant
ε_r	: Complex dielectric constant
μ_r	: The complex magnetic permeability
μ'	: The real side of the magnetic permeability
μ''	: The imaginary side of the magnetic permeability
$\tan\delta$	: Loss tangent
$\tan\delta_\varepsilon$	: Dielectric loss
$\tan\delta_\mu$	: Magnetic loss
r	: Reflection coefficient
η	: Admittance of the radiating medium
Z_M	: Impedance of the material
Z_0	: Impedance of the free space
μ_0	: Magnetic constant
ε_0	: Electric constant
c	: Speed of electromagnetic wave in the space
f	: Frequency
d	: Thickness
ε_s	: Static frequency dielectric constant
ε_∞	: Infinite frequency dielectric constant
$\vec{A}$	: Normal area vector
eV	: Electronvolt

H_c : Coercive field

HCl : Hydrochloric acid

φ_{in} : Inner diameter

φ_{out} : Out diameter

Z_{in} : Input impedance of the absorbent material

1. INTRODUCTION

Electromagnetic waves have started to be used in electronic devices, trade, and communication and defence industry etc. as a result of the development of technology. In particular, electromagnetic waves used in the defence industry to detect the position and speed of military vehicles constitute the basis of radar technology. As a result of the development of radar technology, it has become easier to detect the vehicles of enemy forces by integrating radar systems into land, sea and air vehicles used in the defence industry.

Radar is a technological system utilizing electromagnetic waves for the detection of the size, speed, range, and position of stationary or mobile objects. Operating within the frequency range of 300 MHz to 300 GHz, radar systems function across wavelengths spanning from 1 mm to 1 m.

The working principle of radars is very simple. The electromagnetic wave sent from the radar source captures the object and reflects the electromagnetic wave back. The receiver collects the reflected electromagnetic wave so that the radar can observe the object. As depicted in Figure 1.1, certain radio waves, whether pulsed or continuous, emitted by the transmitter are reflected off the object and subsequently received by the receiver. This process furnishes details regarding the object's position and speed. This information is provided using the energy of the reflected wave [1].

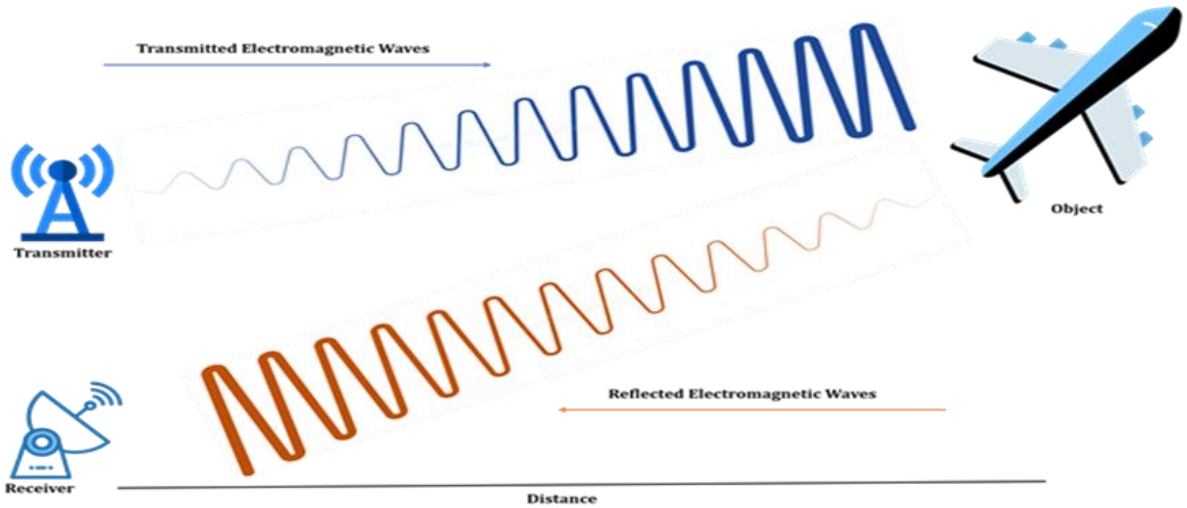

Figure 1.1. Working principle of radar system.

The amount of the electromagnetic wave sent to the object, which is reflected back and absorbed after contact with the object, varies depending on the surface and material properties. If the material has a smooth surface, the incident electromagnetic wave will be reflected back in one direction. Thus, the radar system can easily determine the speed and position of the object. However, if the material has a porous surface with sharp transitions, the incident electromagnetic wave will be reflected in different directions. As a result, the radar system will have difficulty in detecting the speed and position of the object.

As a consequence of the development of radar technology, weapons used in land, sea and air forces are now designed to be invisible to radar. Thus, a new field of study, stealth technology, has emerged. Stealth technology can be defined as low observability [2]. The main purpose of stealth technology is to make combat aircraft, helicopters, warships and other military vehicles less visible to detection methods such as radar, infrared and sonar. In other words, the aim is to reduce the radar cross section (RCS) of the target vehicle. The radar cross section is described as a measure of how detectable an object is to radar. Factors affecting radar detectability include the material from which the target is made, the size, shape and orientation of the target, the angle of incidence, the angle of reflection, the frequency and polarisation of the radar signal. Taking advantage of these factors, researchers in many countries have started to work on the design of radar absorbing materials to reduce the radar cross-sectional area.

Research on electromagnetic wave absorbers began in the 1930s, and the first patent was obtained in the Netherlands in 1936 [2, 3]. Since these years, interest in radar absorbing materials has increased and studies on this subject have increased day by day. The main objective was to achieve high reflection loss over a wide effective absorption range [4]. For this reason, RAMs continue to be designed with different designs and contents in the literature.

1.1. Fundamental of electromagnetic wave and absorbing theory

Electromagnetic waves are produced by accelerating electrons and photons. Electromagnetic waves are a type of radiation that can reach everywhere in the universe. Electromagnetic waves are generated by both electric and magnetic fields. Figure 1.2a shows the formation of electromagnetic waves. In this context, electromagnetic waves are characterized by

perpendicular electric and magnetic fields, with transverse waves propagating in a direction perpendicular to the plane formed by these fields. [5]. Electromagnetic waves are classified according to their frequencies and wavelengths and the electromagnetic wave spectrum is given in Figure 1.2b. Electromagnetic waves are listed as radio waves, microwaves, visible region, ultraviolet, X-ray and Gamma Rays according to energy increase and wavelength decrease.

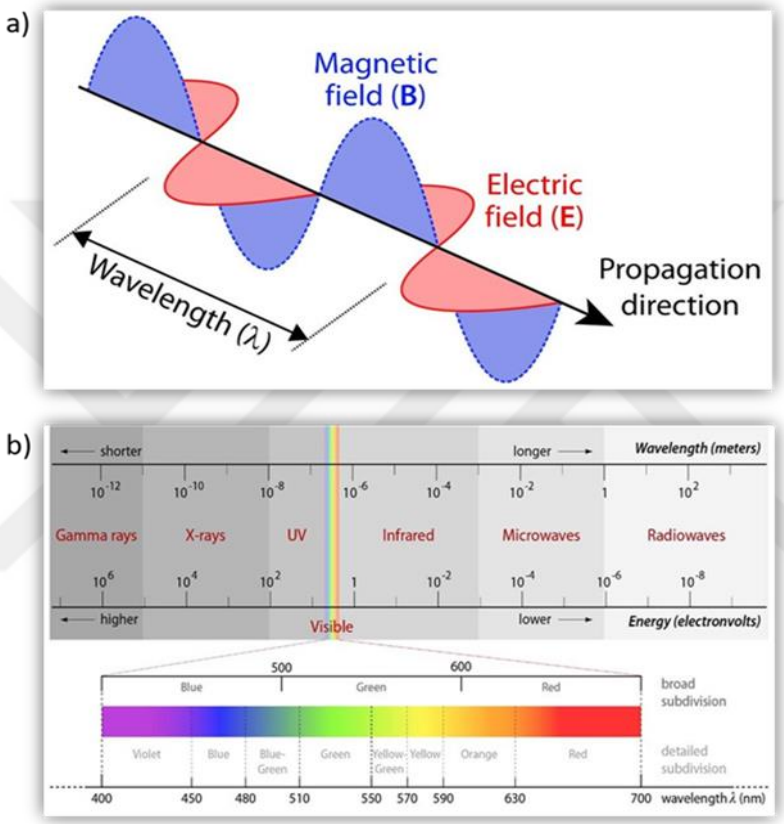

Figure 1.2. a) Generation of electromagnetic wave b) electromagnetic spectrum [6].

Microwave radiations encompass electromagnetic waves with frequencies falling within the range of 300 MHz to 300 GHz and wavelengths spanning from one millimeter to one meter. Many sources define microwaves in different frequency ranges; our definition includes the UHF, SHF and EHF bands. In radio frequency engineering, the commonly accepted definition narrows ranging from 1 to 100 GHz (0.3 mm to 3 mm) for microwave frequencies. Microwaves are in any case known to include the entire SHF band (3 to 30 GHz). Microwave frequency ranges are often referred to by IEE radar band names. The band names are S, C, X, Ku, K or Ka respectively.

Thanks to electromagnetic methods, the location, position and velocity of objects from nano to macro size can be determined. Therefore, to understand the function of electromagnetic waves in the detection of objects, it is necessary to understand their interaction with the object. The interactions depend on the shape, content, structure and properties of the material of the item, as well as the electromagnetic wave frequency and angle of arrival. Table 1.1 shows the frequency ranges and application areas of radar systems. The propagation of electromagnetic waves is mainly described by magnetic permeability and dielectric permeability [7]. In other words, the electromagnetic properties of a material depend on its dielectric and magnetic properties.

Table 1.1. Frequency ranges and application areas of radar systems [8].

Band Code	Frequency Range	Application Areas
HF	3-30 MHz	Over-the-horizon surveillance typically involves limited range and resolution capabilities.
VHF	50-330 MHz	Low/medium resolution; long-range surveillance; foliage penetration (FOPEN); counter-stealth; and ground penetration.
UHF	300-1000 MHz	FOPEN long-range observation has inadequate to medium resolution.
L	1-2 GHz	Medium resolution, little air impact; long range air traffic management and surveillance.
S	2-4 GHz	Medium-range surveillance, terminal air traffic control, long-range air surveillance, airborne early warning (AEW).
C	4-8 GHz	Long-range tracking, weather observation, and weapon positioning are impacted more in light to medium rain.
X	8-12 GHz	Various purposes are served by short-range tracking, missile guidance, maritime radar mapping, airborne interception, battlefield surveillance, and weapon location.
Ku	12-18 GHz	Satellite altimetry, and unmanned aerial vehicle (UAV) radar serve distinct purposes.
K	18-27 GHz	Police radar is restricted in its application due to significant water vapor absorption.
Ka	27-40 GHz	Short-range, high-resolution mapping and airport surveillance are limited by the absorption of water vapor, which reduces their effective range.
V	40-75 GHz	In the scientific field, it is used for high water vapor absorption.
W	75-110 GHz	It is used for very high resolution imaging, automobile cruise control and missile detection.
Mm	110-300 GHz	Used in the experimental field. Short range due to high water vapor absorption.

1.1.1. Dielectric loss mechanism

It is described as the interaction between the material and the electric field, known as the dielectric constant. The real side of the dielectric constant (ε') indicates how much energy is stored in the material in the case of an externally applied electric field. The imaginary side of the dielectric constant (ε'') indicates the energy loss in the external electric field applied to the material. The real (ε') and imaginary (ε''') dielectric constants form the complex dielectric constant (ε_r). The complex permeability can be defined by the following equation;

$$\varepsilon = \varepsilon' - i\varepsilon'' \tag{1.1}$$

where ε' and ε'' real and imaginary permittivity, respectively.

1.1.2. Magnetic loss mechanism

The interaction of the material with the magnetic field is called magnetic permeability (μ). The complex magnetic permeability (μ_r) consists of two parts: real (μ') and imaginary (μ'') magnetic permeability [9]. These parts are defined as energy storage and loss, respectively. The equation of magnetic loss is as follows;

$$\mu = \mu' - i\mu'' \tag{1.2}$$

where ε' and ε'' real and imaginary permittivity, respectively.

1.1.3. Loss tangent

One of the values indicating the electromagnetic properties of the material is the loss tangent (tanδ). The loss tangent has two different values: dielectric ($\tan\delta_\varepsilon$) and magnetic ($\tan\delta_\mu$) loss factor [10, 11]. These values indicate whether the absorption ability of the material is due to dielectric loss or magnetic loss. Loss tangent equations are as follows;

$$tan\delta_\varepsilon = \frac{\varepsilon''}{\varepsilon'} \;\; and \;\; tan\delta_\mu = \frac{\mu''}{\mu'} \text{ so } \tan\delta = tan\delta_\varepsilon + tan\delta_\mu \tag{1.3}$$

1.1.4. Radar absorbing mechanism

Radar systems are a significant technological vehicle for determining the position and speed of a target. These systems are of great importance to the defence industry as they play a vital role in detecting enemy combat vehicles. The advancement of radar technology has necessitated the creation of radar-absorbing materials to counteract it. Radar-absorbing

materials absorb the electromagnetic wave from the radar system and prevent it from reaching the transmitter. Therefore, radar-absorbing materials are of great importance to the defence industry for electronic warfare. To understand the radar absorption mechanism and radar absorbing materials, we need to understand the relationship between the electromagnetic wave and the material. The main objective is to minimise the reflection coefficient, which is the ratio of reflected energy to incident energy. While aiming to minimise the reflection in the material, it is necessary to study the physical equations that describe the reflection process. There are 3 basic conditions to achieve minimum reflection [12]. The reflection coefficient with an interface is as follows;

$$r = \frac{\eta_M - \eta_0}{\eta_M + \eta_0} = \frac{Z_M - Z_0}{Z_M + Z_0} \tag{1.4}$$

here r is defined as the reflection coefficient and η is the admittance of the radiating medium. The admittance is inversely proportional to the intrinsic impedance. Here, Z_M and Z_0 represent the impedance of the material and free space, respectively.

Radar absorption is based on impedance matching. Impedance matching is achieved when Z_M and Z_0 are equal to each other. The impedance of free space is given by the following equation;

$$Z_0 = \frac{|\mathrm{E}|}{|\mathrm{H}|} = \sqrt{\frac{\mu_0}{\varepsilon_0}} \tag{1.5}$$

here |E| is the electric field strength and |H| is the magnetic field strength, μ_0 is the magnetic constant, ε_0 is the electric constant. Also, as a result of the calculations, Z_0 value was found as 377 Ω [13]. If the values of electric permittivity and magnetic permeability are equal, impedance matching can be achieved. Thus, the equation with minimum reflection coefficient is obtained;

$$r = \frac{Z_M - 1}{Z_0 + 1} = \frac{Z_M}{Z_0} \tag{1.6}$$

If we normalized intrinsic empedance;

$$\frac{Z_M}{Z_0} = \sqrt{\frac{\mu_r^*}{\varepsilon_r^*}} \tag{1.7}$$

where

$$\mu_r^* = \frac{\mu' - i\mu''}{\mu_0} \; and \; \varepsilon_r^* = \frac{\varepsilon' - i\varepsilon''}{\varepsilon_0} \tag{1.8}$$

μ_r^* and ε_r^* are equal if the incident medium is free space and the reflectivity is zero. Therefore, if the real and imaginary part of the magnetic permeability and the electrical permittivity are equal, then the reflection coefficient is zero [13].

We have stated that the basis of radar absorption is impedance matching and defined Z_0, the free space impedance. To achieve impedance matching, the impedance of the material, Z_M must be equal to Z_0. The material impedance (Z_M) is expressed by the following equation [14-16].

$$Z_M = Z_0 \left(\sqrt{\frac{\mu_r}{\varepsilon_r}}\right) tanh\left[j\left(\frac{2\pi f d}{c}\right)\left(\sqrt{\mu_r \varepsilon_r}\right)\right] \tag{1.9}$$

where Z_M is the impedance of absorber material, Z_0 is empedance of free space , c is the speed of electromagnetic wave in the space, f is the frequency and d is the thickness of the absorber material.

The absorption performance is evaluated by measuring the reflection loss (RL) value. The RL values of a material system can be calculated using the relative complex permeability *($\varepsilon_r = \varepsilon' - j\varepsilon''$)* and relative complex permittivity *($\mu_r = \mu' - j\mu''$)* values, according to transmission line theory. The following equation are used to determine RL [14-16].

$$RL = 20\, log\left(\frac{Z_M - Z_0}{Z_M + Z_0}\right) \tag{1.10}$$

According to the equations we have examined, the performance of radar absorbing materials varies depending on electrical permeability and magnetic permeability. We can characterise which part of the reflection loss occurs by looking at the permeability and permittivity values. In radar absorbing materials, permeability and permittivity are a function of frequency.

Therefore, the performance of the radar absorbing material can change even with small frequency changes. If the complex permeability and permittivity are known in a given frequency range, the absorber performance of the material can be determined [17].

Attenuation is a critical factor that impacts the absorption of electromagnetic waves (EW). It pertains to the rate and ability with which the energy of the incident EW is transformed into other forms of energy [18-20]. In the context of radar absorbing composite structures, attenuation represents the loss that occurs due to scattering. The formula for defining the attenuation constant (α) of a material is as follows:

$$\alpha = \frac{\sqrt{2}\pi f}{c}\sqrt{(\mu''\varepsilon'' - \mu'\varepsilon') + \sqrt{(\mu''\varepsilon'' - \mu'\varepsilon')^2 + (\mu'\varepsilon'' + \mu''\varepsilon')^2}} \tag{1.11}$$

The attenuation coefficient is a measure of how electromagnetic wave energy is absorbed or dissipated in a material. Material properties such as permeability, permittivity, and conductivity can influence it. Higher frequencies of electromagnetic waves result in increased attenuation, as the shorter wavelengths allow for closer interactions with the material and increased energy conversion. The permeability and permittivity of the material also affect the attenuation, with higher values leading to higher attenuation due to faster energy conversion. Additionally, the conductivity of the material impacts the magnitude of the attenuation coefficient. Materials with high conductivity tend to have higher attenuation constants as they effectively convert electromagnetic wave energy into heat.

Materials can experience magnetic loss through various mechanisms, such as natural resonance, domain wall resonance, eddy current loss (also known as C_0 loss), and hysteresis loss. Hysteresis loss, in the context of weak electromagnetic fields, is typically considered negligible. It is advisable to use technical term abbreviations only when they have been fully explained. Domain wall resonance becomes significant primarily at lower frequencies, typically below 2 GHz. In the gigahertz frequency range, the primary sources of magnetic loss in materials are natural resonance and eddy current loss. The formula for eddy current loss is as follows:

$$C_0 = \mu''(\mu')^{-2}f^{-1} \tag{1.12}$$

Hysteresis loss is more noticeable at higher magnetic field strengths but is often disregarded in weak electromagnetic fields due to its minimal impact on magnetic loss. On the other hand, domain wall resonance occurs at frequencies below 2 GHz and is a significant factor in magnetic loss in this low frequency range, as it involves the dynamic motion of magnetic fields within the material. In the gigahertz frequency range, natural resonance and eddy current loss are the primary sources of magnetic loss in materials. Natural resonance refers to the absorption of energy and subsequent magnetic loss due to the inherent resonant behaviour of magnetic materials at specific frequencies. Eddy current loss, also known as C_0 loss, is caused by the circulation of eddy currents in a material when exposed to rapidly changing magnetic fields, resulting in the dissipation of energy as heat.

In the context of absorbing electromagnetic waves, Debye relaxation is an essential factor that affects dielectric loss. Debye's theory can help to explain the relationship between ε' and ε" [21, 22].

$$\left(\varepsilon' - \frac{\varepsilon_s + \varepsilon_\infty}{2}\right)^2 + (\varepsilon'')^2 = \left(\frac{\varepsilon_s - \varepsilon_\infty}{2}\right)^2 \quad (1.13)$$

where ε_s and ε_∞ are static and infinite frequency dielectric constants, respectively. In some plots, like the Cole-Cole curve, the relaxation processes within materials are illustrated by the semicircles observed in the variations of ε' and ε" [23-25].

Relaxation processes refer to the gradual return of nuclear spins to equilibrium when exposed to an electromagnetic wave. These processes involve the realignment of charged particles or dipoles in response to the changing electric field of the wave. The number of semicircles on graphs like the Cole-Cole curve shows how many relaxation processes are occurring within a material. Each semicircle represents a specific relaxation time associated with a particular type of movement within the material. Therefore, more semicircles imply a more complex dielectric behaviour, suggesting the presence of multiple relaxation processes. Dielectric loss is closely linked to these processes, as energy is dissipated as heat due to internal friction or resistance encountered by moving particles or dipoles. Thus, materials with a higher number of relaxation processes tend to have greater dielectric losses, as there are more opportunities for energy dissipation.

1.2. Radar absorbing structures

Stealth technology is very important to make military vehicles such as ships, aircraft, helicopters, unmanned aerial vehicles and many military technological vehicles less detectable against radar systems. Stealth technology aims to decrease the radar cross-section (RCS) of the object targeted by the radar system. RCS can be defined as the ratio of incident and reflected power. The main factors affecting the RCS are the size and shape of the object and the material used. There are two basic methods to implement stealth technology. One is to reduce the radar cross-section by changing the shape and size of the object so that electromagnetic waves are reflected in different directions. The second is to cover the surfaces of objects with radar-absorbing materials that absorb electromagnetic waves. In order to reduce RCS, these two methods must be well understood.

1.2.1 Shape of military vehicles

To change the direction of the electromagnetic wave hitting the target and reduce its reflection, the surface and corners of the target are modified. In military vehicles, sharp angles and flat surfaces are used to reduce the reflection of electromagnetic waves. Figure 1.3 shows the design of a fighter jet with smooth surfaces and sharp angles and an ordinary passenger plane. The airliner has a smooth surface which reflects the waves from the radar. This is because the RCS of the airliner is high. The fighter plane, on the other hand, has a design with sharp and pointed surfaces that scatter the radar signals in different directions. This result shows that the RCS of the fighter plane is low.

Figure 1.3. Passenger plane and fighter jet designs.

Stealth aircraft are designed to achieve reduced visibility by using various stealth technology applications that reduce the reflection of electromagnetic waves [26]. The aircraft to which stealth technology was first applied is the F-111 Nighthwak operational aircraft [27]. Figure

1.4 shows the so-called first generation aircraft with stealth technology, F-111 Nighthwak, B-2 Spirit and B-21 Raider, respectively.

Figure 1. 4. First generation aircraft with stealth technology a) F-111 Nighthwak, b) B-2 Spirit, c) B-21 Raider.

Furthermore, stealth aircraft technology has continued to evolve after the first generation. Figure 1.5 shows the latest generation of stealth aircraft developed as a result of the studies carried out, respectively Lockheed Martin F-35 Lightning II, Chengdu J-20 and Sukhoi Su-57.

Figure 1.5. Latest generation of stealth aircraft a) Lockheed Martin F-35 Lightning II, b) Chengdu J-20, c) Sukhoi Su-57.

A stealth ship is a ship built using stealth technology to make it difficult to be detected by radar, sonar, etc. RCS reduction for stealth ships is a relatively new concept because there are also some applications for ships such as wake and acoustic signature reduction. Figure 1.6 shows various warships with stealth technology.

Figure 1.6. Warships with stealth technology a) Type 055 destroyer, b) ENS El Fateh (Gowind-class design) c) USS Zumwalt (Zumwalt-class destroyer).

Stealth technology has been applied to land vehicles as well as air and sea vehicles. The corners, front and rear surfaces of land vehicles are designed with sharp angles to reduce RCS. Figure 1.7 shows various land vehicles with stealth technology.

Figure 1.7. Land vehicles with stealth technology **a)** FV4034 Challenger 2, **b)** GTK Boxer, **c)** PL-01.

1.2.2. Radar absorbing materials

According to the studies and sources in the literature, radar absorbing materials have different absorber groups. The main characteristics of these absorber groups are magnetic permeability and dielectric permeability. Many materials such as conductive, magnetic, ceramic, metal, carbon, polymer, etc. can be considered as radar absorbing materials. The basic radar absorbing materials are described in the subheadings below.

1.2.2.1. Dielectric absorbers

Since dielectric absorber materials alone have low dielectric loss factors they have low electromagnetic wave absorption. Therefore, dielectric absorber materials are used in composite structures obtained by using conductive fillers. Semiconductors, metal oxides, graphite, carbon black, metals, etc. are conductive filler materials [28]. By changing the proportions in the composite structure, magnetic permeability and dielectric permittivity

values that will provide optimum impedance matching can be obtained. In addition, since the density of such materials is low, they are preferred in military vehicles.

1.2.2.2. Magnetic absorbers

Ferrite, radar absorbing materials consist of a combination of iron oxide and other metals. The ferrite spinel structure is denoted by MFe_2O_4. Here, M stands for metal ions with two valence electrons. In addition, ferrites with a crystal structure have a cubic structure. Ferrite structure is divided into two as soft and hard. When soft ferrites are exposed to an external magnetic field, their magnetisation can be easily changed. However, hard ferrites, unlike soft ferrites, do not easily change their magnetisation when exposed to an external magnetic field because they have a high coercive field. Soft ferrites are of great interest in radar absorption as they can easily interact with external magnetic fields. In addition, the fact that ferrites are ceramic materials gives them resistance to high temperatures and the ability to exhibit magnetic properties at high temperatures [29]. For the reasons mentioned above, ferrites play an important role in radar absorbing materials. They are generally used in composite radar absorber structures to provide magnetic interaction. In addition, ferrite radar absorbing materials are used in stealth aircraft and ships because they effectively absorb frequency ranges in the order of GHz.

1.2.2.3. Oxide absorbers

Materials with a large and effective capacity of oxygen anion bound to metal-centred atoms to absorb electromagnetic wave are oxide materials. Oxide-based materials are radar absorbing materials with the ability to utilise both magnetic loss and dielectric loss mechanism [30]. With these properties, they have the potential to absorb electromagnetic waves in wide bandwidth.

1.2.2.4. Polymeric composites

Composite materials are structures formed by combining at least two insoluble materials with different chemical and physical properties. Composite materials consist of matrix and reinforcement materials dispersed in the matrix. In order for the reinforcement materials to show their properties, the mechanical properties of the matrix structure are expected to be good. Epoxy is generally preferred as the matrix in radar absorbing composite structures. The reasons for the preference of epoxy can be listed as easy applicability, wear and corrosion

resistance, adhesion strength and high heat resistance etc. In radar absorbing composite structures, electromagnetic wave absorption capacity is increased to high levels by adding magnetic and dielectric material into epoxy.

1.3. Magnetism

Magnetism can be defined as a physical phenomenon produced by a magnetic field. An elementary particle or electric current can generate a magnetic field. This magnetic field can also affect other currents and moments. The magnetic field can affect any material up to a certain level. Materials in nature exhibit different types of magnetic properties due to their inherent magnetic moments. The magnetic properties of a material vary depending on factors such as temperature, pressure and applied magnetic field. Depending on the variation of these factors, a material can exhibit more than one magnetic property. The use of magnetic materials in electronic devices has gained importance with the development of technology. Magnetic materials are of great importance in the field of electronic warfare due to technological advancements. To understand the effects of magnetic materials used in advanced materials, it is necessary to study the basics of magnetism.

1.3.1. Basics of magnetism

According to the classical atomic model, electrons rotate around the nucleus at radius (r) and velocity (V) and create an (I) current in the opposite direction of this rotational motion. This current loop creates the magnetic moment ($\vec{\mu}$) ($\vec{\mu}= I\vec{A}$, here $\vec{A}$ is a normal area vector). Figure 1.8 shows the motion of electrons around the nucleus.

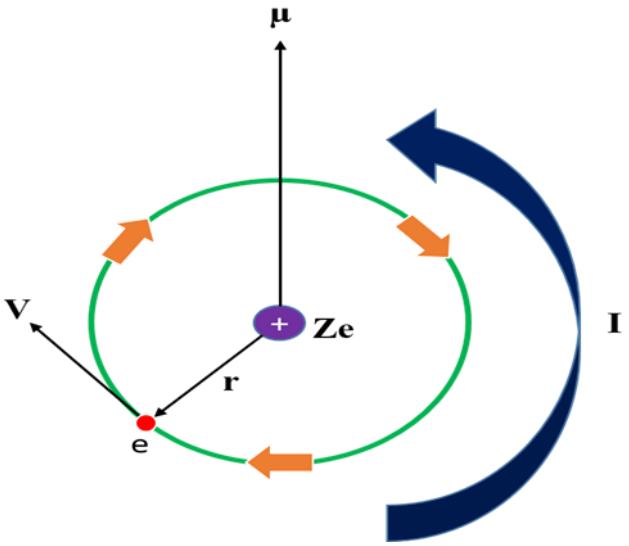

Figure 1.8. Magnetic moment generation by the current loop of an electron rotating with velocity V at radius r around the nucleus.

The electric current in the electron-nucleus structure of the elementary hydrogen atom is expressed as follows;

$$I = \frac{eV}{2\pi r} \tag{1.14}$$

Here, V is the electron velocity and e is the electron charge. The magnetic moment equation is expressed as follows;

$$|\vec{\mu}| = |I\vec{A}| = \frac{eV}{2\pi r}\pi r^2|\hat{A}| \tag{1.15}$$

The orbital angular momentum of an electron moving around a nucleus is defined as follows;

$$\vec{L} = m\vec{V} \times \vec{r} \tag{1.16}$$

If we apply the orbital angular momentum to Eq. (14), we get the following equation;

$$|\vec{\mu}| = \frac{1}{2}eVR|\vec{A}| = \frac{e}{2m_e}|\vec{L}| = \gamma|\vec{L}| \tag{1.17}$$

where γ is the gyromagnetic ratio. Moreover, there is a spin angular momentum derived from the S^2 operator in addition to the orbital angular momentum, and its equation is as follows;

$$\hat{S}^2\chi = \hbar^2 S(S+1)\chi \tag{1.18}$$

The quantized spin angular momentum can be defined as follows;

$$\left|\vec{S}\right| = \hbar\left|\sqrt{s(s+1)}\right| \tag{1.19}$$

The following expression refers to the spin magnetic momentum;

$$|\mu_s| = \gamma\left|\vec{S}\right| = \gamma\hbar\sqrt{s(s+1)} \tag{1.20}$$

The magnetic moment resulting from the spin and orbital angular momentum, as explained in the equations above, can be expressed as the Bohr magneton ($\mu_B = e\hbar/2m_e$).

$$|\mu_s| = \gamma\left|\vec{S}\right| = \mu_B\sqrt{s(s+1)} \tag{1.21}$$

$$|\mu_l| = \gamma\left|\vec{L}\right| = \mu_B\sqrt{l(l+1)} \tag{1.22}$$

The equation defined below reveals the contribution of orbital and spin angular momentum;

$$\left|\mu_j\right| = \gamma\left|\vec{J}\right| = \mu_B\sqrt{j(j+1)} \tag{1.23}$$

The total angular momentum quantum number, represented by j, is the sum of the orbital angular momentum and spin angular momentum.

$$\vec{J} = \vec{L} + \vec{S} \tag{1.24}$$

1.3.2. Classification of magnetic materials

As previously explained, magnetism originates from the interaction between the orbital and spin motions of electrons. All materials in nature have magnetic properties, but the reactions of materials to magnetic fields are different from each other. Magnetic materials can be classified based on the collective interaction of atomic magnetic moments. Some materials exhibit a strong interaction between atomic moments, while others do not. Therefore, magnetic materials are classified into 5 main different groups: Diamagnetic, Paramagnetic, Ferromagnetic, Antiferromagnetic and Ferrimagnetic. In this thesis, only ferromagnetism will be analyzed in detail since ferromagnetic materials are used.

1.3.2.1. Ferromagnetism

Commonly thought of magnetic materials include iron, nickel, and magnetite due to their ferromagnetic properties. Ferromagnetic materials form the magnetic moment patterns of atoms through spin bonds formed by paired electrons. Moreover, all ferromagnetic materials exhibit different magnetic behavior at certain temperature values due to thermal fluctuations. This temperature value is called the Curie temperature. Ferromagnetic materials exhibit much stronger interactions between atomic moments compared to other magnetic materials. These interactions are due to electronic exchange forces, which cause the atomic moments to align either parallel or antiparallel. As a result, ferromagnetic materials have a large number of unpaired electron spins [31]. In summary, ferromagnetic materials exhibit permanent magnetic properties even without the application of an external magnetic field. Examples of ferromagnetic materials include iron (Fe), magnetite (Fe_3O_4), nickel (Ni), cobalt (Co) and some rare earth elements (Gd, ie).

Figure 1.9a-b shows the behavior of the magnetic moments of a ferromagnetic material in the absence and presence of an external magnetic field. As seen in Figure 1.9a, magnetic materials are composed of many domains and the domains have their own magnetic moments. In Figure 1.9b, as a result of the magnetic field applied externally on the ferromagnetic material, the magnetic moments in the domains change in the direction of the applied magnetic field and thus its magnetism increases. This magnetization amount is higher than paramagnetic materials.

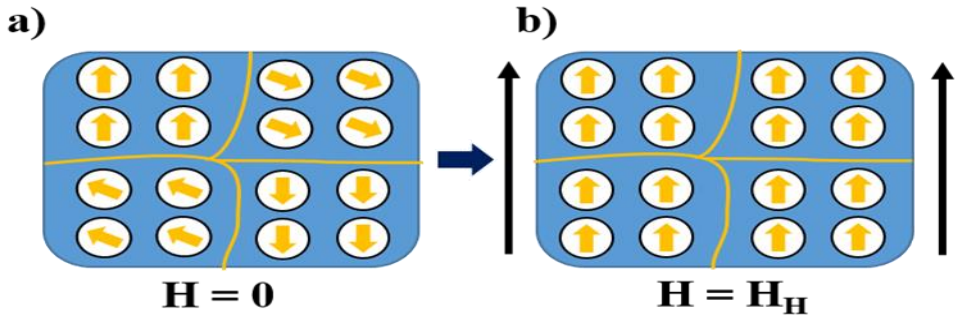

Figure 1.9. Regulation of magnetic moments of a ferromagnetic material a) no external magnetic field was applied b) an external magnetic field was applied.

Ferromagnetic materials show a nonlinear behavior under a magnetic field and are irreversible [31]. This behavior is illustrated in Figure 1.10a, which shows the response of a ferromagnetic material to an applied magnetic field. Also, Figure 1.10b-c shows the hysteresis curves of the response of hard and soft ferromagnetic materials to an externally applied magnetic field.

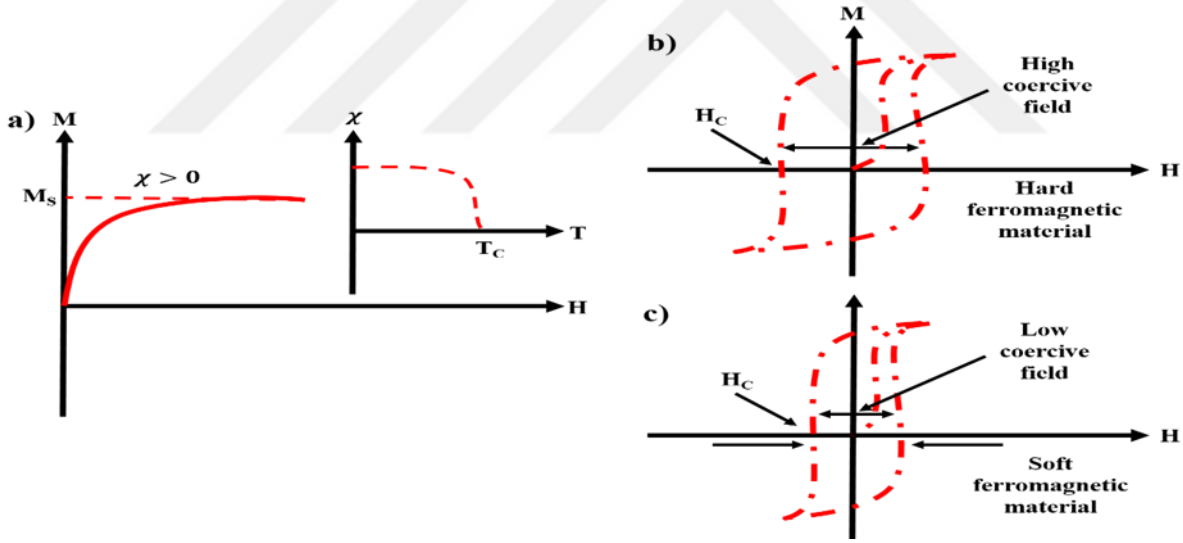

Figure 1.10. a) M-H and χ - T curves of ferromagnetic materials b) hysteresis curves of hard and c) soft ferromagnetic materials.

Figure 1.10a shows that when an external magnetic field is applied to a ferromagnetic material, the atoms in the material structure begin to align and orient in the direction of the applied magnetic field. The magnetization of the material increases rapidly and the

ferromagnetic material reaches the saturation magnetization value *(Ms)* as the amount of applied magnetic field increases.

From Figure 1.10b it is clear that hard ferromagnetic materials have a large coercive field *(Hc)*. In this type of hard ferromagnetic material, when sufficient magnetic field is applied, the material becomes ductile and gains permanent magnetization. Figure 1.10c shows that soft ferromagnetic materials have a low coercive field.

1.3.2.2.Ferrimagnetism

The atoms in ferrimagnetic materials have a net magnetic moment and the magnetic moments in the atoms are in a non-parallel arrangement. Moreover, the magnitudes of the magnetic moments of the atoms are different. Since the magnetic moment magnitudes are different, they cannot annihilate each other. Therefore, they have net magnetization. However, the magnetic saturation value of ferrimagnetic materials is lower than ferromagnetic materials. Figures 1.11a-b indicate the behavior of the magnetic moments when no external magnetic field is applied to the ferrimagnetic material and when it is applied, respectively.

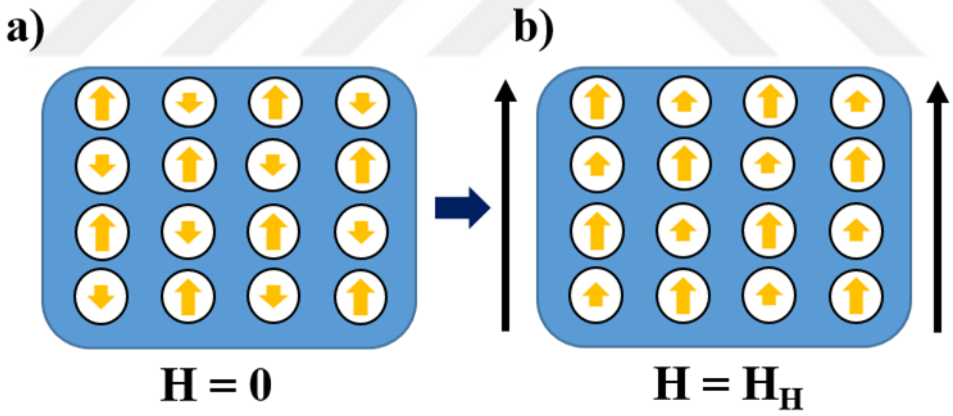

Figure 1.11. Regulation of magnetic moments of material exhibiting ferrimagnetic behavior a) no external magnetic field was applied, and b) an external magnetic field was applied.

Figure 1.12 indicates the performance of the magnetic saturation of a ferrimagnetic material in the presence of a magnetic field. The reaction of a ferrimagnetic material to an externally applied magnetic field is very similar to that of a ferromagnetic material.

However, the magnetic saturation value is lower than that of ferromagnetic materials. This is because the magnitudes of the magnetic moments of the atoms in ferrimagnetic materials are different from each other.

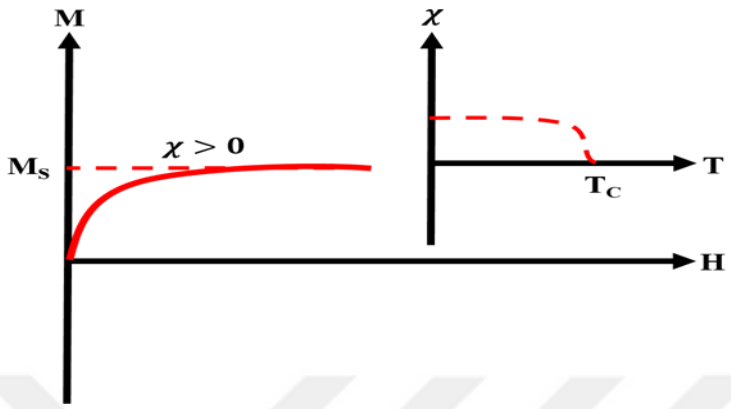

Figure 1.12. M-H and $\chi - T$ graph of ferrimagnetic materials.

1.3.3. Magnetic hysteresis loop

Curves showing the complex change in magnetization of ferromagnetic and ferrimagnetic materials with an applied magnetic field are called hysteresis curves. Hysteresis curves give many magnetic properties of materials. The saturation magnetization *(M_S)*, permanent magnetization *(M_R)* and coercive field *(H_C)* of the material are obtained from hysteresis curves. Moreover, it is also used to determine the softness and hardness of the material. Figure 1.13 illustrates the hysteresis loop of a classical multi-field magnetic material.

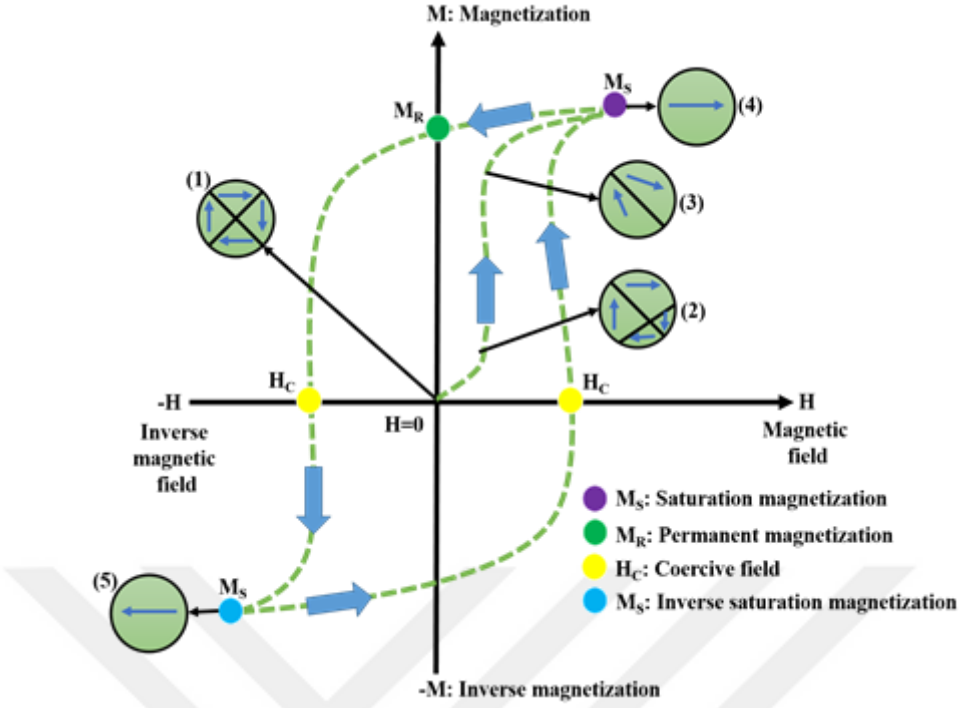

Figure 1.13. Hysteresis loop of a multi-domain magnetic material.

Ferromagnetic and ferrimagnetic materials exhibit a net magnetization value even in the absence of an external magnetic field. When an external magnetic field is applied, the magnetization of the object increases rapidly and reaches the magnetic saturation value *(M_S)*. When the effect of the external magnetic field is removed, the materials usually exhibit permanent magnetization *(M_R)*. Furthermore, we can determine whether materials are magnetically hard or soft by looking at the coercive field *(H_C)* value.

2. THEORETICAL FOUNDATIONS AND LITERATURE REVIEW

The physical theory of electromagnetic wave absorption describes the interaction of electromagnetic waves with objects. These waves come in energy packets of different frequencies and wavelengths. When an object absorbs electromagnetic waves, it takes energy, which is then transformed into internal energy by the object. The object can re-emit this energy, but the process varies depending on the structure and composition of the object. The absorption spectrum indicates that the object selectively absorbs waves of particular frequencies. In addition, electromagnetic waves may get scattered or transmitted through the object. The theory of electromagnetic wave absorption facilitates comprehension of the ways in which different objects interact with these waves, and how they do so, and has important applications in fields such as materials science and optics.

In this part of the thesis, studies on the characterization of radar absorbing materials and composites will be briefly reviewed. Thus, a brief summary of the literature on radar absorbing systems will be obtained.

Xian et al. (2023) synthesized rhombohedral dodecahedral Co/C nanocomposites with desirable porous structures by hydrothermally synthesizing zeolitic imidazolate framework-67 (ZIF-67) and thermally annealing it. They were then coated on the surface of the Co/C nanocomposites with a rod-shaped polyaniline layer via in situ polymerization. The effect of the mass ratio of polyaniline to Co/C on the electromagnetic properties of the nanocomposites was also studied. The study found that the Co/C@PANI-2 sample had an optimal reflection loss of -67.67 dB at a 50% filling ratio and an effective absorption bandwidth of 5.02 GHz. They revealed that the rod-like polyaniline coating improved the electromagnetic properties and impedance matching of the nanocomposite structures [32].

Luo et al. (2022) prepared porous PANI/SBA-15 composites through in situ chemical oxidative polymerization. The absorption capacity of PANI/SBA-15 composites can be effectively controlled by varying the amount of PANI. The PANI/SBA-15 composite with 0.35 mL of aniline monomer demonstrated the best EMW absorption performance, with a minimum reflection loss of -54.20 dB at a matching thickness of 2.4 mm. The results

suggested a favorable coupling effect between impedance matching and loss characteristics. The effective absorption bandwidth was up to 6.00 GHz at 2.15 mm. [33].

Pan et al. (2023) prepared $NiCo_2O_4$@Fe_3O_4 composites with excellent electromagnetic wave absorption performance using the co-precipitation method at low temperature (50 °C). The combination of $NiCo_2O_4$ with a 3D hierarchical flower-like structure and Fe_3O_4 with a spherical structure increased the specific surface area of the composite material, facilitating the full reflection and scattering of electromagnetic waves. The researchers improved the absorption loss performance of electromagnetic waves by using a combination of typical magnetic material and excellent dielectric material, which allowed them to adjust the impedance matching value of the material. The study discovered that the maximum RL value for a 2.0 mm thickness was -53.35 dB at approximately 13 GHz. Additionally, the effective absorption bandwidth was 4.4 GHz when the weight ratio of composite samples ($NiCo_2O_4$:Fe_3O_4) was 6:1.[34].

Zeng et al. (2023) employed HF etching, KOH shearing, and high-temperature molten salt techniques to fabricate layered MXene (L-MXene), network-like MXene nanoribbons (N-MXene NRs), porous MXene monolayer (P-MXene ML), and porous MXene layer (P-MXene L). These materials exhibited suitable microstructures and surface features for EMW absorption performance. The researchers utilized HF, KOH, and KCl/LiCl for MXene functionalization, enabling the tuning of microstructure and surface states (F-, OH-, and Cl-terminals). This modification enhanced the EMW absorption capacity of MXene-based nanostructures. Consequently, L-MXene, N-MXene NRs, P-MXene ML, and P-MXene L samples demonstrated reflection loss (RL) values of -43.14, -63.01, -60.45, and -56.50 dB, respectively, with matching thicknesses of 0.95, 1.51, 3.83, and 4.65 mm, respectively. [35].

Deng et al. (2023) created MnO_2/Carbon foam (MCF) composites with adjustable morphology through a straightforward hydrothermal and annealing process. They observed that varying the $KMnO_4$ concentration facilitated the morphological transformation of MnO_2, introducing defects that reduced conductive loss, optimized impedance matching, enhanced polarization loss, and induced multiple scattering. Consequently, the MCF composite exhibited a remarkable minimum reflection loss of -65.18 dB at 3.19 mm, along with a broad effective absorption bandwidth encompassing the entire X band. Despite the involvement of

various dispersion mechanisms, the outstanding performance of MCF composites was predominantly attributed to defects modulated by morphology [36].

Dong et al. (2023) fabricated reduced graphene oxide (rGO) nanosheets adorned with hollow core-shell Fe_3O_4@PPy (FP) microspheres using a hybrid approach involving hydrothermal, in situ polymerization, directional freeze-drying, and hydrazine vapor reduction methods. The resulting Fe_3O_4@PPy/rGO (FPG) composite exhibited outstanding EMW absorption performance, featuring a minimum reflection loss of -61.20 dB at 1.89 mm and an effective absorption bandwidth spanning 5.26 GHz at 1.71 mm. The authors attribute the exceptional performance of the heterostructure to the synergistic effects of conductive loss, dielectric loss, magnetic loss, multiple reflection loss, and optimized impedance matching [37].

Zhang et al. (2023) employed a microwave-assisted hydrothermal process to synthesize MoS_2 nanosheets with varying Fe concentrations. Microstructure analysis revealed that Fe doping promotes the formation of MoS_2 nanosheets with a mixed 1T/2H phase. Benefiting from improved permittivity and permeability properties, enhanced impedance matching, and attenuation properties resulting from doping and partial phase transformation, the Fe-doped 1T/2H-MoS_2 nanosheets demonstrated remarkable electromagnetic wave absorption capabilities. The maximum reflection loss was reported to be -60.03 dB at a matching thickness of 5.65 mm, and the effective absorption bandwidth below -10 dB was measured at 5.33 GHz [38].

Yu et al. (2023) utilized a two-step method to synthesize CoNi/$MoSe_2$ composites. Initially, they synthesized flower-like $MoSe_2$ through a hydrothermal method, followed by the loading of CoNi alloy on the $MoSe_2$ surface using the electrolysis coating method. To assess the impact of different Co/Ni molar ratios on the absorption performance of CoNi/$MoSe_2$ composites, they prepared three samples with Co/Ni molar ratios of 1:3, 1:1, 3:1, and two additional samples containing only one metal (Ni or Co). The optimal electromagnetic wave absorption performance was observed for the CoNi/$MoSe_2$ composite with a Co/Ni ratio of 1:3. The minimum reflection loss was reported as -48.6 dB with a matching thickness of 1.8 mm, and the largest effective absorption bandwidth was 3.76 GHz at a matching thickness of 1.4 mm. [39].

Chen et al. (2023) created an Ag^{+}-doped α-MnO_2 with a hierarchical structure for EMW absorption. They enhanced EMW absorption performance significantly by concurrently adjusting microscopic morphology and crystal defects. The optimal reflection loss reached -68.6 dB, and an effective absorption bandwidth of 4.2 GHz was attained at a thin thickness of 1.43 mm. This simultaneous achievement of thin thickness, heightened absorption intensity, and expanded absorption bandwidth were highlighted in their findings. [40].

Yang et al. (2023) employed an in situ sacrificial template method to synthesize the $CoMoO_4$@ZIF-67 precursor, which was subsequently subjected to a calcination process to yield porous Mo_2C@cobalt/carbon (Mo_2C@Co/C) composites. The novel in-situ fabrication strategy led to the homogeneous dispersion of Mo_2C and Co nanoparticles, along with the formation of porous structures. This approach facilitated the creation of abundant interfaces and effective multiple loss mechanisms, including polarization loss, conductivity loss, and magnetic loss. The optimized composite, Mo_2C@Co/C-10, demonstrated superior electromagnetic wave absorption performance, achieving a maximum reflection loss value of -37.9 dB at a matching thickness of 2.3 mm and an effective absorption bandwidth of 5.52 GHz at 1.9 mm. [41].

In this thesis, PANI, Fe_3O_4 and MoS_2 will be synthesized by polymerization, co-precipitation and hydrothermal methods, respectively. Then, Fe_3O_4 nanoparticles will be decorated on MoS_2 at different ratios (5 wt%, 10 wt%, 15 wt%, 20 wt%). PANI will be coated on the Fe_3O_4 decorated MoS_2 samples at different ratios (25 wt%, 50 wt%, 75 wt%). Thus, PANI@Fe_3O_4:MoS_2 nano hybrid structure will be obtained. Reflection loss in PANI@Fe_3O_4:MoS_2 hybrids can be attributed to four key factors. First, the good impedance matching in hybrid structures ensures that electromagnetic waves entering the hybrid penetrate in a wide frequency range. Second, due to the composition and morphology of the hybrid, the incident electromagnetic waves can exhibit multiple dispersion. Thirdly, dielectric loss plays an critical role in EMW absorption because it shows properties such as accumulation of free charges in the hybrid structure, interface polarization and energy storage. The hybrid structure benefits from high conductivity due to polarized electrons circulating between PANI and MoS_2 nanosheets, which helps dissipate EMW. This mechanism, along with the Fe_3O_4 decoration of MoS_2 nanosheets and PANI polymer coating, is expected to result in a high and broadband EMW absorption performance.

3. METHODOLOGY

In this section, the co-precipitation, hydrothermal and in situ chemical oxidative polymerization methods used to synthesis Fe_3O_4, MoS_2 and PANI will be described. Preparation procedures of nanomaterials required for PANI@Fe_3O_4:MoS_2 nano hybrid structure and radar absorbing composite structures will be explained. Characterization techniques for the study of structural, morphological, elemental, thermal, magnetic and electromagnetic properties of nanoparticles will be described in this chapter.

3.1. Co-precipitation method

Co-precipitation is the process of precipitating multiple compounds simultaneously from a solution. It is the most convenient and cheapest method especially for nanoparticle synthesis. In this method, the metal is precipitated as a hydroxide in a solvent in basic media under the guidance of a salt. Figure 3.1 shows the flow diagram for co-precipitation.

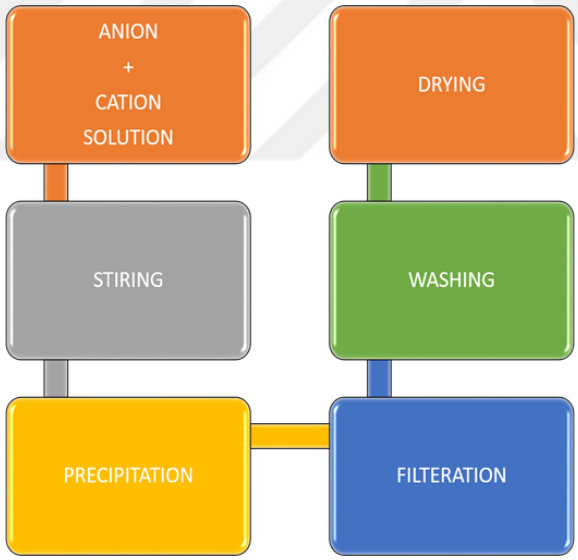

Figure 3.1. Stages of the classical co-precipitation method.

The solutions containing cations and anions are stirred continuously to precipitate the hydroxide. The precipitate is then separated from the solution through flotation. Next, the destruction process is carried out. Finally, it is dried to ensure oxide formation. During the co-precipitation process, several processes occur, including initial nucleation, growth,

coarsening, agglomeration, and ripening. The release of anions and cations in a controlled manner regulates the kinetics of nucleation and particle growth, ensuring the formation of nanoparticles that are monodisperse [42].

3.2. Hydrothermal method

The hydrothermal method refers to heterogeneous reactions that allow the synthesis of inorganic materials in aqueous media by adjusting the ambient temperature and pressure. Figure 3.2a-b shows a classical stainless steel autoclave used in the hydrothermal method and the steps of the hydrothermal method. The synthesis takes place by heating the aqueous mixture of starting salts in a stainless steel autoclave above the boiling point of water. The critical point here is that the temperature above the boiling point of water creates an internal pressure in the closed environment that is significantly higher than atmospheric pressure. The effect of high pressure and temperature provides a one-step process to synthesize materials with high crystallinity without the need for post-annealing processes.

Magnetic nanomaterials and various nanomaterials can be synthesized by the hydrothermal method. In the hydrothermal method, parameters such as the amount of starting salts, solvent, stabilizing agents and reaction temperature and time significantly affect the structure and morphology of the materials. One of the disadvantages of the hydrothermal method is the low product yield compared to other methods.

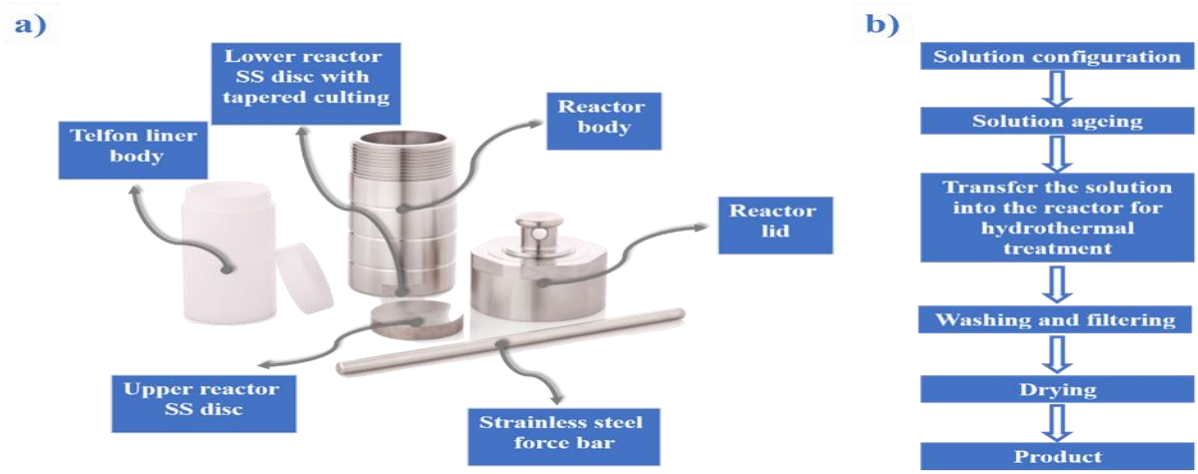

Figure 3.2. a) Schematic diagram of typical hydrothermal apparatus, and b) typical synthesis procedure of hydrothermal method.

In a classic hydrothermal method, the solution is first prepared. Then it is aged. The resulting solution is then transferred to a stainless steel autoclave. It is placed in the furnace by adjusting the temperature and reaction time according to the material to be obtained. The solution coming out of the furnace is centrifuged several times and finally the product is obtained after drying.

3.3. Oxidative polymerization method

The process of synthesizing polymeric (oligomeric) products from different classes of monomers is known as oxidative polymerization [43]. Monomers used in oxidative polymerization are expected to have significant electron-donating properties and a high tendency towards oxidation. The monomer undergoes oxidation due to either the oxidizing agent or the applied potential. Thus, the monomer (or polymer) molecule forms cation or cation radical sites, initiating polymerization [43].

Figure 3.3. Oxidative polymerisation method for polyaniline.

PANI synthesized via chemical oxidation polymerization is produced using hydrochloric acid (HCl) as a dopant and ammonium persulfate (APS) as an oxidant in an aqueous solution [43]. Currently, with the aid of a proton oxidant, the aniline monomer can be separated without forming a strong bond or producing impurities. The oxidant polymerisation method is commonly used to synthesise PANI. Aniline is allowed to react with an acidic substance with the help of a neutralising agent, followed by the addition of an oxidising agent such as APS at varying temperatures. After completion, the polymerisation mechanism takes three hours and the resulting aqueous solution is separated by filtration. Technical abbreviations are explained in the first use. PANI in its pure form can be obtained by rinsing the solution mentioned above with deionized water 5-6 times. Finally, drying at 80 °C gives PANI in green colour.

3.4. Synthesis of nanomaterials

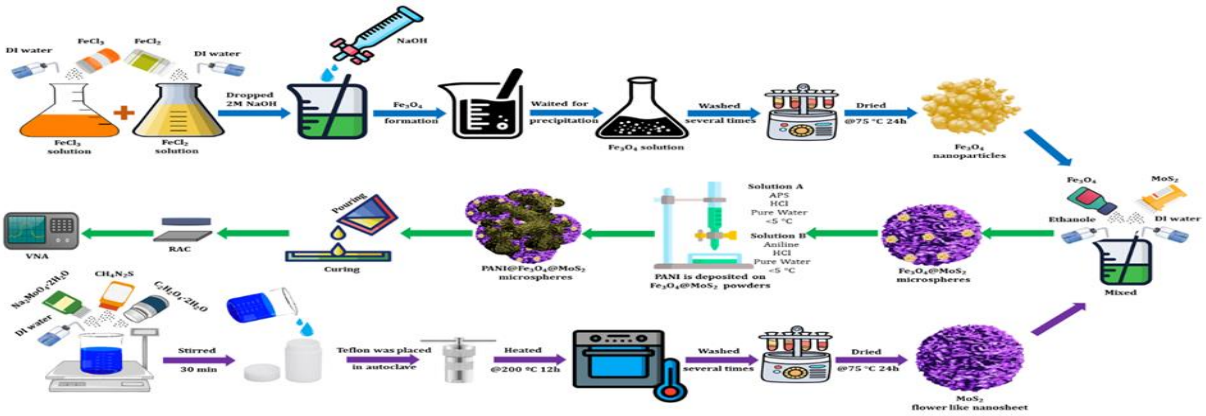

Figure 3.4. Schematic illustration showing the process of synthesizing nanoparticles and composites, followed by measuring the electromagnetic parameters of the resulting hybrid structures.

3.4.1. Materials

Sodium molybdate dihydrate ($Na_2MoO_4 \cdot 2H_2O$, Sigma-Aldrich, ≥99.5%) and thiourea (CH_4N_2S, Sigma-Aldrich, high purity) were utilized as precursors for the synthesis of MoS_2 NSs. Deionized (DI) water was employed as the solvent and oxalic acid ($C_2H_2O_4 \cdot 2H_2O$, Sigma-Aldrich, high purity) was added as an acidity regulator and sheet separator during synthesis. Iron (III) chloride hexahydrate- $FeCl_3.6H_2O$ (Sigma-Aldrich), Iron (II) chloride tetrahydrate- $FeCl_2.4H_2O$ (Sigma-Aldrich), and Sodium hydroxide-NaOH (Sigma-Aldrich) were utilized to synthesize Fe_3O_4 nanoparticles. The final composite samples were manufactured using epoxy resin ($C_{21}H_{25}ClO_5$, BRTR Chemistry) and hardener.

.4.2. Synthesis of MoS_2 nanosheets

The experiment began by weighing appropriate amounts of sodium molybdate and thiourea. These were then sequentially dissolved in 55 mL of deionized water at room temperature. Next, the necessary amount of oxalic acid was gradually added to the solution. The solution was stirred at 800 rpm for 30 minutes before being transferred into a 100 mL hydrothermal vessel lined with Teflon. The hydrothermal reactor was then heated to 200°C for 12 hours. After completing the reaction, the resulting particles underwent multiple washes with DI

water and ethanol. Each cycle involved centrifugation at 9000 rpm for 10 minutes. The washed sample was then dried in an atmospheric oven at 80°C for 24 hours. The schematic synthesis process of MoS_2 nano sheets is illustrated in Figure 3.4.

3.4.3 Synthesis of Fe_3O_4 nanoparticles

To synthesize Fe_3O_4 nanoparticles, first dissolve $FeCl_2.4H_2O$ and $FeCl_3.6H_2O$ in an appropriate amount of DI water at a ratio of 1:2. Next, slowly add 2M NaOH solution dropwise to the mixture. The formation of Fe_3O_4 in black color will be visible. Allow the Fe_3O_4 nanoparticles to settle to the bottom of the beaker. Finally, synthesize the Fe_3O_4 nanoparticles using centrifugation at 9000 rpm for 10 minutes per cycle. The Fe_3O_4 nanoparticles were repeatedly washed with DI water and ethanol before being dried for 24 hours at 80°C. Figure 3.4 shows the schematic process for synthesizing Fe_3O_4 nanoparticles.

3.4.4. Synthesis of Fe_3O_4:MoS_2 hybrids

Figure 3.4 demonstrates the decoration of Fe_3O_4 nanoparticles on MoS_2 nanosheets. The appropriate weight ratio (5 wt%, 10 wt%, 15 wt%, 20 wt%) of Fe_3O_4 nanoparticles and MoS_2 were individually dissolved in DI water and ethanol through stirring for 30 minutes. After that, the Fe_3O_4 solution was combined with the MoS_2 solution and stirred for 30 minutes. Subsequently, the solutions underwent multiple washes with DI water and ethanol. Finally, they were dried at 80°C for 24 hours, successfully decorating the Fe_3O_4 nanoparticles on MoS_2 nanosheets.

3.4.5. Synthesis of PANI@Fe_3O_4@MoS_2, PANI@Fe_3O_4 and PANI@MoS_2 hybrids

PANI was synthesized on Fe_3O_4, MoS_2, and Fe_3O_4: MoS_2 nanostructures using oxidative polymerization with an appropriate amount of aniline in 1 M HCl and APS as an oxidizing agent. Table 1 shows the composition of the composites, the PANI, Fe_3O_4 and MoS_2 contents and the code numbers for the hybrid composites produced. The particles were weighed with a balance, dispersed in HCl solution, and mixed with APS and aniline solutions, which were prepared separately under an ice bath. The bath temperature remained below 5°C throughout the experiment. APS solution was cautiously added to the aniline solution with constant stirring. The resulting mixture was washed with distilled water and the residual solution was then dried in an oven at 80°C for 24 hours to produce the desired powders.

3.4.6. Radar Absorbing Composite Manufacture

To create the final electromagnetic absorbent composite structure, Fe_3O_4, MoS_2, PANI@Fe_3O_4, PANI@MoS_2, Fe_3O_4:MoS_2, and PANI@Fe_3O_4:MoS_2 particles (30 wt%) were distributed in epoxy resin (70 wt%). For 30 minutes, a mixer was used to homogeneously mix the resin. The combination was then given the curing agent. To avoid the production of gas bubbles, the mixture was then poured into a silicone mold with toroidal-shaped geometry ($\boldsymbol{\phi_{out}}$ =7.00 mm and $\boldsymbol{\phi_{in}}$ =3.00 mm) and placed in a vacuum chamber (100 mbar) for 24 hours at ambient temperature.

Table 3.1. The codes, contents (wt.%), and structures of the synthesized samples are presented.

Sample Codes	PANI (wt%)	Fe_3O_4 (wt%)	MoS_2 (wt%)	Structure
F	0	100	0	Fe_3O_4
M	0	0	100	MoS_2
P	100	0	0	PANI
$\mathbf{F_5M_{95}}$	0	5	95	Fe_3O_4@MoS_2
$\mathbf{F_{10}M_{90}}$	0	10	90	Fe_3O_4@MoS_2
$\mathbf{F_{15}M_{85}}$	0	15	85	Fe_3O_4@MoS_2
$\mathbf{F_{20}M_{80}}$	0	20	80	Fe_3O_4@MoS_2
$\mathbf{P_{25}F_{75}}$	25	75	0	PANI@Fe_3O_4
$\mathbf{P_{50}F_{50}}$	50	50	0	PANI@Fe_3O_4
$\mathbf{P_{75}F_{25}}$	75	25	0	PANI@Fe_3O_4
$\mathbf{P_{25}M_{75}}$	25	0	75	PANI@MoS_2
$\mathbf{P_{50}M_{50}}$	50	0	50	PANI@MoS_2
$\mathbf{P_{75}M_{25}}$	75	0	25	PANI@MoS_2
$\mathbf{P_{25}F_{3.75}M_{71.25}}$	25	3.75	71.25	PANI@Fe_3O_4:MoS_2
$\mathbf{P_{50}F_{2.5}M_{47.5}}$	50	2.5	47.5	PANI@Fe_3O_4:MoS_2
$\mathbf{P_{75}F_{1.25}M_{23.75}}$	75	1.25	23.75	PANI@Fe_3O_4:MoS_2
$\mathbf{P_{25}F_{7.5}M_{67.5}}$	25	7.5	67.5	PANI@Fe_3O_4:MoS_2
$\mathbf{P_{50}F_5M_{45}}$	50	5	45	PANI@Fe_3O_4:MoS_2
$\mathbf{P_{75}F_{2.5}M_{22.5}}$	75	2.5	22.5	PANI@Fe_3O_4:MoS_2
$\mathbf{P_{25}F_{11.25}M_{63.75}}$	25	11.25	63.75	PANI@Fe_3O_4:MoS_2
$\mathbf{P_{50}F_{7.5}M_{42.5}}$	50	7.5	42.5	PANI@Fe_3O_4:MoS_2
$\mathbf{P_{75}F_{3.75}M_{21.25}}$	75	3.75	21.25	PANI@Fe_3O_4:MoS_2
$\mathbf{P_{25}F_{15}M_{60}}$	25	15	60	PANI@Fe_3O_4:MoS2
$\mathbf{P_{50}F_{10}M_{40}}$	50	10	40	PANI@Fe_3O_4:MoS_2
$\mathbf{P_{75}F_5M_{20}}$	75	5	20	PANI@Fe_3O_4:MoS_2

3.5. Characterization techniques

The structural properties of the samples were characterized using X-Ray Diffraction (XRD) analysis with the Rigaku MiniFlex. The morphologies were studied with the FEI-Quanta 650 Field Emission equipment using Scanning Electron Microscopy (SEM), while the elemental

analysis was conducted using Energy-Dispersive Spectroscopy (EDS). The thermal behaviors of the samples were characterized using Thermogravimetric Analysis (TG) with the Hitachi STA7300. Vibrating Sample Magnetometry (VSM) using the Quantum Design DynaCool was used to study the magnetic characteristics. Lastly, the electromagnetic parameters and reflection behaviors of the samples were examined using the Agilent E8363B PNA Vector Network Analyzer.

3.5.1. Structural analysis

3.5.1.1. X-ray diffraction method

XRD (X-ray diffraction) characterisation method is an analytical technique used to study and characterise the structural properties of materials with crystalline structures. This method is used to determine the internal atomic arrangement of the material, crystal structure, period lengths and composition of the crystal. In 1912, Max von Laue's discovery of X-ray diffraction through a crystal of copper sulphate demonstrated the periodic atomic arrangement of crystals. This research, which showed the power of X-ray diffraction in determining internal atomic arrangement, resulted in von Laue receiving the 1914 Nobel Prize in Physics. William Lawrence Bragg and his father, Sir William Henry Bragg, were motivated by von Laue's research and formulated "Bragg's Law". This mathematical concept explains X-ray diffraction and is utilised to establish atom positioning. It is considered an integral equation in X-ray diffraction experiments and was crucial to the Bragg duo winning the 1915 Nobel Prize in Physics. Bragg's Law is still a prominent feature in X-ray diffraction analysis and crystal structure studies. Bragg's Law is as follows.

$$n\lambda = 2\sin\theta \tag{3.1}$$

where, n denotes the order of diffraction (first order, second order, third order, etc.). λ represents the wavelength (in nanometres) of X-ray employed. d denotes the period length (interplanar distance) of the crystal structure (in angstroms). θ represents the scattering angle.

The Bragg diffraction hypothesis describes a phenomenon in which atomic planes in a crystal lattice function as virtual "mirrors," resulting in the reflection of X-rays. Horizontal lines that contain the scattering centers represent these “mirrors” or, in other words, the atoms are designated by the green circles depicted in Figure 3.5a-b. The periodic arrangement of the

crystal establishes a constant distance "d" between these planes. The two X-ray beams and light with wavelength λ reach virtual planes at an incidence angle of θ. They combine to form a wave front (blue line on the left in Figure 3.5a). For cooperation, the X-ray beams must maintain coherence after reflection (blue line on the right in Figure 3.5a). Coherence occurs when the difference in the paths traveled by the OF and OH wave fronts (wave fronts before and after reflection) is one wavelength. When the angle of incidence of X-rays does not comply with Bragg's Law, the resultant rays are no longer in phase (green line on the right in Fig. 3.5b) and interfere destructively, causing the absence of the detected reflected intensity.

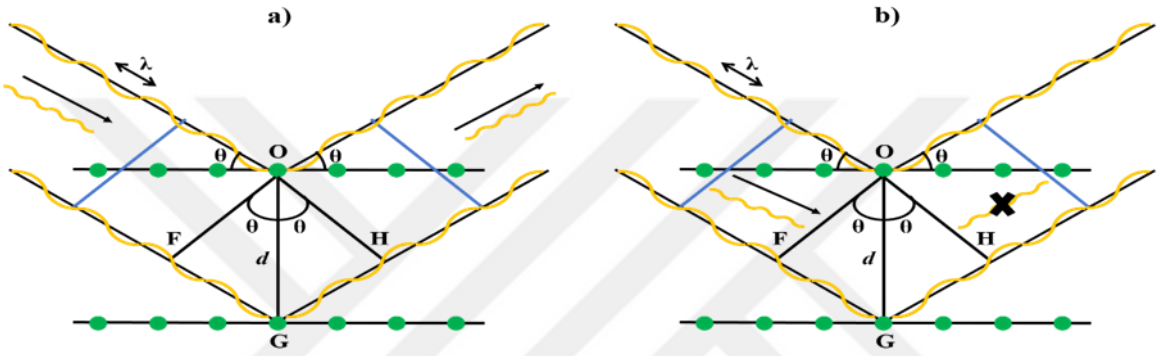

Figure 3.5. X-ray diffraction in crystal planes and the principle of Bragg's law.

Within the confines of this research project, X-ray diffractometry readings were conducted at Adana Alparslan Türkeş Science and Technology University. Cu-Kα (1.5405 Å) was the source of X-ray used, and the analyses were executed via Rigaku MiniFlex 600 X-ray diffractometer and analyzed with X'Pert HighScore Plus software (see Figure 3.6). At room temperature, the tests were undertaken in the angle margin spanning from 5° to 90°, moving at 3° per minute.

Figure 3.6. X-ray diffraction system of Rigaku MiniFlex 600.

3.5.2. Morphological Analysis

3.5.2.1. Scanning electron microscopy and energy-dispersive x-ray spectrum methods

SEM is a surface analysis tool that uses a beam of high-energy electrons to interact with the sample surface and examine the resulting interaction. Figure 3.7 shows a schematic representation of the working principle of the SEM. The sample surface interacts with the electron beam, resulting in the production of characteristic X-rays, scattering of secondary electrons, propagation of backscattered electrons, and loss of energy by electrons. The signals resulting from these interactions are detected by the SEM and processed by computers to produce high resolution images. These images are utilized to analyze the surface topography, composition, and properties of the sample.

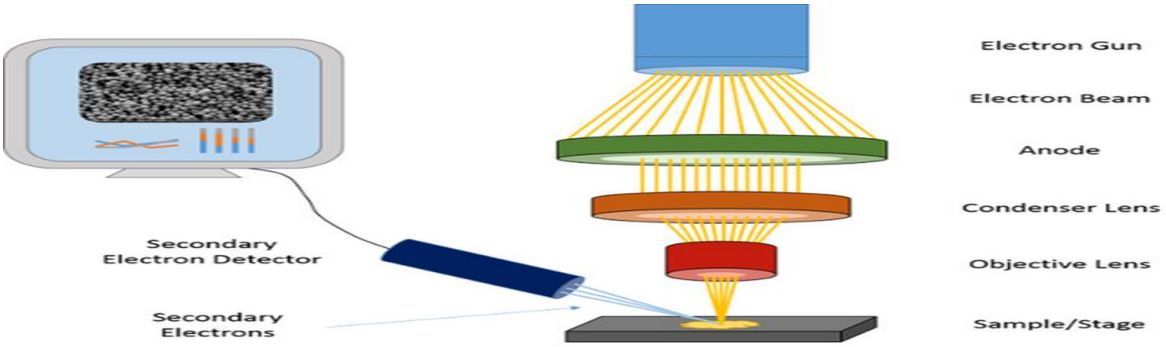

Figure 3.7. Schematic representation of the working principle of SEM.

EDS is an analytical technique utilized in SEM and is grounded on the measurement of characteristic X-rays in determining the chemical makeup of samples. The EDS analysis technique is based on the interaction between the SEM-generated electron beam and the sample surface, which then stimulates the electrons in the inner atoms, generating characteristic X-rays. EDS instrument separates and detects the energy levels of X-rays, then determines the presence and intensity of chemical elements within the sample by generating an energy-dispersive spectrum. These spectra enable identification and analysis of the sample's composition, and provide a valuable tool for determining the chemical elements present. SEM pictures and EDS analyses of the nanoparticles created in this study were collected at the Central Research Laboratory of Çukurova University using an FEI Quanta FEG 650 model scanning electron microscope with EDS integration (see Figure 3.8).

Figure 3.8. FEI Quanta FEG 650 model scanning electron microscope with EDS integration.

3.5.3. Thermal analysis

3.5.3.1 Thermogravimetric analysis method

TGA is a commonly used analytical technique that enables researchers to examine the mass variation of materials against temperature. TGA provides valuable insights into the thermal stability, degradation temperatures, evaporation rates, and components of materials. The process entails preparing the sample, measuring its initial weight and then gradually heating it under controlled conditions while observing mass loss. The TGA instrument records the relationship between temperature and mass loss, providing data that can be analysed to determine various properties of the material, such as its thermal stability, decomposition temperatures and evaporation rates. This information is invaluable for comprehending the material's properties, ensuring quality control, or contributing to the development of novel materials. TGA is of great importance in numerous scientific research disciplines, such as materials science, chemistry, polymer science, and drug development. This method is considered a valuable tool for conducting scientific investigations. The thermal analysis of the samples was conducted using the Hitachi STA 7300 instrument (see Figure 3.9). The analysis was performed at a heating rate of 10°C/min, covering temperatures ranging from room temperature to 550°C.

Figure 3.9. Hitachi STA 7300 instrument used in thermal analysis.

3.5.4. Magnetic analysis

3.5.4.1. Vibrating sample magnetometry method

VSM is a widely used laboratory instrument for studying magnetic properties. It is commonly used in solid state physics and materials science for the characterization of magnetic materials. The main purpose of the VSM is to analyze the magnetic behavior of samples and

determine their magnetic moments and response to external magnetic fields. The instrument operates by subjecting a prepared magnetic sample to a vibrating motion, which helps in measuring the magnetic moment. Then, an external magnetic field is applied, and the sample is kept under its influence to study its magnetic behavior. The vibrating sample enables the measurement of the magnetic moment, which is used to characterize the behavior and magnetic transition points of the sample. The VSM is a valuable tool for the detailed analysis of magnetic properties, which is crucial for the design and application of magnetic materials. Magnetic hysteresis *(M(H))* measurements of the synthesised samples were carried out with Quantum Design brand DynaCool model PPMS system (see Figure 3.10) at Çukurova University Central Laboratory by sweeping the magnetic field between ∓2T at room temperature.

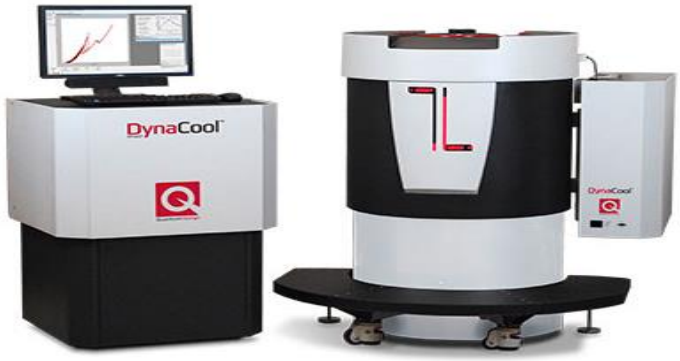

Figure 3.10. Quantum Design brand DynaCool model PPMS system.

3.5.5. Electromagnetic analysis

3.5.5.1. Vector network analyzer method

VNA is a measuring device that analyses the transmission and reflection characteristics of electromagnetic waves at high frequencies, typically in radio frequency and microwave frequencies. This instrument determines how effectively electromagnetic waves are transmitted and reflected from objects or materials. To measure return loss, the VNA is prepared and the correct connections are established. The frequency range and measurement parameters of the VNA are designated, followed by directing the electromagnetic waves, produced by the VNA, to the surface of the object or material being studied, and then measuring the resulting wave reflection. The frequency range and measurement parameters of

the VNA are designated, followed by directing the electromagnetic waves, produced by the VNA, to the surface of the object or material being studied, and then measuring the resulting wave reflection. The reflection data obtained is used to analyse and determine the reflection loss, which is expressed in dB. Electromagnetic parameters and reflection behaviour of the samples were investigated between 2-18 GHz using an Agilent E8363B PNA (see Figure 3.11) at Turkish Aerospace.

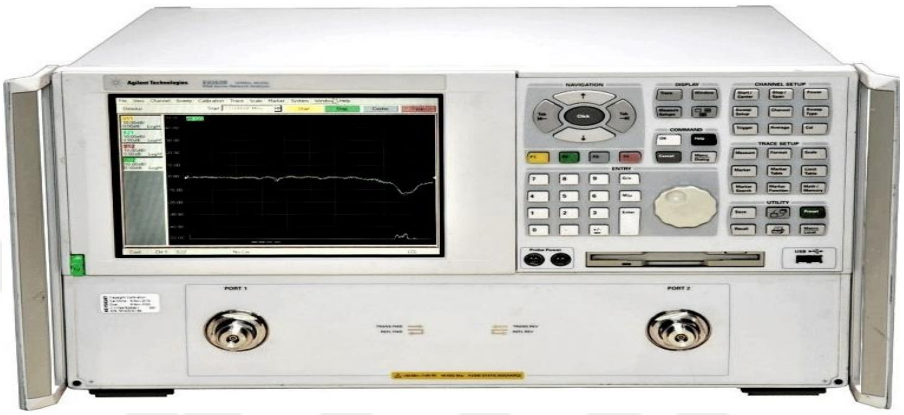

Figure 3.11. Agilent E8363B PNA brand network analyzer.

4. ANALYSIS AND DISCUSSION

In this thesis, Fe_3O_4 nanoparticles were decorated on MoS_2 at different ratios (5 wt%, 10 wt%, 15 wt%, 20 wt%). Then, PANI was coated on Fe_3O_4 decorated MoS_2 samples at different ratios (25 wt%, 50 wt%, 75 wt%). Thus, PANI@Fe_3O_4:MoS_2 hybrid structure was obtained as described in Chapter 3. The obtained hybrid structures were dispersed in epoxy resin and radar absorbing composite structures were obtained as shown in Table 3.1. The structural, morphological, thermal, magnetic and electromagnetic properties of the synthesised hybrid structures are discussed in Sections 4.1, 4.2, 4.3 and 4.4 respectively.

4.1. Structural Analysis

4.1.1. X-ray diffraction

The synthesised hybrid structures were characterised by X-ray diffraction (XRD) measurement method for structural analysis. XRD measurements were performed by scanning diffraction angles between 5° and 90°. The peaks of the hybrid structures were analysed using X' Pert HighScore Plus software.

Figure 4.1a-d shows the XRD patterns of Fe_3O_4 MoS_2 PANI, F_5M_{95}, $F_{10}M_{90}$, $F_{15}M_{85}$, $F_{20}M_{80}$, $P_{25}M_{75}$, $P_{50}M_{50}$, $P_{75}M_{25}$, $P_{25}F_{75}$, $P_{50}F_{50}$ and $P_{75}F_{25}$, respectively. The diffraction peaks of the obtained MoS_2 sample were observed to have 2θ values of 13.62°, 28.42°, 32.40°, 35.56°, 43.63° and 57.53°, respectively. These peaks were identified by indices (002), (004), (100), (102), (006) and (110). In addition, the peaks of the MoS_2 sample are indicated by the symbol ♥, indicating the distinct characteristic peaks of the hexagonal crystal structure of MoS_2 [44-46]**.** The diffraction peaks of the Fe_3O_4 sample were observed to have 2θ values of 18.37°, 21.62°, 30.23°, 35.59°, 42.97°, 53.48°, 56.93°, 62.67°, 71.27° and 74.04°, respectively. These peaks were identified by indices (111), (200), (002), (311), (400), (422), (511), (440), (620) and (553) [47-49]. These peaks, marked with the symbol ♦, represent the characteristic peaks of the cubic crystal structure of Fe_3O_4. The XRD patterns of the conducting polymer PANI show characteristic peaks indicated by the symbol ♠. These peaks have 2θ values of 9.34°, 15.12°, 20.36°, 25.27°, 27.18° and 30.32° and these peaks are indexed to (001), (011), (020), (200), (121) and (022) planes, respectively [50-52]. Figure 4.1b shows the XRD patterns of F_5M_{95}, $F_{10}M_{90}$, $F_{15}M_{85}$ and $F_{20}M_{80}$ samples. The hybrid structures exhibit peaks represented by the symbols shown above. MoS_2 decorated with Fe_3O_4 samples display peaks that

correspond to the MoS_2 and Fe_3O_4 planes. It is important to note that the primary peak of the Fe_3O_4 sample, observed at 35.59°, coincides with the MoS_2 peak at 35.56°. Moreover, it is clearly seen that as the amount of Fe_3O_4 increases in the . MoS_2 decorated with Fe_3O_4 samples, the intensity of the peak at 62.67° belonging to Fe_3O_4 increases and is marked with the symbol ♦. XRD patterns of PANI coated MoS_2 samples are given in Figure 4.1.c. In the PANI coated MoS_2 samples, it is seen that the intensity of the peaks at 18.37°, 21.62° and 30.23° of PANI increases with the increase in the amount of PANI and is marked with the symbol ♠. Figure 4.1.d shows the XRD patterns of PANI coated Fe_3O_4 samples. In the PANI coated Fe_3O_4 samples, it is seen that the intensity of the peaks at 9.34°, 15.12°, 20.36°, 25.27° and 27.18° of PANI increases with the increase in the amount of PANI and is marked with the symbol ♠. Peaks appearing as impurities are marked with the symbol ♣.

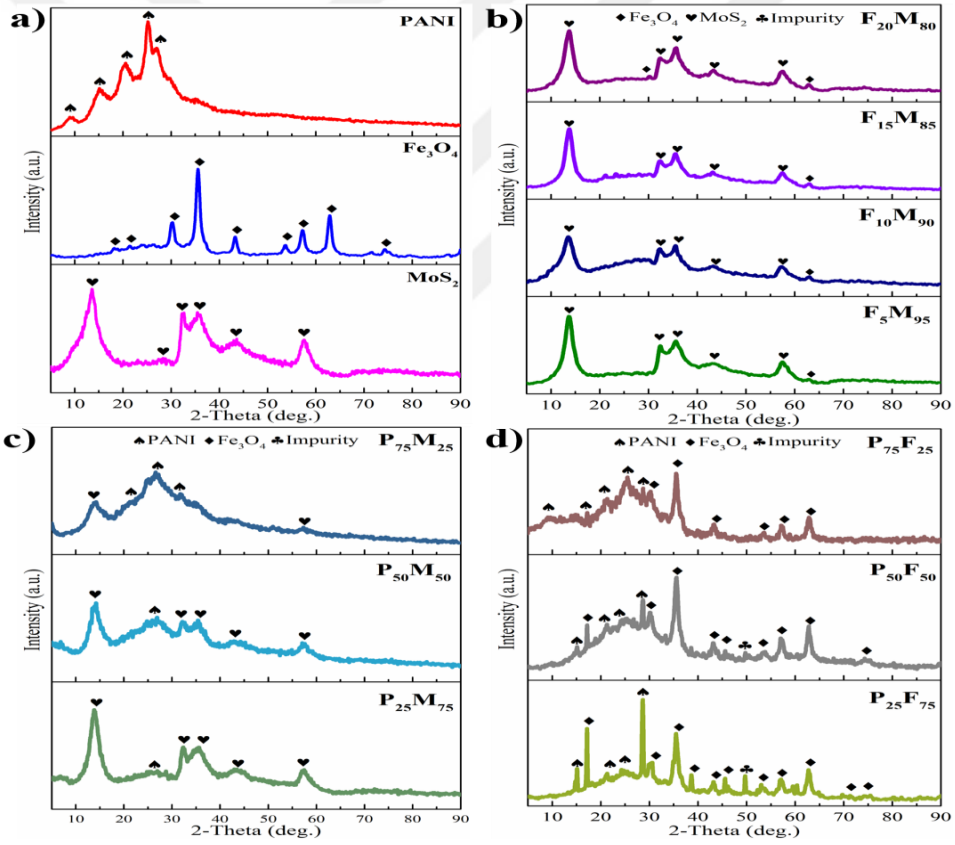

Figure 4.1. XRD patterns of a) Fe_3O_4, MoS_2 and PANI b) F_5M_{95}, $F_{10}M_{90}$, $F_{15}M_{85}$, $F_{20}M_{80}$ c) $P_{25}M_{75}$, $P_{50}M_{50}$, $P_{75}M_{25}$ d) $P_{25}F_{75}$, $P_{50}F_{50}$, $P_{75}F_{25}$ samples.

Figure 4.2a-d shows the XRD patterns of $P_{25}F_{3.75}M_{71.25}$, $P_{50}F_{2.5}M_{47.25}$, $P_{75}F_{1.25}M_{23.75}$, $P_{25}F_{7.5}M_{67.5}$, $P_{50}F_5M_{45}$, $P_{75}F_{2.5}M_{22.5}$, $P_{25}F_{11.25}M_{63.75}$, $P_{50}F_{7.5}M_{42.5}$, $P_{75}F_{3.75}M_{21.25}$, $P_{25}F_{15}M_{60}$,

$P_{50}F_{10}M_{40}$ and $P_{75}F_5M_{20}$, respectively. Figure 4.2 a-d clearly shows that F_5M_{95}, $F_{10}M_{90}$, $F_{15}M_{85}$ and $F_{20}M_{80}$ samples were coated with PANI at different ratios and the intensity of MoS_2 and Fe_3O_4 peaks decreased in all samples with increasing PANI amount. The peaks belonging to all samples are marked and shown in Figure 4.2a-d. ♣ symbolizes the impurity in the samples. Impurities were formed as a result of the increased use of HCl acid during the synthesis with the refinement of the amount of PANI.

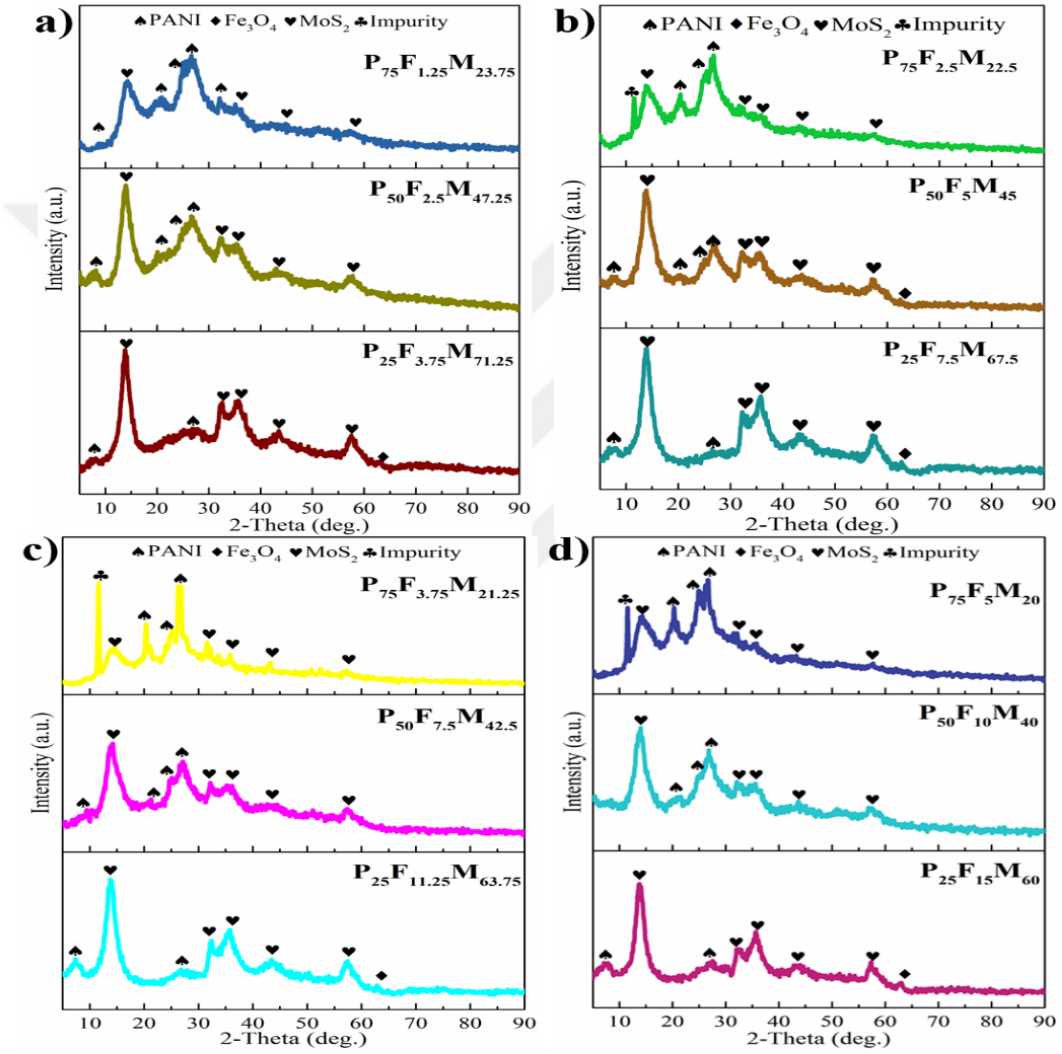

Figure 4.2. XRD patterns of a) $P_{25}F_{3.75}M_{71.25}$, $P_{50}F_{2.5}M_{47.25}$, $P_{75}F_{1.25}M_{23.75}$ b) $P_{25}F_{7.5}M_{67.5}$, $P_{50}F_5M_{45}$, $P_{75}F_{2.5}M_{22.5}$ c) $P_{25}F_{11.25}M_{63.75}$, $P_{50}F_{7.5}M_{42.5}$, $P_{75}F_{3.75}M_{21.25}$ d) $P_{25}F_{15}M_{60}$, $P_{50}F_{10}M_{40}$, $P_{75}F_5M_{20}$ samples.

4.2. Morphological Analysis

4.2.1. Scanning electron microscopy and energy-dispersive x-ray spectrum

The morphological and elemental analysis of the synthesized samples were investigated by scanning electron microscopy (SEM) images and energy dispersive x-ray spectrums (EDS). To determine the particle size distribution, 100 particles were randomly selected from the SEM images of all samples in imgeJ software program. To improve surface conductivity, the samples were coated with gold (Au) prior to EDS measurements. The gold element was subsequently excluded from the elemental analysis.

In Figure 4.3, a set of SEM images, EDS graph and elemental analysis results are presented for Fe_3O_4, MoS_2, and PANI. The images in Figure 4.3a-b show that Fe_3O_4 nanoparticles were accurately synthesized with a relatively uniform particle size distribution of 23.31 nm. EDS graph and elemental analysis of Fe_3O_4 nanoparticles in Figure 4.3c reveals that they consist of 75.25 wt% Fe and 24.75 wt% O. This confirms the successful synthesis of Fe_3O_4 nanoparticles in terms of their elemental content. Similarly, Figure 4.3d-e demonstrate the successful formation of MoS_2 nanosheets, exhibiting a uniform particle size distribution with an average size of 201 nm. EDS graph and elemental analysis in Figure 4.3(f) indicates that MoS_2 nanosheets consist of 8.25 wt% O, 46.06 wt% Mo, and 32.42 wt% S, resulting in an Mo/S atomic weight ratio of 1.23, signifying successful synthesis. Lastly, Figure 4.3g-h confirm the correct synthesis of the conducting polymer PANI, while Figure 4.3i shows its EDS graph and elemental analysis to be 50.81 wt% C, 19.99 wt% N, 13.87 wt% O, 5.90 wt% S, and 9.42 wt% Cl, indicating successful synthesis.

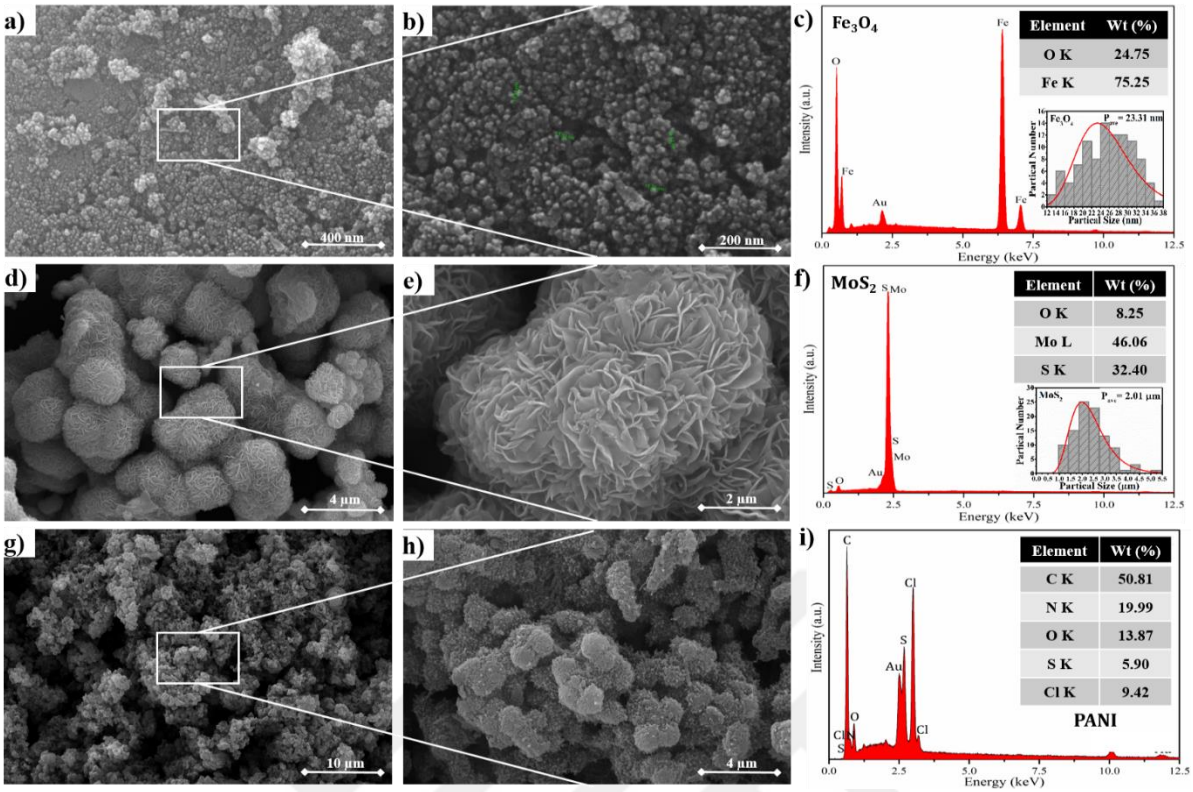

Figure 4.3. (a-c) SEM figures, EDS measurement and particle size distrubition of Fe_3O_4, (d-f) SEM figures, EDS measurement and particle size distrubition of MoS_2, (g-i) SEM figures and EDS measurement PANI sample.

SEM images and EDS analysis results of F_5M_{95} sample are given in Figure 4.4a-c. Figure 4.4a-b shows that Fe_3O_4 nanoparticles are placed on the layers of MoS_2, but the layers are not completely filled. Figure 4.4c shows the EDS graph and elemental analysis results. The elemental analysis results are almost completely consistent with the doping ratio we determined. Thus, it was determined that the F_5M_{95} sample was successfully synthesised at the determined rate. Figure 4.4d-f shows the SEM images and EDS analysis results of the $F_{10}M_{90}$ sample. In Figure 4.4d-e, Fe_3O_4 nanoparticles started to become more prominent on the layers of MoS_2. The space between the layers has started to fill partially. Figure 4.4f shows the EDS graph and elemental analysis results. The elemental analysis results are almost completely consistent with the doping determined ratio. Thus, it was determined that the $F_{10}M_{90}$ sample was successfully synthesised at the determined ratio. Figure 4.4g-i shows the SEM images and EDS analysis results of sample $F_{15}M_{85}$. In Figure 4.4g-h, MoS_2 is partially filled between some layers, but some parts are still empty and Fe_3O_4 is clearly visible. Figure 4.4i shows the EDS graph and elemental analysis results. The elemental analysis results are

almost completely consistent with the doping ratio we have determined. Thus, it was determined that the $F_{15}M_{85}$ sample was successfully synthesised at the determined ratio. Figure 4.4j-l shows the SEM images and EDS analysis results of the $F_{20}M_{80}$ sample. In Figure 4.4j-k, it is seen that the interlayer space between the layers of MoS_2 is almost completely filled and Fe_3O_4 is integrated with the layers. Figure 4.4l shows the EDS graph and elemental analysis results. The elemental analysis results are almost completely consistent with the doping ratio we determined. Thus, it was determined that the $F_{20}M_{80}$ sample was successfully synthesised at the determined ratio.

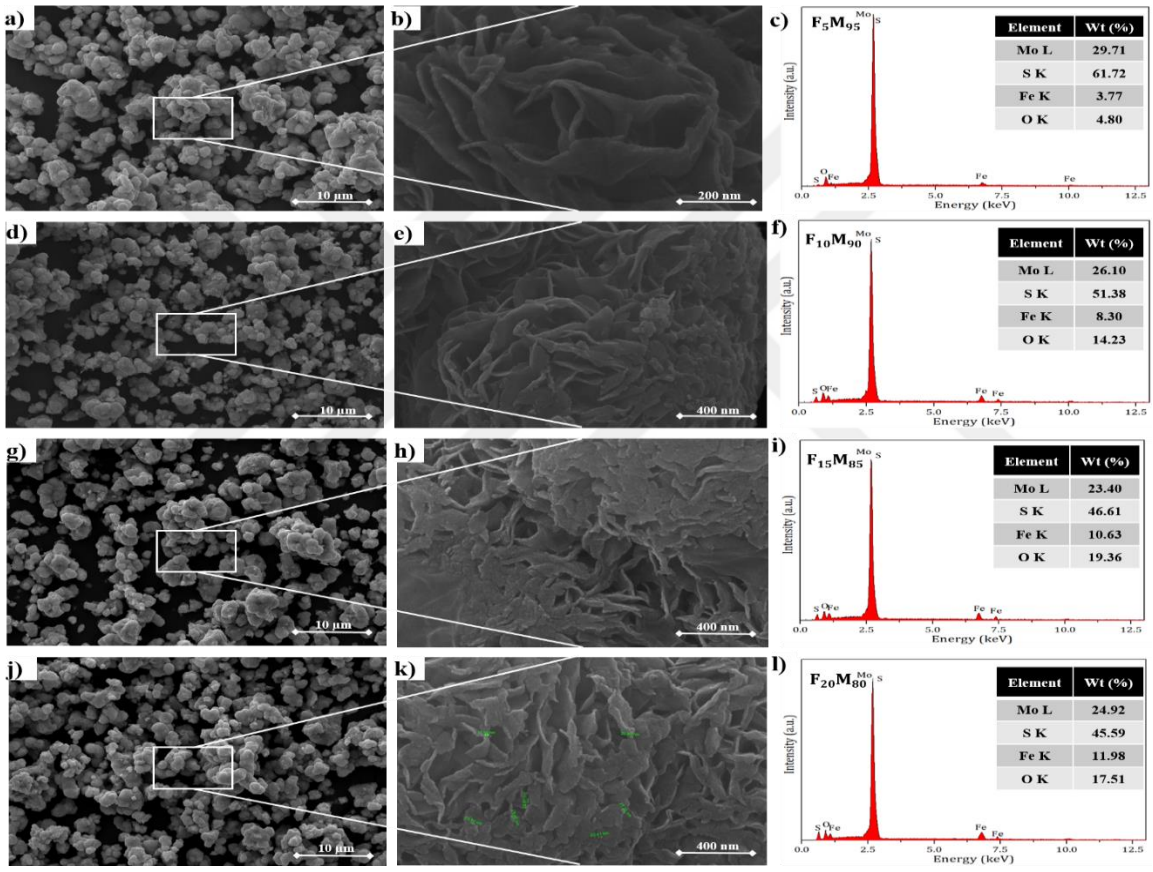

Figure 4.4. (a-c) SEM figures and EDS measurement of F_5M_{95} sample, (d-f) SEM figures and EDS measurement $F_{10}M_{90}$ sample, (g-i) SEM figures and EDS measurement $F_{15}M_{85}$ sample, (j-l) SEM figures and EDS measurement $F_{20}M_{80}$ sample.

Figure 4.5 shows the SEM images and EDS analysis results of $P_{25}F_{75}$, $P_{50}F_{50}$, $P_{75}F_{25}$, $P_{25}M_{75}$ and $P_{50}M_{50}$ samples. The SEM images of $P_{25}F_{75}$, $P_{50}F_{50}$, and $P_{75}F_{25}$ samples exhibit Fe_3O_4 nanoparticles that are fully coated with PANI as the amount of PANI increases. Moreover, the EDS graphs and elemental analysis results of the samples show that the samples were

synthesised at the targeted rate. In the SEM images of samples $P_{25}M_{75}$ and $P_{50}M_{50}$, the MoS_2 nanosheets were observed to be filling between each other and being completely coated with PANI in response to the increased amount of the latter. Furthermore, the EDS graphs and elemental analysis results of the samples show that the samples were synthesised at the targeted ratio.

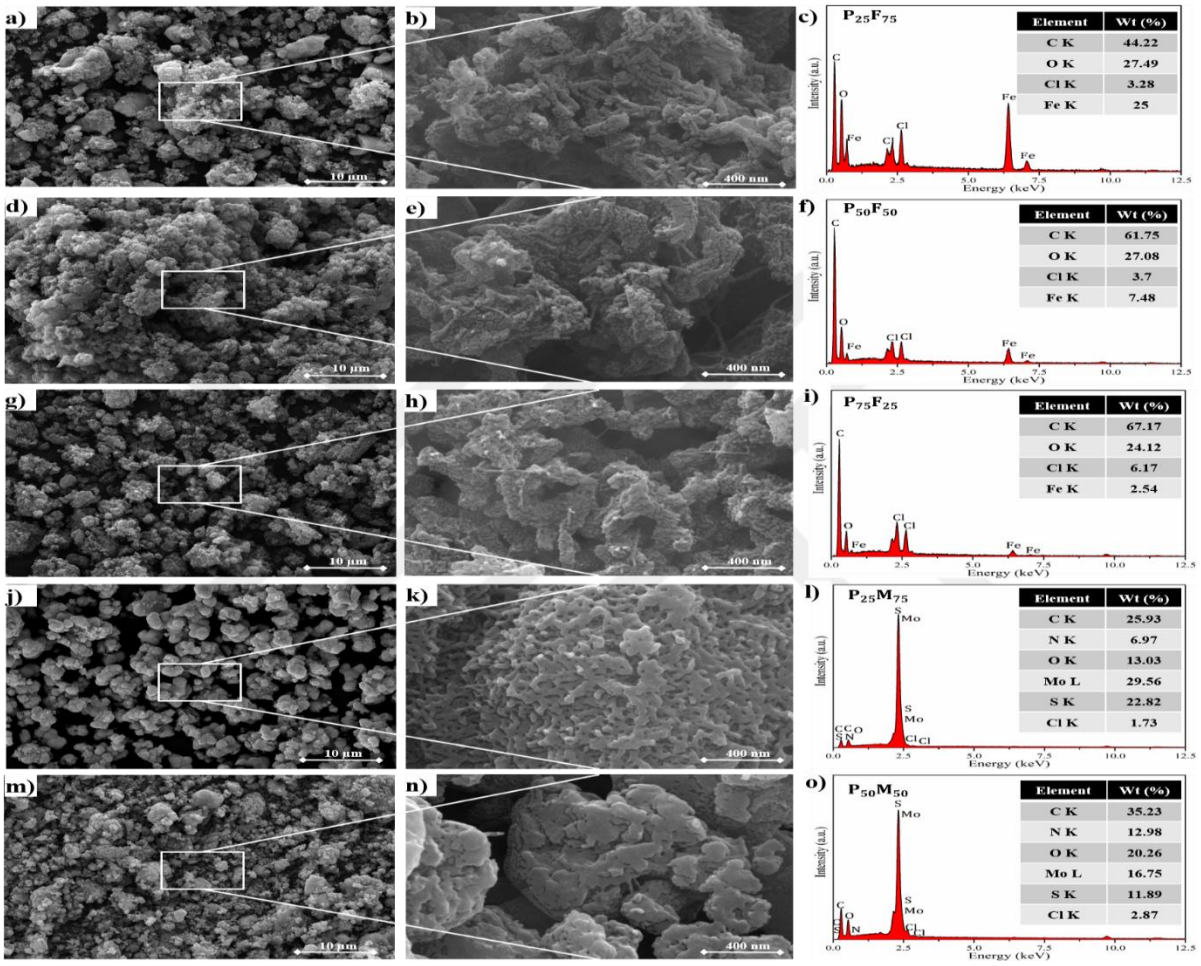

Figure 4.5. (a-c) SEM figures and EDS measurement of $P_{25}F_{75}$ sample, (d-f) SEM figures and EDS measurement $P_{50}F_{50}$ sample, (g-i) SEM figures and EDS measurement $P_{75}F_{25}$ sample, (j-l) SEM figures and EDS measurement $P_{25}M_{75}$ sample, (m-o) SEM figures and EDS measurement $P_{50}M_{50}$ sample.

Figure 4.5 shows the SEM images and EDS analysis results of samples $P_{75}F_{1.25}M_{23.75}$, $P_{75}F_{2.5}M_{22.5}$, $P_{75}F_{3.75}M_{21.25}$, $P_{75}F_5M_{20}$. The SEM images of the samples show that the MoS_2 decorated with Fe_3O_4 at different ratios are completely coated with PANI. Furthermore, the EDS graphs and elemental analysis results of the samples show that the samples were

synthesised in close to the target ratio. SEM and EDS analysis of all PANI-coated samples were not performed because the images and elemental analysis results are almost identical. This can be attributed to the low density of PANI, which results in a high volume of PANI.

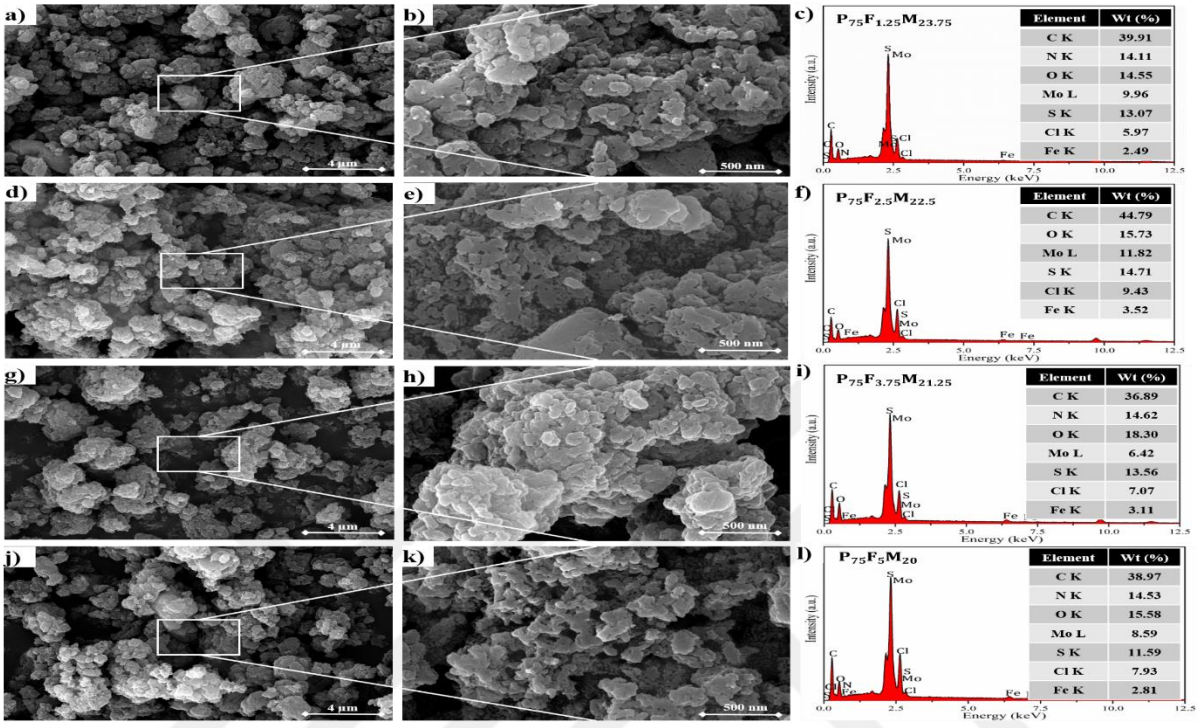

Figure 4.6. (a-c) SEM figures and EDS measurement of $P_{75}F_{1.25}M_{23.75}$ sample, (d-f) SEM figures and EDS measurement $P_{75}F_{2.5}M_{22.5}$ sample, (g-i) SEM figures and EDS measurement $P_{75}F_{3.75}M_{21.25}$ sample, (j-l) SEM figures and EDS measurement $P_{75}F_5M_{20}$ sample.

4.3. Thermal Analysis

4.3.1. Thermogravimetric analysis

The ability to withstand high temperatures is crucial for electromagnetic wave absorbing materials to perform well. To assess the durability of these materials, we conducted thermal gravimetric analysis at a heating rate of 10 °C/min, over a temperature range of up to 500 °C. Figure 4.7a shows the thermogravimetric analysis (TGA) curves of Fe_3O_4, MoS_2, and PANI. The corresponding weight losses were quantified as 8.64%, 26.89%, and 44.83%, respectively. The decrease in mass for Fe_3O_4 nanoparticles can be attributed to the evaporation of physically adsorbed water molecules, occurring within a temperature range of approximately 40°C to 100°C [53, 54]. Furthermore, the loss in mass is also attributed to

molecular alterations resulting from the thermal decomposition of organic compounds associated with Fe_3O_4 nanoparticles between approximately 100°C and 500°C [53, 54]. The loss of mass of MoS_2 nanosheets, the physical loss of moisture between about 40°C and 100°C, is associated with the process of conversion of MoS_2 to MoO_3, while the oxidation of MoS_2 occurs between about 300°C and 500°C [55-57]. The weight loss of PANI begins with physical moisture loss, which is observed in the range between about 40 °C and 100 °C. Subsequently, thermo-oxidative decomposition of PANI happens within the temperature range of about 100 °C to 300 °C, leading to the volatilization of constituents such as N-phenylaniline, methane, acetylene, carbazole, etc [58, 59]. Finally, within the temperature range of about 300 °C to 500 °C, the breakdown and decomposition of the major chains of PANI occur [58, 59]. Figure 4.7b shows the TGA curves of F_5M_{95}, $F_{10}M_{90}$, $F_{15}M_{85}$ and $F_{20}M_{80}$ samples. The weight loss decreased with the increase in the amount of Fe_3O_4 in the samples. The weight losses of F_5M_{95}, $F_{10}M_{90}$, $F_{15}M_{85}$ and $F_{20}M_{80}$ samples were determined as 20.32%, 15.16%, 12.44% and 10.53%, respectively. Figure 4.7c shows the TGA curves of $P_{25}M_{75}$, $P_{50}M_{50}$ and $P_{75}M_{25}$ samples. The weight loss increased with the increase in the amount of PANI in the samples. The weight losses of $P_{25}M_{75}$, $P_{50}M_{50}$ and $P_{75}M_{25}$ samples were determined as 15.50%, 25.35% and 31.90%, respectively. Figure 4.7d shows the TGA curves of $P_{25}F_{75}$, $P_{50}F_{50}$ and $P_{75}F_{25}$ samples. The weight loss increased with the increase in the amount of PANI in the samples. The weight losses of $P_{25}F_{75}$, $P_{50}F_{50}$ and $P_{75}F_{25}$ samples were determined as 28.33%, 28.57% and 40.63%, respectively. Figure 4.7e-h, TGA curves of $P_{25}F_{3.75}M_{71.25}$, $P_{50}F_{2.5}M_{47.5}$, $P_{75}F_{1.25}M_{23.75}$, $P_{25}F_{7.5}M_{67.5}$, $P_{50}F_5M_{45}$, $P_{75}F_{2.5}M_{22.50}$, $P_{25}F_{11.25}M_{63.75}$, $P_{50}F_{7.5}M_{42.5}$, $P_{75}F_{3.75}M_{21.25}$, $P_{25}F_{15}M_{60}$, $P_{50}F_{10}M_{40}$ and $P_{75}F_5M_{25}$ samples. It was found that the weight loss of the samples decreased with the increase in the amount of PANI and the increase decreased the amount of MoS_2. The weight losses of the samples were 14.40%, 24.50%, 28.73%, 12.96%, 29.26%, 37.85%, 14.04%, 28.54%, 40.18%, 19.95%, 28.73% and 39.11%, respectively. When the weight losses of all samples are examined, it is clearly understood that increasing the amount of PANI increases the weight loss, while increasing the amount of Fe_3O_4 and MoS_2 decreases the weight loss.

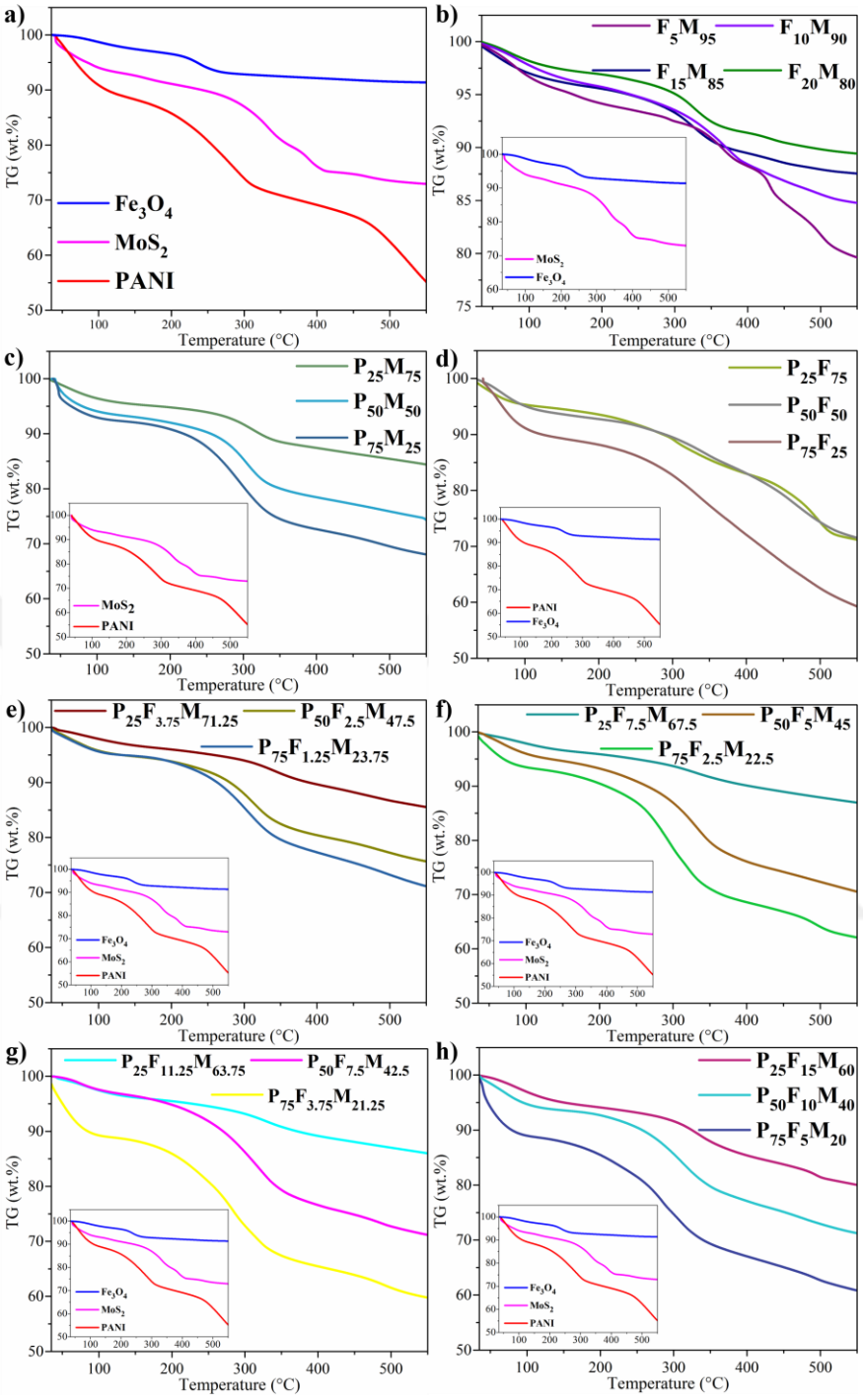

Figure 4.7. TG curves of a) Fe_3O_4, MoS_2, PANI, b) F_5M_{95}, $F_{10}M_{90}$, $F_{15}M_{85}$, $F_{20}M_{80}$ c) $P_{25}M_{75}$, $P_{50}M_{50}$, $P_{75}M_{25}$ d) $P_{25}F_{75}$, $P_{50}F_{50}$, $P_{75}F_{25}$ e) $P_{25}F_{3.75}M_{71.25}$, $P_{50}F_{2.5}M_{47.5}$, $P_{75}F_{1.25}M_{23.75}$ f) $P_{25}F_{7.5}M_{67.5}$, $P_{50}F_5M_{45}$, $P_{75}F_{2.5}M_{22.50}$ g) $P_{25}F_{11.25}M_{63.75}$, $P_{50}F_{7.5}M_{42.5}$, $P_{75}F_{3.75}M_{21.25}$ h) $P_{25}F_{15}M_{60}$, $P_{50}F_{10}M_{40}$ and $P_{75}F_5M_{25}$ samples.

4.4. Magnetic Analysis

4.4.1. Vibrating sample magnetometry

Magnetic hysteresis measurements *(M(H))* were conducted on the synthesized hybrid structures by applying a magnetic field between ±2T at room temperature. In addition, magnetic hysteresis *(M(H))* measurements were not performed since PANI, MoS_2 and hybrid structures consisting of only these two structures do not have magnetic properties. Figure 4.8 shows the *M(H)* curves of Fe_3O_4, F_5M_{95}, $F_{10}M_{90}$, $F_{15}M_{85}$, $F_{20}M_{80}$, $P_{25}F_{3.75}M_{71.25}$, $P_{50}F_{2.5}M_{47.5}$, $P_{75}F_{1.25}M_{23.75}$, $P_{25}F_{3.75}M_{71.25}$, $P_{50}F_{2.5}M_{47.5}$, $P_{75}F_{1.25}M_{23.75}$, $P_{25}F_{7.5}M_{67.5}$, $P_{50}F_5M_{45}$, $P_{75}F_{2.5}M_{22.50}$, $P_{25}F_{11.25}M_{63.75}$, $P_{50}F_{7.5}M_{42.5}$, $P_{75}F_{3.75}M_{21.}25$, $P_{25}F_{15}M_{60}$, $P_{50}F_{10}M_{40}$ and $P_{75}F_5M_{25}$ samples. In hybrid structures, the only material showing magnetic properties is Fe_3O_4 nanoparticles. A typical magnetic hysteresis wave was observed in all of our samples. This is because Fe_3O_4 nanoparticles lack a coercive field value due to their size and inverse spinel structure property. Figure 4.8a shows the magnetic hysterisis curves of Fe_3O_4, F_5M_{95}, $F_{10}M_{90}$, $F_{15}M_{85}$ and $F_{20}M_{80}$ samples. Magnetic saturation values were determined as 50.22 emu/g, 4.34 emu/g, 7.33 emu/g, 9.26 emu/g and 10.83 emu/g, respectively. It was determined that the magnetic saturation values increased as the amount of Fe_3O_4 decorated on MoS_2 increased. Figure 4.8b shows the magnetic hysterisis curves of $P_{25}F_{75}$, $P_{50}F_{50}$ and $P_{75}F_{25}$ samples. Magnetic saturation values were determined as 29.20 emu/g, 20.09 emu/g and 8.37 emu/g, respectively. Since PANI does not have magnetic properties, it was determined that the magnetic saturation value decreased as the amount of PANI increased. Figure 4.8.c-f shows the magnetic hysterisis slopes of $P_{25}F_{3.75}M_{71.25}$, $P_{50}F_{2.5}M_{47.5}$, $P_{75}F_{1.25}M_{23.75}$ $P_{25}F_{7.5}M_{67.5}$, $P_{50}F_5M_{45}$, $P_{75}F_{2.5}M_{22.50}$ $P_{25}F_{11.25}M_{63.75}$, $P_{50}F_{7.5}M_{42.5}$, $P_{75}F_{3.75}M_{21.25}$ $P_{25}F_{15}M_{60}$, $P_{50}F_{10}M_{40}$ and $P_{75}F_5M_{25}$ the samples and the wide range hysterisis slopes of some samples. Magnetic saturation values were determined as 2.17 emu/g, 0.21 emu/g, 0.09 emu/g, 4.97 emu/g, 0.02 emu/g, 0.01 emu/g, 2.59 emu/g, 0.34 emu/g, 0.09 emu/g, 3.43 emu/g, 0.16 emu/g and 0.02 emu/g, respectively. It was found that the magnetic saturation values became very low with the increase in the amount of PANI coated on MoS_2 nanosheets decorated with Fe_3O_4 nanoparticles. The results were consistent with Fe_3O_4 doping ratios.

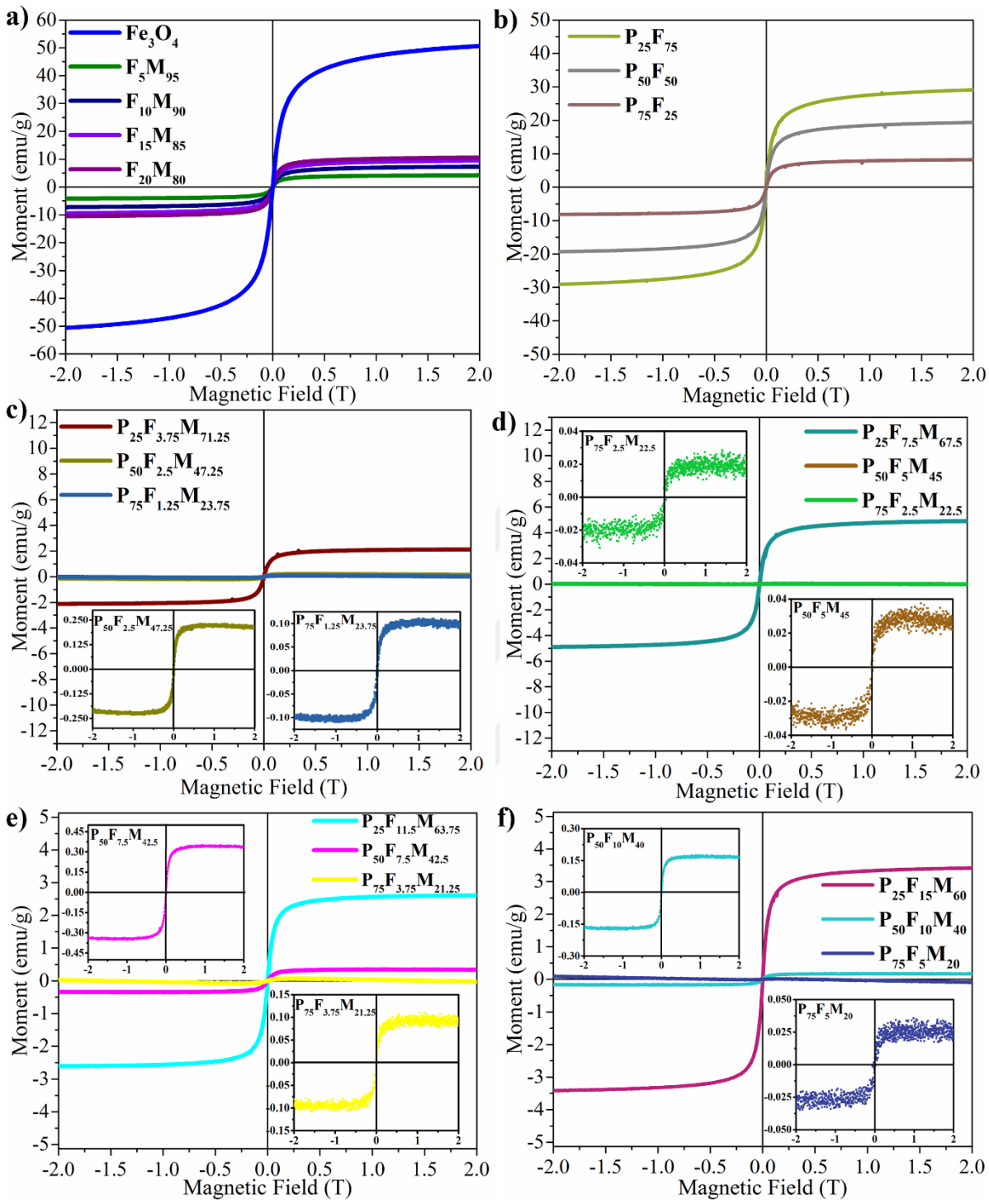

Figure 4.8. Magnetic hysteresis curves of a) Fe_3O_4, F_5M_{95}, $F_{10}M_{90}$, $F_{15}M_{85}$, $F_{20}M_{80}$ b) $P_{25}F_{75}$, $P_{50}F_{50}$, $P_{75}F_{25}$ c) $P_{25}F_{3.75}M_{71.25}$, $P_{50}F_{2.5}M_{47.5}$, $P_{75}F_{1.25}M_{23.75}$ d) $P_{25}F_{7.5}M_{67.5}$, $P_{50}F_5M_{45}$, $P_{75}F_{2.5}M_{22.50}$ e) $P_{25}F_{11.25}M_{63.75}$, $P_{50}F_{7.5}M_{42.5}$, $P_{75}F_{3.75}M_{21.25}$ f) $P_{25}F_{15}M_{60}$, $P_{50}F_{10}M_{40}$ and $P_{75}F_5M_{25}$ samples.

4.5. Electromagnetic Analysis

4.5.1 Electromagnetic parameters

A vector network analyzer was used to examine the performance of hybrid structures in absorbing electromagnetic waves. The reflection loss (RL) value is used to evaluate the absorption performance. Based on transmission line theory, the RL values of a material system are calculated based on the relative complex permittivity *($\varepsilon_r = \varepsilon' - j\varepsilon''$)* and relative complex permeability *($\mu_r = \mu' - j\mu''$)* values. The following equations (4.1) and (4.2) are used to calculate the input impedance and RL [15, 16, 60, 61].

$$Z_{in} = Z_0 \left(\sqrt{\frac{\mu_r}{\varepsilon_r}}\right) \tanh\left[j\left(\frac{2\pi f d}{c}\right)\left(\sqrt{\mu_r \varepsilon_r}\right)\right] \tag{4.1}$$

$$\mathrm{RL} = 20 \log\left(\frac{Z_{in} - Z_0}{Z_{in} + Z_0}\right) \tag{4.2}$$

In this context, Z_{in} represents the input impedance of the absorbent material and Z_0 represents the impedance of air c is the velocity of electromagnetic waves in free space, f is the frequency and d is the thickness of the hybrid material. The real parts of the complex permittivity and permeability (ε' and μ') represent the capacity for storing and converting electromagnetic energy; whereas the imaginary parts (ε″ and μ″) represent energy loss. Logical structure, objective language, and precise vocabulary choices are prioritised. The dielectric ($\tan\delta_\varepsilon$) and magnetic loss tangent ($\tan\delta_\mu$) indicate the angle between the electric and magnetic fields in the electromagnetic wave absorber and those of the electromagnetic wave. While the electrical and magnetic storage parts (ε' and μ') of a material may impact the effective absorption band, the electric and magnetic loss parts (ε″ and μ″) can alter the amount of absorption. To create a high performance electromagnetic wave absorbing material system, it is first required that the internal impedance of a material is equal to or close to the impedance of air (377Ω) over a wide frequency range. If the value of $\left|Z_{in} / Z_0\right|$ is close to 1, this implies a good match and means that the electromagnetic wave can fully penetrate the material. This is an ideal situation for the material to effectively absorb electromagnetic waves. Consequently, an electromagnetic wave absorber structure should incorporate optimal storage, loss and $\left|Z_{in} / Z_0\right|$ values for enhanced electromagnetic wave absorption performance. Figure 4.9a-c shows the relative complex permittivity, relative complex

permeability, dielectric and magnetic loss tangent, reflection loss and impedance matching curves of Fe_3O_4, MoS_2 and PANI. Fe_3O_4, MoS_2, and PANI did not exhibit any electromagnetic wave absorption performance due to their low values of ε″ and μ″, despite having high ε' and μ' values. The low reflection loss and effective absorption band (EAB) can be attributed to the low values of tanδε and tanδμ. The fact that $tan\delta_{\varepsilon}$, which represents the dielectric loss, and $tan\delta_{\mu}$, which represents the magnetic loss, are close to zero supports our interpretations. Additionally, none of the samples demonstrated impedance matching, which is one of the reasons for the low electromagnetic wave absorption performance. Only PANI with a 5 mm thickness demonstrated a reflection loss performance of -20.41 dB at 16.45 GHz, with an EAB of 2.89 GHz.

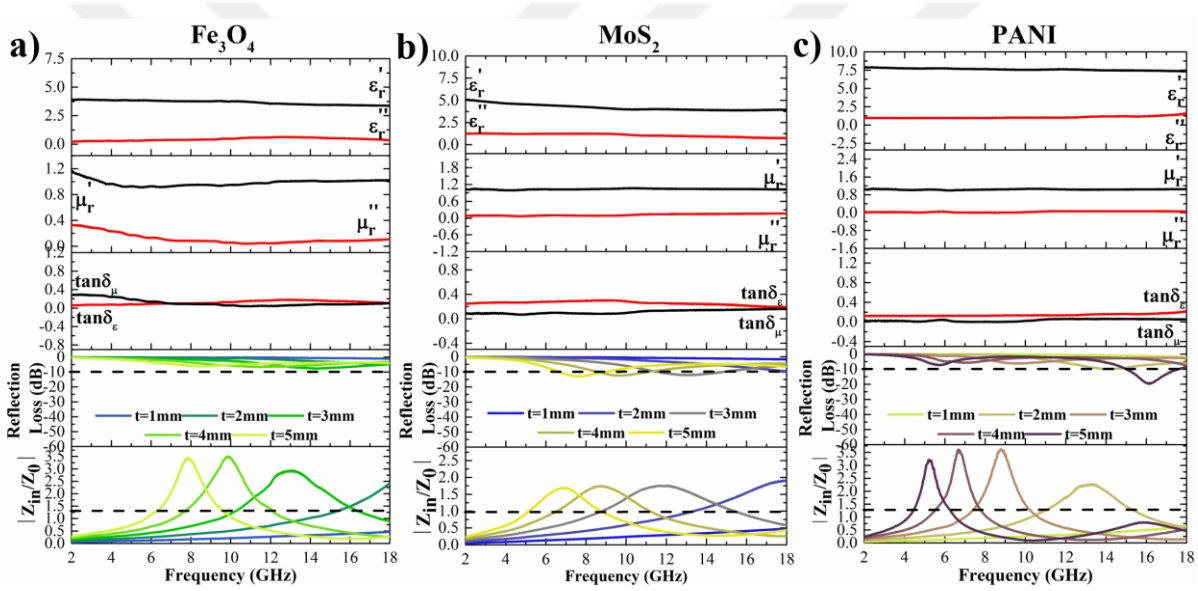

Figure 4.9. Frequency dependence of relative complex permittivity, relative complex permeability, dielectric and magnetic loss tangent, reflection loss and impedance matching ($|Z_{in}/Z_0|$) of a) Fe_3O_4, b) MoS_2 and c) PANI.

Figure 4.10a-d shows the relative complex permittivity, relative complex permeability, dielectric and magnetic loss tangent, reflection loss and impedance matching curves for F_5M_{95}, $F_{10}M_{90}$, $F_{15}M_{85}$ and $F_{20}M_{80}$ samples. The F_5M_{95} sample exhibits high values of μ" and low values of ε", indicating that the loss is due to magnetic interaction. In addition, the high value of tanδμ also supports our interpretation. The values of μ' and ε" suggest that the sample has both dielectric and magnetic storage, which may result in high EAB values. The samples of F_5M_{95} with thicknesses of 3 mm and 4 mm demonstrate good impedance matching, leading

to relatively high reflection loss. The F_5M_{95} sample demonstrated reflection loss values of -31.38 dB at 15.80 GHz and -47.59 dB at 11.36 GHz for thicknesses of 3 mm and 4 mm, respectively, with corresponding EAB values of 4 GHz and 4.27 GHz. The $F_{10}M_{90}$ sample shows high μ" values and low ε" values, indicating that magnetic interactions are the main cause of loss. This interpretation is supported by the significantly high tanδμ value. The elevated values of μ' and ε" in the sample indicate the presence of both dielectric and magnetic storage, potentially leading to higher EAB values. Additionally, the maximum loss values were reached at frequencies where relatively good impedance matching was achieved in thicknesses of 3 mm and 4 mm. The $F_{10}M_{90}$ sample exhibited reflection loss values of -55.54 dB at 15.99 GHz and -52.69 dB at 11.89 GHz for thicknesses of 3 mm and 4 mm, with corresponding EAB values of 4.0 GHz and 4.99 GHz, respectively. The $F_{15}M_{85}$ sample exhibits high μ" values and low ε" values, indicating that the loss is due to magnetic interaction. Furthermore, the high value of tanδμ supports this interpretation. The values of μ' and ε" indicate that the sample has both dielectric and magnetic storage, which may result in high EAB values. However, the $F_{15}M_{85}$ sample did not achieve full impedance matching, resulting in a low reflection loss value. The $F_{15}M_{85}$ sample demonstrated reflection loss values of -22.54 dB at 15.13 GHz and -17.61 dB at 11.44 GHz for 3 mm and 4 mm thicknesses, with corresponding EAB values of 4.63 GHz and 4.32 GHz, respectively. The $F_{20}M_{80}$ sample exhibits elevated μ" values and diminished ε" values, indicating that the loss mainly originates from magnetic interaction, a conclusion supported by the remarkable tanδμ value. Furthermore, the elevated μ' and ε" values indicate the existence of both dielectric and magnetic storage in the sample, which could result in increased EAB values. The $F_{20}M_{80}$ samples with thicknesses of 2 mm, 3 mm, 4 mm, and 5 mm exhibit high reflection losses due to relatively good impedance matching. The $F_{20}M_{80}$ sample, with thicknesses of 2 mm, 3 mm, 4 mm, and 5 mm, exhibited reflection loss performances of -23.19 dB, -30.37 dB, -26.87 dB, and -25.45 dB at 17.96 GHz, 10.96 GHz, 8.24 GHz, and 6.51 GHz, respectively. The EAB values are 3.95> GHz, 6.13 GHz, 3.74 GHz and 3.27 GHz, respectively.

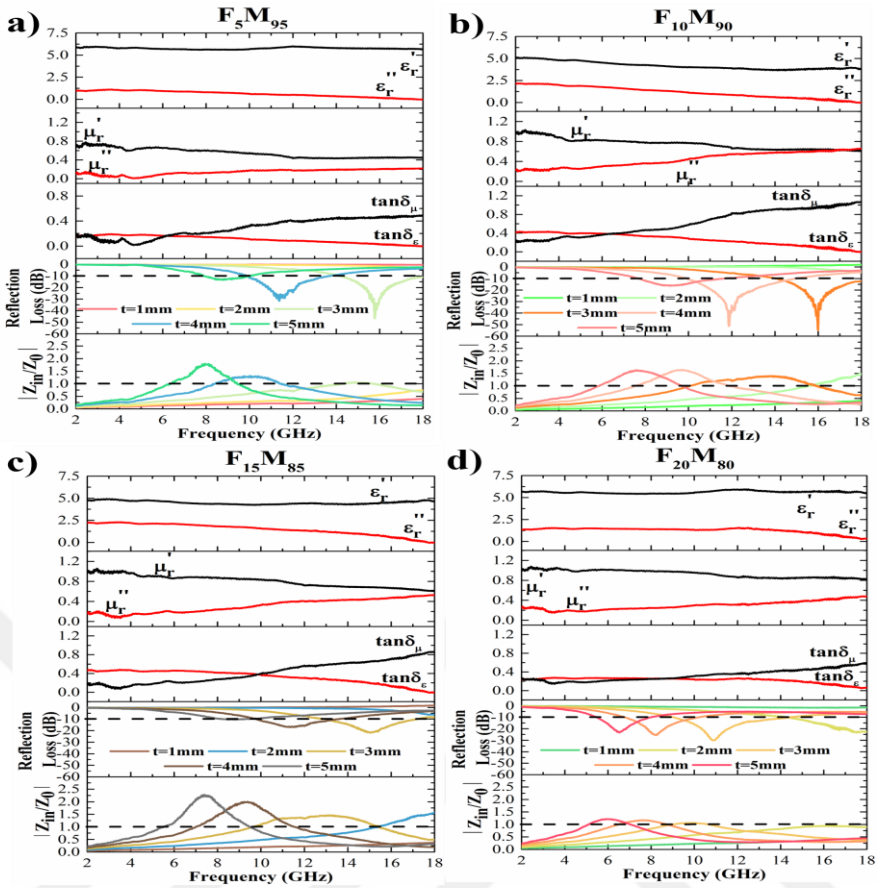

Figure 4.10. Frequency dependence of relative complex permittivity, relative complex permeability, dielectric and magnetic loss tangent, reflection loss and impedance matching($|Z_{in} / Z_0|$) of a) F_5M_{95}, b) $F_{10}M_{90}$, c) $F_{15}M_{85}$ and d) $F_{20}M_{80}$.

Figure 4.11a-f shows the relative complex permittivity, relative complex permeability, dielectric and magnetic loss tangent, reflection loss and impedance matching curves for $P_{25}F_{3.75}M_{71.25}$, $P_{50}F_{2.5}M_{47.5}$, $P_{75}F_{1.25}M_{23.75}$, $P_{25}F_{7.5}M_{67.5}$, $P_{50}F_5M_{45,}$ $P_{75}F_{2.5}M_{22.5}$ samples. The $P_{25}F_{3.75}M_{71.25}$ sample exhibits high values of μ" and negative values of ε", indicating that the loss is entirely due to magnetic interaction. This interpretation is further supported by the high value of tanδμ and the negative value of tanδε. The values of μ' and ε" suggest that the sample has both dielectric and magnetic storage, which may result in high EAB values. Additionally, the samples of $P_{25}F_{3.75}M_{71.25}$ with thicknesses of 3 mm, 4 mm, and 5 mm demonstrate relatively good impedance matching, resulting in relatively high reflection loss. The sample $P_{25}F_{3.75}M_{71.25}$, with thicknesses of 3 mm, 4 mm, and 5 mm, showed reflection loss values of -31.92 dB at 13.13 GHz, -44.98 dB at 9.43 GHz, and -23.96 dB at 7.27 GHz, respectively,

along with corresponding EAB values of 6.14 GHz, 4.67 GHz, and 4.07 GHz. The nearly zero values of μ" and ε" in the $P_{50}F_{2.5}M_{47.5}$ sample indicate that the magnetic and dielectric losses will be low. Also, the fact that $\tan\delta_\mu$ and $\tan\delta_\varepsilon$ are very close to zero supports our interpretation. The values of μ' and ε" suggest that the sample has both dielectric and magnetic storage, which may result in high EAB values. The $P_{50}F_{2.5}M_{47.5}$ sample also exhibits relatively high reflection loss at the 2 mm and 3 mm thicknesses due to impedance matching. $P_{50}F_{2.5}M_{47.5}$ samples with 2 mm, 3 mm, 4 mm and 5 mm thickness showed reflection loss performance of -27.58 dB, -16.78 dB, -16.01 dB and -15.30 dB at 13.18 GHz, 7.97 GHz, 6.12 GHz and 4.77 GHz, respectively. EAB values were determined as 8.03 GHz, 4.29 GHz, 2.60 GHz and 1.91 GHz, respectively. The $P_{75}F_{1.25}M_{23.75}$ sample exhibits low magnetic and dielectric losses, as indicated by the nearly zero values of μ" and ε". This is further supported by the close-to-zero values of tanδμ and tanδε. The high values of μ' and ε" indicate that there is dielectric and magnetic storage in the sample, and as a result, the EAB values may be high. Furthermore, the samples of $P_{75}F_{1.25}M_{23.75}$ exhibit a relatively high reflection loss at 3 mm, 4 mm, and 5 mm thickness due to their impedance matching. The sample of $P_{75}F_{1.25}M_{23.75}$, with thicknesses of 3 mm, 4 mm, and 5 mm, showed reflection loss values of -16.78 dB at 11.44 GHz, -19.63 dB at 8.29 GHz, and -17.49 dB at 6.61 GHz, respectively. The corresponding EAB values were 3.91 GHz, 2.77 GHz, and 2.28 GHz. The $P_{25}F_{7.5}M_{67.5}$ sample exhibits low levels of magnetic and dielectric loss, as evidenced by the near-zero values of μ" and ε". The interpretation is supported by the fact that both tanδμ and tanδε are very close to zero. The high values of μ' and ε" indicate that there is dielectric and magnetic storage in the sample, and as a result, the EAB values may be high. Additionally, the $P_{25}F_{7.5}M_{67.5}$ sample is not impedance-matched, resulting in low reflection loss in these samples. The $P_{25}F_{7.5}M_{67.5}$ sample with 2 mm and 3 mm thickness showed a reflection loss performance of -16.01 dB and -15.24 dB at 15.41 GHz and 13.34 GHz, respectively. EAB values were determined as 5.69 GHz and 4.72 GHz, respectively. The $P_{50}F_5M_{45}$ sample exhibits very low values of μ" and ε", indicating low levels of magnetic and dielectric loss. The close similarity between tanδμ and tanδε supports our interpretation. The high values of μ' and ε' indicate that there is dielectric and magnetic storage in the sample. As a result, the EAB values can be high if the reflection loss is high. The $P_{50}F_5M_{45}$ sample exhibits ideal impedance matching for thicknesses of 3 mm, 4 mm, and 5 mm, resulting in high reflection loss in these samples. The $P_{50}F_5M_{45}$ sample with 3 mm, 4 mm and 5 mm thickness showed reflection loss performance of -39.89 dB, -43.49 dB

and -55.72 dB at 13.33 GHz, 10.12 GHz and 7.86 GHz, respectively. EAB values were determined as 7.65 GHz, 5.42 GHz and 4.26 GHz, respectively. The sample $P_{75}F_{2.5}M_{22.5}$ displays low levels of magnetic and dielectric loss, as indicated by the very low values of μ" and ε". Also, the fact that $\tan\delta_\mu$ and $\tan\delta_\varepsilon$ are very close to zero supports our interpretation. The values of μ' and ε' indicate that the sample has both dielectric and magnetic storage, which can result in high EAB values if the reflection loss is high. Moreover, in the case of $P_{75}F_{2.5}M_{22.5}$, impedance matching is relatively achieved in the 4 mm and 5 mm thickness samples, so these samples have a small amount of reflection loss. The sample $P_{75}F_{2.5}M_{22.5}$, with thicknesses of 4 mm and 5 mm, showed reflection loss values of -16.79 dB at 9.44 GHz and -40.13 dB at 5.42 GHz, respectively. Additionally, the corresponding EAB values were 2.28 GHz and 2.02 GHz.

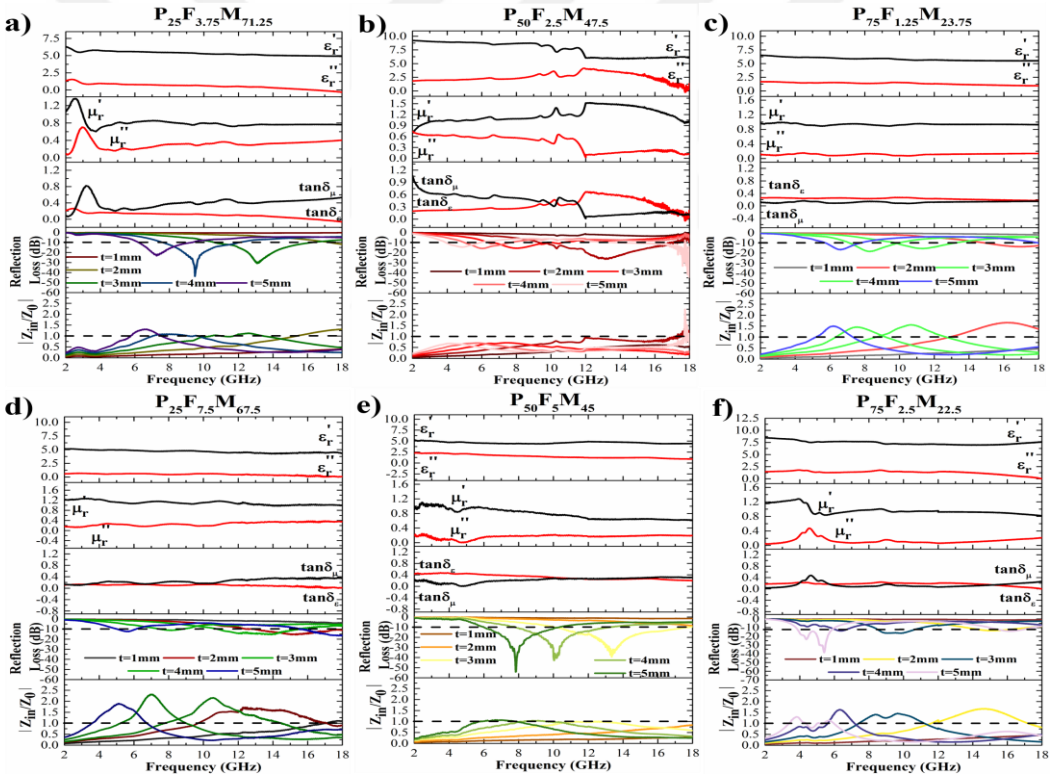

Figure 4.11. Frequency dependence of relative complex permittivity, relative complex permeability, dielectric, magnetic loss tangent values, reflection loss and impedance matching ($|Z_{in} / Z_0|$) of a) $P_{25}F_{3.75}M_{71.25}$, b) $P_{50}F_{2.5}M_{47.5}$, c) $P_{75}F_{1.25}M_{23.75}$, d) $P_{25}F_{7.5}M_{67.5}$, e) $P_{50}F_5M_{45}$, f) $P_{75}F_{2.5}M_{22.5}$.

Figure 4.12a-f shows the relative complex permittivity, relative complex permeability, dielectric and magnetic loss tangent, reflection loss and impedance matching curves for $P_{25}F_{11.25}M_{63.75}$, $P_{50}F_{7.5}M_{42.5}$,$P_{75}F_{3.75}M_{21.25}$, $P_{25}F_{15}M_{60}$, $P_{50}F_{10}M_{40}$, $P_{75}F_{5}M_{20}$.

The sample $P_{25}F_{11.25}M_{63.75}$ shows low levels of magnetic and dielectric loss, as indicated by the very low values of μ" and ε". Additionally, the fact that tanδμ and tanδε are very close to zero supports this interpretation. The high values of μ' and ε' suggest that there is dielectric and magnetic storage in the sample, which can result in high EAB values if the reflection loss is high. However, reflection loss could not be detected in the $P_{25}F_{11.25}M_{63.75}$ sample since impedance matching was not achieved. The $P_{50}F_{7.5}M_{42.5}$ sample exhibits high μ" and low ε" values, indicating a higher magnetic loss. In addition, the high tanδμ also supports our interpretation. The high values of μ' and ε' indicate that there is dielectric and magnetic storage in the sample and as a result, the EAB values can be high if the reflection loss is high. Moreover, the reflection losses in the $P_{50}F_{7.5}M_{42.5}$ sample are relatively high since the impedance matching is achieved in 3 mm, 4 mm and 5 mm thickness samples. The $P_{50}F_{7.5}M_{42.5}$ sample with 3 mm, 4 mm and 5 mm thickness showed reflection loss performance of -26.26 dB, -30.65 dB and -44.02 dB at 10.14 GHz, 7.59 GHz and 5.69 GHz, respectively. EAB values were determined as 2.93 GHz, 2.45 GHz and 1.73 GHz, respectively. The $P_{75}F_{3.75}M_{21.25}$ sample exhibits low μ" and high ε" values, indicating a higher dielectric loss. The high tanδε values further support this interpretation. Additionally, the high μ' and ε' values suggest the presence of both dielectric and magnetic storage in the sample, potentially resulting in high EAB values if the reflection loss is also high. However, reflection losses are low in the $P_{75}F_{3.75}M_{21.25}$ sample because impedance matching is not fully achieved. The sample $P_{75}F_{3.75}M_{21.25}$, with thicknesses of 3 mm, 4 mm, and 5 mm, exhibited reflection loss performances of -12.45 dB, -15.30 dB, and -14.58 dB at 11.28 GHz, 8.30 GHz, and 5.69 GHz, respectively. EAB values were determined as 3.14 GHz, 2.45 GHz and 1.68 GHz, respectively. The $P_{25}F_{15}M_{60}$ sample exhibits low values of μ" and ε", indicating low dielectric and magnetic loss. The close proximity of the tanδμ and tanδε values supports this interpretation. The high values of μ' and ε' suggest the presence of dielectric and magnetic storage in the sample, which may result in high EAB values if the reflection loss is high. However, since the impedance matching in the $P_{25}F_{15}M_{60}$ sample is relatively high in the 3 mm, 4 mm and 5 mm thicknesses, the reflection losses are relatively high. The $P_{25}F_{15}M_{60}$ sample showed reflection loss performance of -18.92 dB, -22.54 dB and -23.25 dB at 17.58

GHz, 12.53 GHz and 9.01 GHz at 3 mm, 4 mm and 5 mm thickness, respectively. EAB values were determined as 3.24> GHz, 7.01 GHz and 5.60 GHz, respectively. The $P_{50}F_{10}M_{40}$ sample exhibits low values of μ'' and ε'', indicating low dielectric and magnetic loss. The close proximity of the tanδμ and tanδε values supports this interpretation. The high values of μ' and ε' suggest the presence of dielectric and magnetic storage in the sample, which may result in high EAB values if the reflection loss is high. However, reflection losses are low in the $P_{50}F_{10}M_{40}$ sample because impedance matching is not achieved. The reflection loss performance of the $P_{50}F_{10}M_{40}$ sample was -16.01 dB at 16.66 GHz and -16.01 dB at 9.01 GHz for thicknesses of 2 mm and 3 mm. EAB values were determined as 4.33> GHz and 3.31 GHz, respectively. The fact that μ'' value is zero and ε'' values are high in $P_{75}F_5M_{20}$ sample indicates that dielectric loss will occur. Also, the zero value of tanδμ and high value of tanδε support our interpretation. The high values of μ' and ε' indicate that there is dielectric and magnetic storage in the sample and as a result, the EAB values can be high if the reflection loss is high. However, reflection losses are low in the $P_{75}F_5M_{20}$ sample because impedance matching is not achieved. The $P_{75}F_5M_{20}$ sample exhibited reflection loss performance of -17.20 dB, -15.60 dB, -17.20 dB, and -16.42 dB at 16.51 GHz, 10.74 GHz, 7.91 GHz, and 6.32 GHz, respectively, for thicknesses of 2 mm, 3 mm, 4 mm, and 5 mm. The EAB values are 4.26> GHz, 3.45 GHz, 2.66 GHz and 2.16 GHz, respectively.

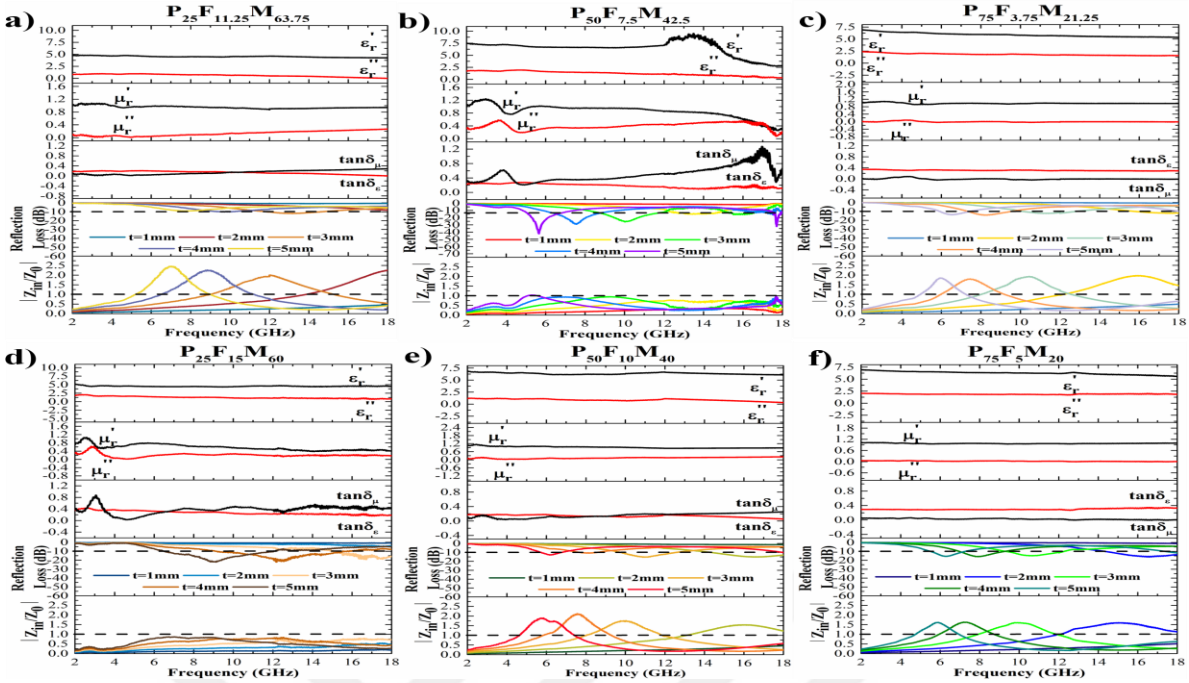

Figure 4.12. Frequency dependence of relative complex permittivity, relative complex permeability, dielectric, magnetic loss tangent values, reflection loss and impedance matching ($|Z_{in} / Z_0|$) of a) $P_{25}F_{11.25}M_{63.75}$, b) $P_{50}F_{7.5}M_{42.5}$, c) $P_{75}F_{3.75}M_{21.25}$, d) $P_{25}F_{15}M_{60}$, e) $P_{50}F_{10}M_{40}$ f) $P_{75}F_5M_{20}$.

Figure 4.13a-f shows the relative complex permittivity, relative complex permeability, dielectric and magnetic loss tangent, reflection loss and impedance matching curves for $P_{25}M_{75}$, $P_{50}M_{50}$, $P_{75}M_{25}$, $P_{25}F_{75}$, $P_{50}F_{50}$, $P_{75}F_{25}$. The $P_{25}M_{75}$ sample exhibits a higher μ" value than ε" value, indicating a higher magnetic loss. Additionally, the higher tanδμ compared to tanδε supports this interpretation. The high values of μ' and ε' suggest the presence of both dielectric and magnetic storage in the sample, potentially leading to high EAB values if the reflection loss is also high. However, the reflection losses are low in the $P_{25}M_{75}$ sample because the impedance matching is not fully achieved. The $P_{25}M_{75}$ sample with 3 mm, 4 mm and 5 mm thickness showed a reflection loss performance of -17.26 dB, -14.94 dB and -15.65 dB at 12.55 GHz, 9.38 GHz and 7.51 GHz, respectively. EAB values were determined as 5.32 GHz, 4.01 GHz and 3.28 GHz, respectively. The $P_{50}M_{50}$ sample exhibits a higher μ" value than ε" value, indicating a higher magnetic loss. Additionally, the higher tanδμ compared to tanδε supports this interpretation. The high values of μ' and ε' suggest the presence of both dielectric and magnetic storage in the sample, potentially leading to high EAB values if the

reflection loss is also high. However, in the $P_{50}M_{50}$ sample, the reflection losses are low because the impedance matching is not fully achieved. The $P_{50}M_{50}$ sample, with a thickness of 5 mm, demonstrated a reflection loss of -29.25 dB at 16.11 GHz, and the EAB value was determined as 3.36 GHz. In the $P_{75}M_{25}$ sample, the μ" and ε" values are close to zero, indicating low magnetic and dielectric loss. The tanδμ and tanδε values being close to zero further support this interpretation. The high values of μ' and ε' indicate dielectric and magnetic storage in the sample, which can result in high EAB values if the reflection loss is high. However, the reflection losses are low in the $P_{75}M_{25}$ sample because the impedance matching is not fully achieved. The sample $P_{75}M_{25}$, which has a thickness of 5 mm, showed a reflection loss of -24.73 dB at 18.00 GHz, and the EAB value was determined to be 2.28 GHz. The $P_{25}F_{75}$ sample exhibits zero μ" and ε" values, indicating no magnetic or dielectric loss. The fact that tanδμ and tanδε are also zero supports this interpretation. The high values of μ' and ε' suggest the presence of dielectric and magnetic storage in the sample, potentially leading to high EAB values if the reflection loss is high. However, no reflection loss could be detected in the $P_{25}F_{75}$ sample since impedance matching was not achieved. In the $P_{50}F_{50}$ sample, μ" value is very close to zero and ε" value is zero, indicating that there will be a low magnetic loss. Also, the fact that $\tan\delta_{\mu}$ is close to zero and tanδε is also zero supports our interpretation. The high values of μ' and ε' indicate that there is dielectric and magnetic storage in the sample and as a result, the EAB values can be high if the reflection loss is high. However, reflection losses are low in the $P_{50}F_{50}$ sample because impedance matching is not fully achieved. The sample $P_{50}F_{50}$, which has a thickness of 5 mm, exhibited a reflection loss of -23.19 dB at 16.06 GHz, and the EAB value was determined to be 2.94 GHz. The relatively high values of μ" and ε" in the $P_{75}F_{25}$ sample indicate that magnetic and dielectric loss will occur. Also, the fact that $\tan\delta_{\mu}$ and $\tan\delta_{\varepsilon}$ are the same supports our interpretation. The high values of μ' and ε' indicate that there is dielectric and magnetic storage in the sample and as a result, the EAB values can be high if the reflection loss is high. Moreover, the reflection losses are relatively high in the $P_{75}F_{25}$ sample because impedance matching is relatively achieved. The $P_{25}F_{75}$ sample, varying in thicknesses of 3 mm, 4 mm, and 5 mm, exhibited reflection loss values of -27.76 dB at 12.04 GHz, -23.96 dB at 9.10 GHz, and -24.73 dB at 7.17 GHz, along with

corresponding EAB values of 6.33 GHz, 3.74 GHz, and 2.99 GHz, respectively.

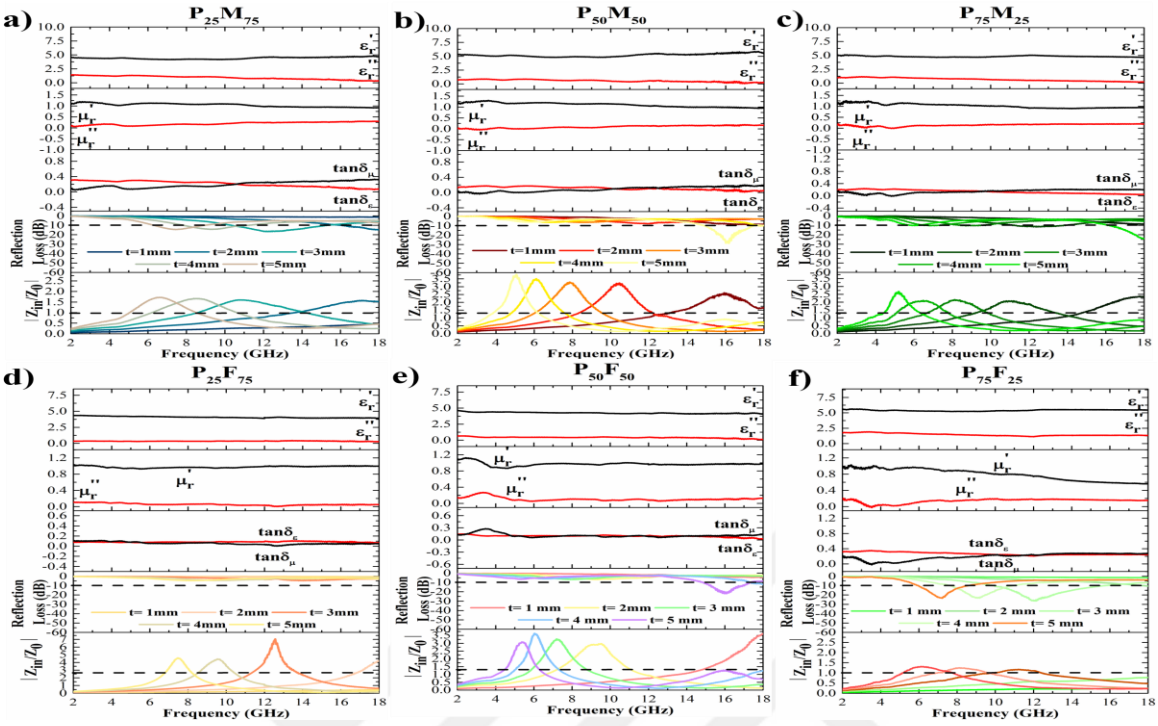

Figure 4.13. Frequency dependence of relative complex permittivity, relative complex permeability, dielectric, magnetic loss tangent values, reflection loss and impedance matching ($|Z_{in}/Z_0|$) of a) $P_{25}M_{75}$, b) $P_{50}M_{50}$, c) $P_{75}M_{25}$, d) $P_{25}F_{75}$, e) $P_{50}F_{50}$, f) $P_{75}F_{25}$.

An important factor that can affect the absorption of electromagnetic waves is attenuation matching. Attenuation matching is a concept that aims to optimize the losses encountered by electromagnetic waves scattering in a structure. In this case, attenuation matching can be defined by the ability and speed of converting incoming electromagnetic wave energy into other forms of energy [18-20]. Attenuation matching is especially critical when studying radar absorbing composite structures. In this context, attenuation matching refers to the losses due to scattering within the radar absorbing material. These losses are energy losses that occur during the dispersion of electromagnetic waves within the material. The higher the attenuation constant (α) of a material, the closer it is to attenuation matching. The formula expressing the proximity to attenuation matching is as follows:

$$\alpha = \frac{\sqrt{2}\pi f}{c}\sqrt{(\mu''\varepsilon'' - \mu'\varepsilon') + \sqrt{(\mu''\varepsilon'' - \mu'\varepsilon')^2 + (\mu'\varepsilon'' + \mu''\varepsilon')^2}} \qquad (4.3)$$

Figure 4.14a-d illustrates the frequency dependent attenuation constants of Fe_3O_4, MoS_2, PANI, F_5M_{95}, $F_{10}M_{90}$, $F_{15}M_{85}$, $F_{20}M_{80}$, $P_{25}F_{3.75}M_{71.25}$, $P_{50}F_{2.5}M_{47.5}$, $P_{75}F_{1.25}M_{23.75,}$ $P_{25}F_{7.5}M_{67.5}$, $P_{50}F_5M_{45}$, $P_{75}F_{2.5}M_{22.50,}$ $P_{25}F_{11.25}M_{63.75}$, $P_{50}F_{7.5}M_{42.5}$, $P_{75}F_{3.75}M_{21.25,}$ $P_{25}F_{15}M_{60}$, $P_{50}F_{10}M_{40}$, $P_{75}F_5M_{25}$, $P_{25}M_{75}$, $P_{50}M_{50}$, $P_{75}M_{25}$, $P_{25}F_{75}$, $P_{50}F_{50}$, $P_{75}F_{25}$ samples. Figure 4.14a-d shows that samples with magnetic or dielectric interactions have lower attenuation constant values and non-linear or decreasing curves. This can be explained by the electromagnetic wave entering the magnetic or dielectric interaction before scattering. Thus, the absorption mechanism resulting from the conversion of electromagnetic waves into heat energy is less effective in these samples. Samples with high attenuation constant values, which increase linearly, indicate that the electromagnetic wave scattering within the structure is high. As a result, the electromagnetic wave can be absorbed by converting it into heat energy. However, simply converting the scattered electromagnetic wave into heat is not enough to improve electromagnetic wave absorption performance. Our results are consistent with these comments.

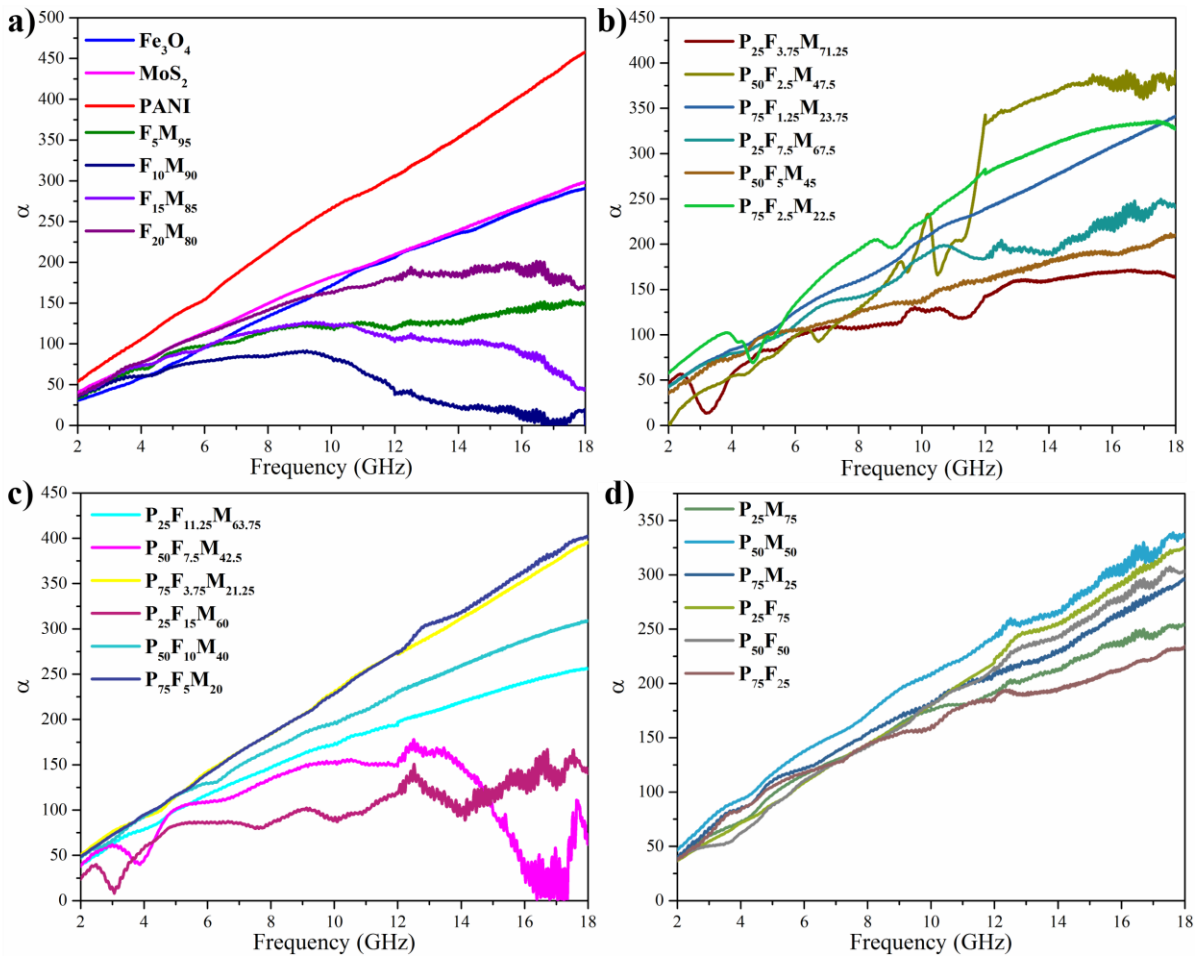

Figure 4.14. Frequency dependent attenuation constant a) Fe_3O_4, MoS_2, PANI, F_5M_{95}, $F_{10}M_{90}$, $F_{15}M_{85}$, $F_{20}M_{80}$ b) $P_{25}F_{3.75}M_{71.25}$, $P_{50}F_{2.5}M_{47.5}$, $P_{75}F_{1.25}M_{23.75}$, $P_{25}F_{7.5}M_{67.5}$, $P_{50}F_5M_{45}$, $P_{75}F_{2.5}M_{22.50}$ c) $P_{25}F_{11.25}M_{63.75}$, $P_{50}F_{7.5}M_{42.5}$, $P_{75}F_{3.75}M_{21.25}$, $P_{25}F_{15}M_{60}$, $P_{50}F_{10}M_{40}$, $P_{75}F_5M_{25}$ d) $P_{25}M_{75}$, $P_{50}M_{50}$, $P_{75}M_{25}$, $P_{25}F_{75}$, $P_{50}F_{50}$, $P_{75}F_{25}$.

Electromagnetic wave absorbing materials provide their magnetic losses from types of magnetic losses such as hysteresis, field wall resonance, natural resonance and eddy current loss. In low electromagnetic fields, hysteresis loss is negligible. Domain wall resonance is typically evident in the low frequency range (<2 GHz). Therefore, the magnetic loss of materials is mainly due to natural resonance and eddy current, particularly in the gigahertz range. Eddy current loss refers to the energy loss due to the currents swirling in the material due to the variation of the magnetic field. The eddy current loss (C_0) equation is given below.

$$C_0 = \mu''(\mu')^{-2} f^{-1} \tag{4.4}$$

If the magnetic loss of the materials is only due to the eddy current, the value of C_0 should remain constant depending on the frequency variation. Figure 4.15a-d illustrates the frequency dependent eddy current (C_0) loss of Fe_3O_4, MoS_2, PANI, F_5M_{95}, $F_{10}M_{90}$, $F_{15}M_{85}$, $F_{20}M_{80}$, $P_{25}F_{3.75}M_{71.25}$, $P_{50}F_{2.5}M_{47.5}$, $P_{75}F_{1.25}M_{23.75,}$ $P_{25}F_{7.5}M_{67.5}$, $P_{50}F_5M_{45}$, $P_{75}F_{2.5}M_{22.50,}$ $P_{25}F_{11.25}M_{63.75}$, $P_{50}F_{7.5}M_{42.5}$, $P_{75}F_{3.75}M_{21.25,}$ $P_{25}F_{15}M_{60}$, $P_{50}F_{10}M_{40}$, $P_{75}F_5M_{25}$, $P_{25}M_{75}$, $P_{50}M_{50}$, $P_{75}M_{25}$, $P_{25}F_{75}$, $P_{50}F_{50}$, $P_{75}F_{25}$ samples. In Figure 4.15a, the increase in C_0 value after about 6 GHz in F_5M_{95}, $F_{10}M_{90}$ and $F_{15}M_{85}$ samples indicates that these samples have a magnetic loss due to natural resonance. The C_0 values of Fe_3O_4, MoS_2 and PANI samples remain constant and very close to zero, indicating that these samples do not have eddy current and natural resonance loss. The constant C_0 value of the $F_{20}M_{80}$ sample indicates that it creates eddy current in the structure. In Figure 4.15b, the increases and decreases in C_0 values after about 4 GHz in $P_{25}F_{3.75}M_{71.25}$, $P_{50}F_{2.5}M_{47.5}$, $P_{25}F_{7.5}M_{67.5}$ and $P_{75}F_{2.5}M_{22.5}$ samples indicate that these samples have a magnetic loss due to natural resonance. Moreover, C_0 values remain constant after 12 GHz, indicating that these samples also have eddy current. The C_0 values of the $P_{75}F_{1.25}M_{23.75}$ and $P_{50}F_5M_{45}$ samples remain constant, indicating that these samples have eddy current loss. In Figure 4.15c, the increases and decreases in the C_0 value of the $P_{50}F_{7.5}M_{42.5}$ and $P_{25}F_{15}M_{60}$ samples after about 4 GHz indicate that these samples have a magnetic loss due to natural resonance. Moreover, the peaks at about 17 GHz and 14 GHz for samples $P_{50}F_{7.5}M_{42.5}$ and $P_{25}F_{15}M_{60}$, respectively, indicate that the loss of natural resonance is severe. The constant C_0 value of the $P_{25}F_{11.25}M_{67.75}$ sample indicates that it has eddy current. The zero value of C_0 in the other samples indicates that there is no eddy current and natural resonance loss. In Figure 4.15d, the increase in C_0 value and some peaks in $P_{75}F_{25}$ and $P_{25}M_{75}$ samples after about 4 GHz indicate that these samples have a magnetic loss due to natural resonance. The increases and decreases in C_0 between about 4-12 GHz in the other samples indicate a loss due to natural resonance, while the constant C_0 value after 12 GHz indicates eddy current loss.

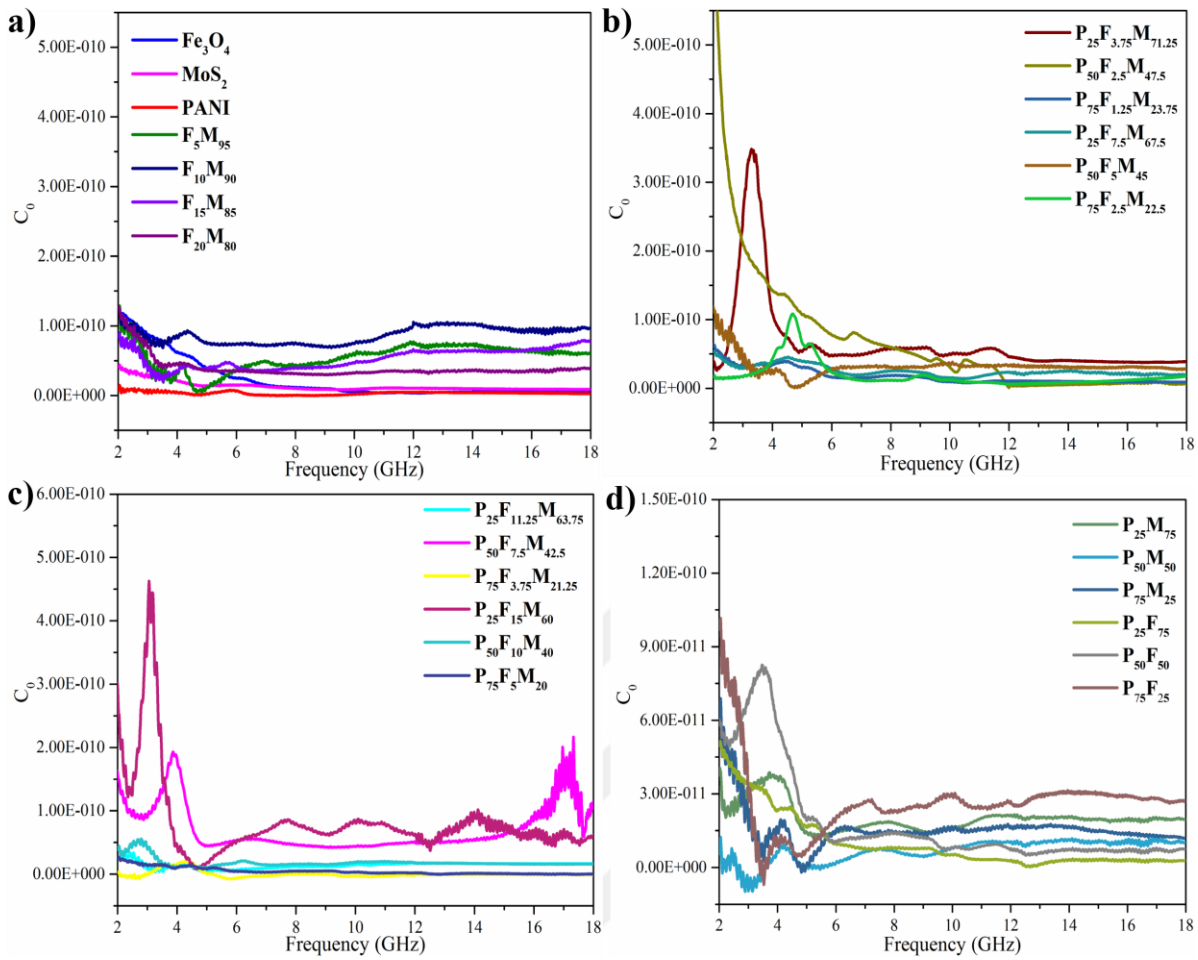

Figure 4.15. Frequency dependent eddy current (C_0) loss a) Fe_3O_4, MoS_2, PANI, F_5M_{95}, $F_{10}M_{90}$, $F_{15}M_{85}$, $F_{20}M_{80}$ b) $P_{25}F_{3.75}M_{71.25}$, $P_{50}F_{2.5}M_{47.5}$, $P_{75}F_{1.25}M_{23.75}$, $P_{25}F_{7.5}M_{67.5}$, $P_{50}F_5M_{45}$, $P_{75}F_{2.5}M_{22.50}$ c) $P_{25}F_{11.25}M_{63.75}$, $P_{50}F_{7.5}M_{42.5}$, $P_{75}F_{3.75}M_{21.25}$, $P_{25}F_{15}M_{60}$, $P_{50}F_{10}M_{40}$, $P_{75}F_5M_{25}$ d) $P_{25}M_{75}$, $P_{50}M_{50}$, $P_{75}M_{25}$, $P_{25}F_{75}$, $P_{50}F_{50}$, $P_{75}F_{25}$.

Debye relaxation plays an important role in electromagnetic wave absorption processes. Debye relaxation describes the tendency of a dielectric material to polarize and relax under an electric field. Debye theory describes the relationship between ε″ and ε″ as follows [21, 22]:

$$\left(\varepsilon' - \frac{\varepsilon_s + \varepsilon_\infty}{2}\right)^2 + (\varepsilon'')^2 = \left(\frac{\varepsilon_s - \varepsilon_\infty}{2}\right)^2 \quad (4.5)$$

Each semicircle represents a relaxation process derived from the variations of ε″ and ε″ [23-25]. These processes are the processes by which nuclear spins exposed to the electromagnetic

wave return to the equilibrium state. The number of semicircles in the Cole-cole curve indicates the number of relaxation processes. It can be interpreted that samples with more relaxation processes have higher dielectric loss. Figure 4.16a-d shows the coole curves of Fe_3O_4, MoS_2, PANI, F_5M_{95}, $F_{10}M_{90}$, $F_{15}M_{85}$, $F_{20}M_{80}$, $P_{25}M_{75}$, $P_{50}M_{50}$, $P_{75}M_{25}$, $P_{25}F_{75}$, $P_{50}F_{50}$ and $P_{75}F_{25}$ samples. The semicircles on the cole-cole curves were identified and the relaxation process numbers were determined. These results show that our samples have dielectric loss due to relaxation processes.

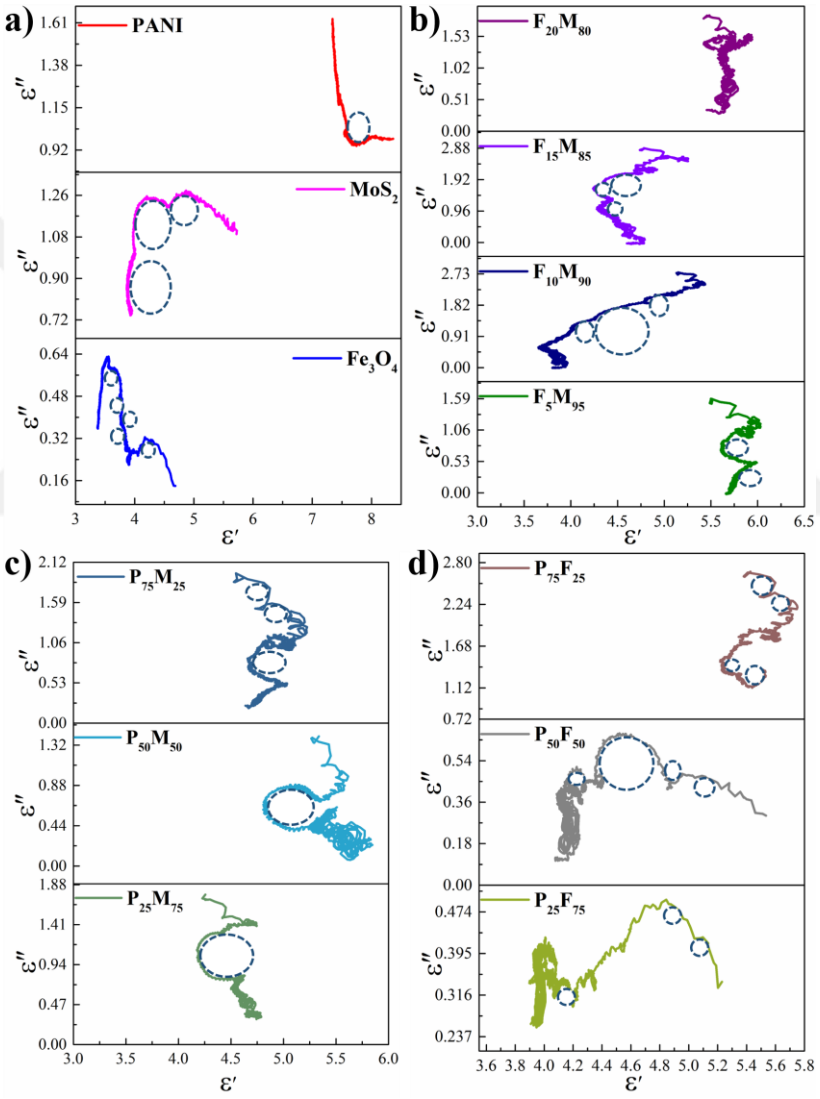

Figure 4.16. Cole-cole curves of a) Fe_3O_4, MoS_2, PANI b) F_5M_{95}, $F_{10}M_{90}$, $F_{15}M_{85}$, $F_{20}M_{80}$ c) $P_{25}M_{75}$, $P_{50}M_{50}$, $P_{75}M_{25}$ d) $P_{25}F_{75}$, $P_{50}F_{50}$, $P_{75}F_{25}$.

Figure 4.16a-d shows the coole curves of $P_{25}F_{3.75}M_{71.25}$, $P_{50}F_{2.5}M_{47.5}$, $P_{75}F_{1.25}M_{23.75}$, $P_{25}F_{7.5}M_{67.5}$, $P_{50}F_{5}M_{45}$, $P_{75}F_{2.5}M_{22.50}$, $P_{25}F_{11.25}M_{63.75}$, $P_{50}F_{7.5}M_{42.5}$, $P_{75}F_{3.75}M_{21.25}$, $P_{25}F_{15}M_{60}$, $P_{50}F_{10}M_{40}$ and $P_{75}F_{5}M_{25}$ samples. The semicircles on the cole-cole curves were identified and the relaxation process numbers were determined. These results show that our samples have dielectric loss due to relaxation processes. All of our samples exhibit a relaxation process, which can be explained by the fundamental property of electromagnetic waves. These waves consist of perpendicular electric and magnetic field components that are directly proportional to each other. Therefore, when one field changes, the other changes as well. Additionally, it is important to note that the dielectric properties of magnetic materials can also impact the dielectric loss.

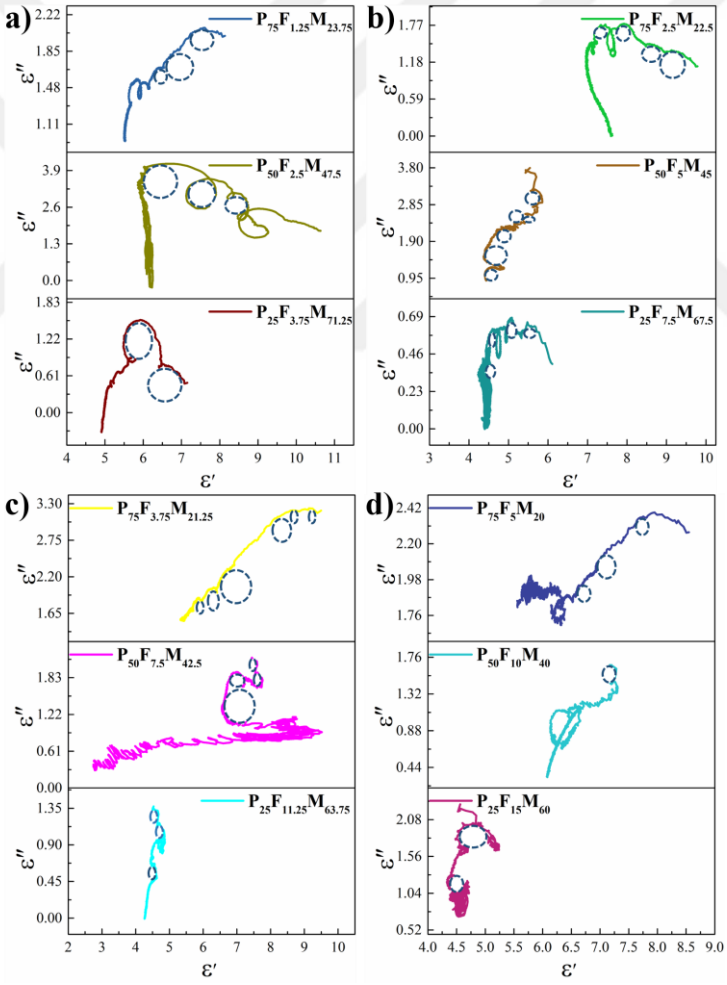

Figure 4.17. Cole-cole curves of a) $P_{25}F_{3.75}M_{71.25}$, $P_{50}F_{2.5}M_{47.5}$, $P_{75}F_{1.25}M_{23.75}$ b) $P_{25}F_{7.5}M_{67.5}$, $P_{50}F_{5}M_{45}$, $P_{75}F_{2.5}M_{22.50}$ c) $P_{25}F_{11.25}M_{63.75}$, $P_{50}F_{7.5}M_{42.5}$, $P_{75}F_{3.75}M_{21.25}$ d) $P_{25}F_{15}M_{60}$, $P_{50}F_{10}M_{40}$, $P_{75}F_{5}M_{25}$.

Table 4.1 displays the results of the electromagnetic wave absorption performance of the synthesized samples. The samples synthesized in this study exhibited high electromagnetic wave absorption performance due to good impedance matching, which was achieved through polarization and conductivity loss with PANI, dielectric and multiple reflection loss with MoS_2, and natural resonance and eddy current loss with Fe_3O_4.

Table 4.1. Electromagnetic wave absorption performans parameters of our samples.

Sample Codes	Thickness (mm)	Frequency (GHz)	RL (dB)	EAB (GHz)
F	-	-	-	-
M	-	-	-	-
P	5.0	16.45	-20.41	2.89
F_5M_{95}	3.0	15.80	-31.38	4.0
	4.0	11.36	-47.59	4.27
$F_{10}M_{90}$	3.0	15.99	-54.97	4.0>
	4.0	11.89	-51.45	4.99
$F_{15}M_{85}$	3.0	15.13	-22.54	4.63
	4.0	11.44	-17.61	4.32
$F_{20}M_{80}$	2.0	17.96	-23.19	3.95>
	3.0	10.96	-30.37	6.13
	4.0	8.24	-26.87	3.74
	5.0	6.21	-25.45	3.27
$P_{25}F_{75}$	3.0	12.55	-17.26	5.32
	4.0	9.38	-14.94	4.01
	5.0	7.51	-15.65	3.28
$P_{50}F_{50}$	5.0	16.06	-23.19	2.94
$P_{75}F_{25}$	3.0	12.04	-27.76	6.33
	4.0	9.10	-23.96	3.74
	5.0	7.17	-24.73	2.99
$P_{25}M_{75}$	3.0	12.55	-17.26	5.32
	4.0	9.38	-14.94	4.01
	5.0	7.51	-15.65	3.28
$P_{50}M_{50}$	5.0	16.11	-29.25	3.36
$P_{75}M_{25}$	5.0	18.00	-24.73	2.28>

	3.0	13.13	-31.92	6.14
$P_{25}F_{3.75}M_{71.25}$	4.0	9.43	-44.98	4.67
	5.0	7.27	-23.96	4.07
	2.0	13.18	-27.58	8.03
$P_{50}F_{2.5}M_{47.5}$	3.0	7.97	-16.78	4.29
	4.0	6.12	-16.01	2.60
	5.0	4.77	-15.30	1.91
	3.0	11.44	-16.78	3.91
$P_{75}F_{1.25}M_{23.75}$	4.0	8.29	-19.63	2.77
	5.0	6.61	-17.49	2.28
	2.0	15.41	-16.01	5.69
$P_{25}F_{7.5}M_{67.5}$	3.0	13.34	-15.24	4.72
	3.0	13.33	-39.96	7.65
$P_{50}F_{5}M_{45}$	4.0	10.12	-42.72	5.42
	5.0	7.86	-54.97	4.26
	4.0	9.44	-16.79	2.28
$P_{75}F_{2.5}M_{22.5}$	5.0	5.42	-40.13	2.02
$P_{25}F_{11.25}M_{63.75}$	-	-	-	-
	3.0	10.14	-26.26	2.93
$P_{50}F_{7.5}M_{42.5}$	4.0	7.59	-30.65	2.45
	5.0	5.69	-44.02	1.73
	3.0	11.28	-12.45	3.14
$P_{75}F_{3.75}M_{21.25}$	4.0	8.30	-15.30	2.45
	5.0	5.69	-14.58	1.68
	3.0	17.58	-18.92	3.24>
$P_{25}F_{15}M_{60}$	4.0	12.53	-22.54	7.01
	5.0	9.01	-23.25	5.60
	2.0	16.66	-16.01	4.33>
$P_{50}F_{10}M_{40}$	3.0	9.01	16.01	3.31
	2.0	16.51	-17.20	4.26>
	3.0	10.74	-15.60	3.45
$P_{75}F_{5}M_{20}$	4.0	7.91	-17.20	2.66
	5.0	6.32	-16.42	2.16

In this study, the reflection loss mechanism in the PANI@Fe_3O_4:MoS_2 hybrid structure can be described by four main factors. First, it is impedance matching, which is the basis of electromagnetic wave absorption. The conductive PANI, magnetic Fe_3O_4 and layered MoS_2 in the structure we obtained allow the incident electromagnetic wave to penetrate into the samples more easily by providing impedance matching [62-64]. Secondly, as a result of the penetration of the electromagnetic wave into the samples, multiple scattering can be achieved due to the effect of the hybrid components [65]. Moreover, PANI and Fe_3O_4 between the layers of MoS_2 with layered structure can interact with the electromagnetic wave by the formation of scattering [65]. As a result, natural resonance and eddy current loss may occur. Thirdly, dielectric loss has a significant effect on electromagnetic wave absorption [65-67]. The PANI@Fe_3O_4:MoS_2 hybrid structure plays an important role in the accumulation of free charges, facilitates their polarization, and can act as a capacitor by storing the energy from the electromagnetic wave [68, 69]. Finally, a circulation of polarized electrons occurs between the PANI and MoS_2 nanostructures and this circulation provides high conductivity within the hybrid structure, allowing the electromagnetic wave to lose its energy. This mechanism, thanks to the hybrid structure we have obtained, has enabled us to achieve superior electromagnetic wave absorption performance.

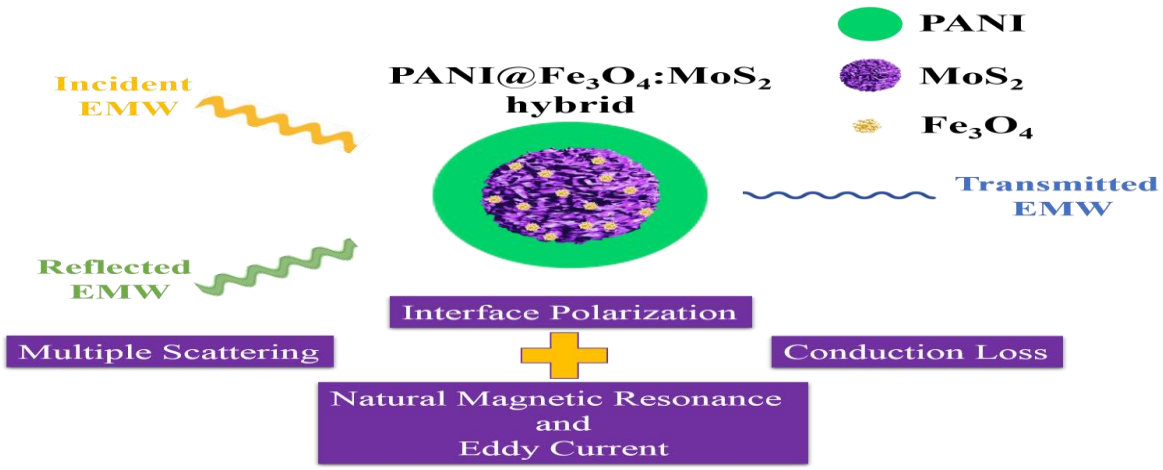

Figure 4.18. Schematic representation of the reflection loss mechanism of PANI@Fe_3O_4:MoS_2 hybrid structure.

5. CONCLUSIONS

This work presents a systematic investigation of the structural, magnetic, thermal, morphological, and electromagnetic properties of Fe_3O_4 magnetic nanoparticles, MoS_2 nanosheets, and the conducting polymer PANI, as well as their hybrid structures (Fe_3O_4:MoS_2, PANI@Fe_3O_4, PANI@MoS_2 and PANI@Fe_3O_4:MoS_2). To improve the absorption of electromagnetic waves, we carefully adjusted the relative complex permittivity and complex permeability values of the samples by using magnetic and dielectric materials.

The $F_{10}M_{90}$ sample achieved a minimum reflection loss of -54.97 dB at a thickness of 3 mm at a frequency of 7.86 GHz with an effective absorption range of 4.0> GHz. The $P_{50}F_{2.5}M_{47.5}$ sample achieved a minimum reflection loss performance of -27.58 dB with 2 mm thickness at a frequency of 13.18 GHz with an effective absorption bandwidth of 8.03 GHz. These results reveal that the PANI@Fe_3O_4:MoS_2 hybrid structure outperforms the MoS_2-based electromagnetic wave absorbers reported so far.

The results show promise for the development of high-performance electromagnetic wave-absorbing materials. These materials have potential for protecting stealth technology and sensitive electronic devices at X and Ku band frequencies.

6. RECOMMENDATIONS

This thesis rigorously investigates the structural, magnetic, thermal, morphological, and electromagnetic properties of Fe_3O_4 magnetic nanoparticles, MoS_2 nanosheets, and the conducting polymer PANI. Moreover, the hybrid structures of these components (Fe_3O_4:MoS_2, PANI@Fe_3O_4, PANI@MoS_2 and PANI@Fe_3O_4:MoS_2) have been systematically investigated. Hybrid structures formed by utilizing various dielectric, magnetic and layered materials have shown high electromagnetic wave absorption performance. In this thesis, it is aimed to increase the effective electromagnetic wave absorption range by obtaining hybrid structures. Since our thesis topic is of critical importance in the Turkish Defense Industry, the studies that can be applied in the future in the light of the gains we have obtained on this subject are listed below.

- Better results can be obtained by increasing the weight contribution ratio of hybrid structures in epoxy.
- By increasing the number of layers of 2D MoS_2 nanosheets, the number of scattering of the electromagnetic wave in the structure can be increased and as a result, the electromagnetic wave absorption performance can be increased.
- Adding hybrid structures with different doping ratios into materials such as epoxy, wax, or polymers can increase electromagnetic wave absorption performance.
- In order to eliminate the problems that may arise from the density difference of PANI while obtaining hybrid structures, doping by volume can increase the electromagnetic wave absorption performance.
- The electromagnetic wave absorption performance of the material can be enhanced by utilizing various nanostructures such as nanotubes, nanowires, and nanosheets to create hybrid structures.

REFERENCES

[1] P. Lopez-Rodriguez, R. Fernández-Recio, I. Bravo, A. Gardel, J. Lázaro, and E. Rufo, "Computational Burden Resulting from Image Recognition of High Resolution Radar Sensors," *Sensors (Basel, Switzerland)*, vol. 13, pp. 5381-402, 04/01 2013, doi: 10.3390/s130405381.

[2] H. Ahmad *et al.*, "Stealth technology: Methods and composite materials—A review," *Polymer Composites*, vol. 40, no. 12, pp. 4457-4472, 2019, doi: https://doi.org/10.1002/pc.25311.

[3] K. k. Sadasivuni, D. Ponnamma, J. Kim, and S. Thomas, *Graphene-Based Polymer Nanocomposites in Electronics*. 2014.

[4] P. Saville, D. RESEARCH, D. A. DARTMOUTH, and D. R. C.-. Atlantic, *Review of Radar Absorbing Materials*. Defence Research & Development Canada, Defence R & D Canada - Atlantic, 2005.

[5] W. D. Callister and D. G. Rethwisch, *Materials science and engineering : an introduction*, 8th edition ed. Hoboken, NJ: John Wiley & Sons (in eng), 2010.

[6] G. Verhoeven, "The reflection of two fields – Electromagnetic radiation and its role in (aerial) imaging," vol. 55, pp. 13-18, 10/25 2017, doi: 10.5281/zenodo.3534245.

[7] D. Schick, "Processing of Polymer-Metal Composites with Microwaves," 2009.

[8] N. Ismail, T. Gunawan, S. S, T. Praludi, and E. Hamidi, "Design of microstrip hairpin bandpass filter for 2.9 GHz – 3.1 GHz s-band radar with defected ground structure," *Malaysian Journal of Fundamental and Applied Sciences*, vol. 14, pp. 448-455, 01/06 2019, doi: 10.11113/mjfas.v14n4.1073.

[9] M. Getzlaff, *Fundamentals of Magnetism*. Springer Berlin Heidelberg, 2007.

[10] T.-H. Ting and K.-H. Wu, "Synthesis, characterization of polyaniline/BaFe12O19 composites with microwave-absorbing properties," *Journal of Magnetism and Magnetic Materials*, vol. 322, no. 15, pp. 2160-2166, 2010/08/01/ 2010, doi: https://doi.org/10.1016/j.jmmm.2010.02.002.

[11] D. Bogdal and A. Prociak, "Microwave-Enhanced Polymer Chemistry and Technology," *Microwave-Enhanced Polymer Chemistry and Technology*, pp. 1-275, 04/15 2008, doi: 10.1002/9780470390276.

[12] Y. Han, H. Sun, and H. Guo, "Analysis of influential factors on a space target's laser radar cross-section," *Optics & Laser Technology*, vol. 56, pp. 151-157, 2014/03/01/ 2014, doi: https://doi.org/10.1016/j.optlastec.2013.08.007.

[13] P. Saville, "Review of Radar Absorbing Materials," vol. 23, p. 62, 01/01 2005.

[14] M. Cao, X. Wang, W. Cao, X. Fang, B. Wen, and J. Yuan, "Thermally Driven Transport and Relaxation Switching Self-Powered Electromagnetic Energy Conversion," *Small*, vol. 14, no. 29, p. 1800987, 2018, doi: https://doi.org/10.1002/smll.201800987.

[15] W.-Q. Cao, X.-X. Wang, J. Yuan, W.-Z. Wang, and M.-S. Cao, "Temperature dependent microwave absorption of ultrathin graphene composites," *Journal of Materials Chemistry C*, 10.1039/C5TC02185E vol. 3, no. 38, pp. 10017-10022, 2015, doi: 10.1039/C5TC02185E.

[16] T. Shang, Q. Lu, L. Chao, Y. Qin, Y. Yun, and G. Yun, "Effects of ordered mesoporous structure and La-doping on the microwave absorbing properties of CoFe2O4," *Applied Surface Science*, vol. 434, pp. 234-242, 2018/03/15/ 2018, doi: https://doi.org/10.1016/j.apsusc.2017.10.175.

[17] Y. B. Zainal, D. Dedi, and A. Manaf, "Microstructure and Microwave Absorption Characteristics of BaTiO3-CoFe2O4 Composites," *Key Engineering Materials*, vol. 855, pp. 322-329, 2020, doi: 10.4028/www.scientific.net/KEM.855.322.

[18] X. Wang, Y. Lu, T. Zhu, S. Chang, and W. Wang, "CoFe2O4/N-doped reduced graphene oxide aerogels for high-performance microwave absorption," *Chemical Engineering Journal*, vol. 388, p. 124317, 2020/05/15/ 2020, doi: https://doi.org/10.1016/j.cej.2020.124317.

[19] J. Yan, Y. Huang, Y. Yan, X. Zhao, and P. Liu, "The composition design of MOF-derived Co-Fe bimetallic autocatalysis carbon nanotubes with controllable electromagnetic properties," *Composites Part A: Applied Science and Manufacturing*, vol. 139, p. 106107, 2020/12/01/ 2020, doi: https://doi.org/10.1016/j.compositesa.2020.106107.

[20] J. Yan *et al.*, "Polypyrrole-Based Composite Materials for Electromagnetic Wave Absorption," *Polymer Reviews*, vol. 61, no. 3, pp. 646-687, 2021/07/03 2021, doi: 10.1080/15583724.2020.1870490.

[21] Z.-J. Guan, J.-T. Jiang, N. Chen, Y.-X. Gong, and L. Zhen, "Carbon-coated CoFe–CoFe2O4 composite particles with high and dual-band electromagnetic wave absorbing properties," *Nanotechnology*, vol. 29, no. 30, p. 305604, 2018/05/23 2018, doi: 10.1088/1361-6528/aac31f.

[22] M. Zong *et al.*, "Facile preparation, high microwave absorption and microwave absorbing mechanism of RGO–Fe3O4 composites," *RSC Advances*, 10.1039/C3RA43359E vol. 3, no. 45, pp. 23638-23648, 2013, doi: 10.1039/C3RA43359E.

[23] J. Qiao *et al.*, "Non-Magnetic Bimetallic MOF-Derived Porous Carbon-Wrapped TiO2/ZrTiO4 Composites for Efficient Electromagnetic Wave Absorption," *Nano-Micro Letters*, vol. 13, no. 1, p. 75, 2021/02/17 2021, doi: 10.1007/s40820-021-00606-6.

[24] S. Gao, S.-H. Yang, H.-Y. Wang, G.-S. Wang, and P.-G. Yin, "Excellent electromagnetic wave absorbing properties of two-dimensional carbon-based nanocomposite supported by transition metal carbides Fe3C," *Carbon*, vol. 162, pp. 438-444, 2020/06/01/ 2020, doi: https://doi.org/10.1016/j.carbon.2020.02.031.

[25] T. Zhu, S. Chang, Y.-F. Song, M. Lahoubi, and W. Wang, "PVP-encapsulated CoFe2O4/rGO composites with controllable electromagnetic wave absorption performance," *Chemical Engineering Journal*, vol. 373, pp. 755-766, 2019/10/01/ 2019, doi: https://doi.org/10.1016/j.cej.2019.05.079.

[26] G. A. Rao and S. P. Mahulikar, "Integrated review of stealth technology and its role in airpower," *The Aeronautical Journal (1968)*, vol. 106, pp. 629 - 642, 2002.

[27] P. E. Eden, *Encyclopedia of modern military aircraft*. London: Amber Books Ltd. (in eng), 2006.

[28] V. M. Petrov and V. V. Gagulin, "Microwave Absorbing Materials," *Inorganic Materials*, vol. 37, no. 2, pp. 93-98, 2001/02/01 2001, doi: 10.1023/A:1004171120638.

[29] K. Gaylor and M. R. Laboratory, *Radar Absorbing Materials - Mechanisms and Materials*. DSTO Materials Research Laboratory, 1989.

[30] M. Green and X. Chen, "Recent progress of nanomaterials for microwave absorption," *Journal of Materiomics*, vol. 5, no. 4, pp. 503-541, 2019/12/01/ 2019, doi: https://doi.org/10.1016/j.jmat.2019.07.003.

[31] J. M. D. Coey, *Magnetism and Magnetic Materials*. Cambridge: Cambridge University Press, 2010.
[32] G. Xian *et al.*, "Polyaniline-Coated ZIF-67-Derived Co/C Nanostructures for Efficient Electromagnetic Wave Absorption," *ACS Applied Nano Materials*, vol. 6, no. 10, pp. 8617-8626, 2023/05/26 2023, doi: 10.1021/acsanm.3c01007.
[33] Z. Luo *et al.*, "Synthesis of Conductive Polyaniline Composites for Superior Electromagnetic Wave Absorption with Lightweight and Broad Bandwidth," *Advanced Engineering Materials*, vol. 25, no. 1, p. 2200976, 2023, doi: https://doi.org/10.1002/adem.202200976.
[34] H. Pan, L. Xu, K. Li, T. Li, Y. Shen, and L. Wang, "The electromagnetic wave absorption composite of flower-like structure NiCo2O4 and Fe3O4 derived from low-temperature preparation method," *Materials Science and Engineering: B*, vol. 296, p. 116714, 2023/10/01/ 2023, doi: https://doi.org/10.1016/j.mseb.2023.116714.
[35] X. Zeng, C. Zhao, X. Jiang, R. Yu, and R. Che, "Functional Tailoring of Multi-Dimensional Pure MXene Nanostructures for Significantly Accelerated Electromagnetic Wave Absorption," *Small*, vol. n/a, no. n/a, p. 2303393, doi: https://doi.org/10.1002/smll.202303393.
[36] W. Deng *et al.*, "Morphology modulated defects engineering from MnO2 supported on carbon foam toward excellent electromagnetic wave absorption," *Carbon*, vol. 206, pp. 192-200, 2023/03/25/ 2023, doi: https://doi.org/10.1016/j.carbon.2023.02.039.
[37] F. Dong *et al.*, "Fabrication of hierarchical reduced graphene oxide decorated with core-shell Fe3O4@polypyrrole heterostructures for excellent electromagnetic wave absorption," *Journal of Colloid and Interface Science*, vol. 649, pp. 943-954, 2023/11/01/ 2023, doi: https://doi.org/10.1016/j.jcis.2023.06.085.
[38] J. Zhang *et al.*, "Microwave-assisted hydrothermal synthesis of Fe-doped 1T/2H-MoS2 few-layer nanosheets for efficient electromagnetic wave absorbing," *Journal of Alloys and Compounds*, vol. 947, p. 169544, 2023/06/25/ 2023, doi: https://doi.org/10.1016/j.jallcom.2023.169544.
[39] G. Yu, M. Ye, A. Han, Q. Liu, Y. Su, and C. Chen, "Optimization of electromagnetic wave absorption properties of CoNi/MoSe2 composites with 3D flower-like by controlling the Co/Ni molar ratio," *Journal of Alloys and Compounds*, vol. 939, p. 168592, 2023/04/05/ 2023, doi: https://doi.org/10.1016/j.jallcom.2022.168592.
[40] T. Chen *et al.*, "Synchronously modulated the morphology and crystal defects of α-MnO2 for high-performance mono-component electromagnetic wave absorber," *Applied Surface Science*, vol. 608, p. 155024, 2023/01/15/ 2023, doi: https://doi.org/10.1016/j.apsusc.2022.155024.
[41] G. Yang, B. Wen, Y. Wang, X. Zhou, X. Liu, and S. Ding, "In situ construction of ZIF-67 derived Mo2C@cobalt/carbon composites toward excellent electromagnetic wave absorption properties," *Nanotechnology*, vol. 34, no. 18, p. 185704, 2023/02/20 2023, doi: 10.1088/1361-6528/acb655.
[42] A. Srivastava and A. Katiyar, "10 - Zinc oxide nanostructures," in *Ceramic Science and Engineering*, K. P. Misra and R. D. K. Misra Eds.: Elsevier, 2022, pp. 235-262.
[43] M. Beygisangchin, S. Abdul Rashid, S. Shafie, A. Sadrolhosseini, and H. Lim, "Preparations, Properties, and Applications of Polyaniline and Polyaniline Thin Films—A Review," *Polymers*, vol. 13, p. 2003, 06/18 2021, doi: 10.3390/polym13122003.

[44] X. Zhou, D. Wu, Z. Jin, X. Song, X. Wang, and S. Suib, "Significantly increased Raman enhancement on defect-rich O-incorporated 1T-MoS2 nanosheets," *Journal of Materials Science*, vol. 55, 12/01 2020, doi: 10.1007/s10853-020-05172-7.

[45] J. Bai *et al.*, "Glucose-Induced Synthesis of 1T-MoS 2 /C Hybrid for High-Rate Lithium-Ion Batteries," *Small*, vol. 15, p. 1805420, 03/08 2019, doi: 10.1002/smll.201805420.

[46] Y. Li *et al.*, "Cracked monolayer 1T MoS2 with abundant active sites for enhanced electrocatalytic hydrogen evolution," *Catalysis Science & Technology*, 10.1039/C6CY02649D vol. 7, no. 3, pp. 718-724, 2017, doi: 10.1039/C6CY02649D.

[47] K. S. Loh, L. yook heng, A. Musa, A. Salmah, and Z. Ishak, "Use of Fe3O4 Nanoparticles for Enhancement of Biosensor Response to the Herbicide 2,4-Dichlorophenoxyacetic Acid," *Sensors*, vol. 8, 09/01 2008, doi: 10.3390/s8095775.

[48] E. Bertolucci *et al.*, "Chemical and magnetic properties characterization of magnetic nanoparticles," *Conference Record - IEEE Instrumentation and Measurement Technology Conference*, vol. 2015, pp. 1492-1496, 07/06 2015, doi: 10.1109/I2MTC.2015.7151498.

[49] M. Compeán, F. Ruiz, J. R. Martinez, and A. Herrera-Gomez, "Magnetic properties of magnetite nanoparticles synthesized by forced hydrolysis," *Materials Letters - MATER LETT*, vol. 62, pp. 4248-4250, 10/01 2008, doi: 10.1016/j.matlet.2008.06.053.

[50] B. Singu, S. Palaniappan, and S. Pabba, "Benzoyl Peroxide Oxidation Route to Nano Form Polyaniline Salt Containing Dual Dopants for Pseudocapacitor," *Journal of The Electrochemical Society*, vol. 159, p. A6, 01/01 2012, doi: 10.1149/2.036201jes.

[51] V. K T and S.L.Belagali, "Characterization of Polyaniline for Optical and Electrical Properties," *IOSR Journal of Applied Chemistry*, vol. 8, 02/01 2015, doi: 10.9790/5736-0801025356.

[52] S. Yang, S. Zhu, and R. Hong, "Graphene Oxide/Polyaniline Nanocomposites Used in Anticorrosive Coatings for Environmental Protection," *Coatings*, vol. 10, no. 12, p. 1215, 2020. [Online]. Available: https://www.mdpi.com/2079-6412/10/12/1215.

[53] H.-Y. Zhu, X.-D. Song, X.-R. Yang, C.-J. Cheng, H.-R. Yu, and H.-H. Zhang, "Smart chiral magnetic nanoparticles for highly efficient enantioseparation of tryptophan enantiomers," *Journal of Materials Science*, vol. 54, 02/01 2019, doi: 10.1007/s10853-018-3072-z.

[54] H. Fattahi, N. Arsalani, and M. Nazarpoor, "Synthesis and characterization of PVP-functionalized superparamagnetic Fe3O4 nanoparticles as an MRI contrast agent," *eXPRESS Polymer Letters*, vol. 4, p. 329, 05/17 2010, doi: 10.3144/expresspolymlett.2010.42.

[55] H. Qiu *et al.*, "Dopamine-derived N-doped carbon-encapsulated MoS2 microspheres as a high-performance anode for sodium-ion batteries," *Ionics*, vol. 26, no. 11, pp. 5543-5551, 2020/11/01 2020, doi: 10.1007/s11581-020-03734-y.

[56] A. Bahuguna *et al.*, "Nanocomposite of MoS2-RGO as Facile, Heterogeneous, Recyclable, and Highly Efficient Green Catalyst for One-Pot Synthesis of Indole Alkaloids," *ACS Sustainable Chemistry & Engineering*, vol. 5, no. 10, pp. 8551-8567, 2017/10/02 2017, doi: 10.1021/acssuschemeng.7b00648.

[57] R. Thangappan *et al.*, "Graphene decorated with MoS2 nanosheets: a synergetic energy storage composite electrode for supercapacitor applications," *Dalton Transactions*, 10.1039/C5DT04832J vol. 45, no. 6, pp. 2637-2646, 2016, doi: 10.1039/C5DT04832J.

[58] V. Saadattalab, A. Shakeri, and H. Gholami, "Effect of CNTs and nano ZnO on physical and mechanical properties of polyaniline composites applicable in energy devices," *Progress in Natural Science: Materials International*, vol. 26, 09/27 2016, doi: 10.1016/j.pnsc.2016.09.005.

[59] L. Bao and X. Liu, "Study on the Synthesis and Photothermal Conversion Property of Polyaniline," *IOP Conference Series: Materials Science and Engineering*, vol. 772, p. 012048, 03/31 2020, doi: 10.1088/1757-899X/772/1/012048.

[60] M. Cao, X. Wang, W. Cao, X. Fang, B. Wen, and J. Yuan, "Thermally Driven Transport and Relaxation Switching Self-Powered Electromagnetic Energy Conversion," *Small (Weinheim an der Bergstrasse, Germany)*, vol. 14, p. e1800987, 06/07 2018, doi: 10.1002/smll.201800987.

[61] W. Zhang *et al.*, "Preparation of Polyaniline@MoS2@Fe3O4 Nanowires with a Wide Band and Small Thickness toward Enhancement in Microwave Absorption," *ACS Applied Nano Materials*, vol. 1, no. 10, pp. 5865-5875, 2018/10/26 2018, doi: 10.1021/acsanm.8b01452.

[62] Y. Zhang, X. Wang, and M. Cao, "Confinedly implanted NiFe2O4-rGO: Cluster tailoring and highly tunable electromagnetic properties for selective-frequency microwave absorption," *Nano Research*, vol. 11, no. 3, pp. 1426-1436, 2018/03/01 2018, doi: 10.1007/s12274-017-1758-1.

[63] L. Kong *et al.*, "Electromagnetic Wave Absorption Properties of Reduced Graphene Oxide Modified by Maghemite Colloidal Nanoparticle Clusters," *The Journal of Physical Chemistry C*, vol. 117, no. 38, pp. 19701-19711, 2013/09/26 2013, doi: 10.1021/jp4058498.

[64] L. Kong *et al.*, "Electromagnetic wave absorption properties of graphene modified with carbon nanotube/poly(dimethyl siloxane) composites," *Carbon*, vol. 73, pp. 185-193, 2014/07/01/ 2014, doi: https://doi.org/10.1016/j.carbon.2014.02.054.

[65] J. Liu, H. Liang, and H. Wu, "Hierarchical flower-like Fe3O4/MoS2 composites for selective broadband electromagnetic wave absorption performance," *Composites Part A: Applied Science and Manufacturing*, vol. 130, p. 105760, 2020/03/01/ 2020, doi: https://doi.org/10.1016/j.compositesa.2019.105760.

[66] P. Liu, Y. Huang, and X. Sun, "NiFe2O4 clusters on the surface of reduced graphene oxide and their excellent microwave absorption properties," *Materials Letters*, vol. 112, pp. 117-120, 2013/12/01/ 2013, doi: https://doi.org/10.1016/j.matlet.2013.08.126.

[67] N. Yousefi *et al.*, "Highly Aligned Graphene/Polymer Nanocomposites with Excellent Dielectric Properties for High-Performance Electromagnetic Interference Shielding," *Advanced Materials*, vol. 26, no. 31, pp. 5480-5487, 2014, doi: https://doi.org/10.1002/adma.201305293.

[68] Y. Wang, X. Di, Z. Lu, and X. Wu, "Rational construction of hierarchical Co@C@NPC nanocomposites derived from bimetallic hybrid ZIFs/biomass for boosting the microwave absorption," *Journal of Colloid and Interface Science*, vol. 589, pp. 462-471, 2021/05/01/ 2021, doi: https://doi.org/10.1016/j.jcis.2021.01.013.

[69] D. Zhang *et al.*, "Highly efficient microwave absorption properties and broadened absorption bandwidth of MoS2-iron oxide hybrids and MoS2-based reduced graphene oxide hybrids with Hetero-structures," *Applied Surface Science*, vol. 462, pp. 872-882, 2018/12/31/ 2018, doi: https://doi.org/10.1016/j.apsusc.2018.08.152.